University of Washington
Department of Civil and Environmental Engineering

HYDRAULIC AND MIXING CHARACTERISTICS OF SUCTION MANIFOLDS

R. E. Nece

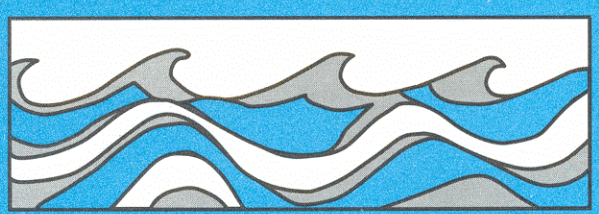

Water Resources Series
Technical Report No. 26
June 1969

Seattle, Washington
98195

Department of Civil Engineering
University of Washington
Seattle, Washington 98195

HYDRAULIC AND MIXING CHARACTERISTICS OF SUCTION MANIFOLDS

R. E. Nece

Water Resources Series
Technical Report No. 26

June 1969

Charles W. Harris Hydraulics Laboratory

Department of Civil Engineering

University of Washington
Seattle, Washington 98105

HYDRAULIC AND MIXING CHARACTERISTICS OF SUCTION MANIFOLDS

by

Ronald E. Nece

June 1969

Technical Report No. 26

Completion Report on

Grant No. WP-00512-5

from the

United States Department of the Interior

Federal Water Pollution Control Administration

Washington, D.C.

TABLE OF CONTENTS

ACKNOWLEDGMENTS

The study reported here was supported by the United States Department of Health, Education and Welfare, Public Health Service, under Grants No. WP-00512-1,2,3 and by the United States Department of the Interior, Federal Water Pollution Control Administration, under Grants No. WP-00512-4,5. The work was conducted at the C. W. Harris Hydraulics Laboratory, University of Washington, under the supervision of Ronald E. Nece, Professor of Civil Engineering (Principal Investigator).

This report summarizes the entire study. Because it is a summary and contains a relatively large amount of data, it was decided to restrict numerical results to graphical presentation instead of listing all experimental data in tabular form also. Four graduate students served as Research Assistants on the study; almost all data presented herein are tabulated in their respective M.S. theses. The four theses are listed below, and because results from them are used so extensively the theses are not listed in the report bibliography. The author gratefully acknowledges the contributions of his four junior colleagues, detailed more fully in the following:

Black, Jared L., 1965, "Characteristics of a Single Port Entrainment Manifold"

Linden, Richard A., 1965, "Characteristics of Multiple-Port Entrainment Manifolds"

Tuan, Denny K-Y., 1967, "Characteristics of an Annular Port Suction Manifold"

Rush, Roy H., 1968, "Mixing of Coaxial Streams in a Suction Manifold".

ABSTRACT

Experimental data have been obtained on the external hydraulic characteristics and mixing characteristics of two basic classes of suction manifolds. The objective was to obtain data which could be used in feasibility and/or design studies of using such devices to accomplish predilution in sewer outfalls, with special attention devoted to marine outfalls.

Results linking dilution rates and head loss characteristics are given for six single circular side-port manifolds, for multiport manifolds incorporating the same side ports, and for annular ports with and without axial symmetry. Data were obtained for density differences between the heavier ambient fluid entrained into the manifold and the initially undiluted conduit fluid ranging from $\Delta\rho/\rho_o = 0$ to $\Delta\rho/\rho_o = 0.042$. Within this range, which spans that to be encountered in outfall operation, density differentials have relatively little effect on the dilution-head loss characteristics of the configurations tested.

Mixing characteristics within the conduit downstream from the manifold were investigated for a range of density differentials for the annular-port manifold only, with stratification tendencies investigated.

The laboratory apparatus and techniques are described. Extrapolation of experimental results obtained from the 2-inch diameter test line to installations of prototype size are discussed.

Comparison of the two geometries tested shows that the annular-port manifold possesses hydraulic advantages over single circular side-port manifolds. Limitations of operating ranges of the manifolds in sewer outfall applications are delineated.

LIST OF FIGURES

LIST OF SYMBOLS

A	area of conduit
A_i	discharge area of nozzle, annular-port manifold
A_x	projected area of inflow jet from side port
A'	effective flow passage area past inflow jet
a	area of inflow port, circular or annular
b	gap width, annular port
C_e	entrainment coefficient
c_e	dye concentration, ambient fluid
c_m	dye concentration, downstream, fully mixed
c_o	dye concentration, initial conduit fluid
c'	dye concentration, local value at a point in the mixing chamber
D	inside diameter of conduit
d	diameter of circular port
$\mathbb{E}$	port Euler number
$\mathbb{E}'$	port Euler number using local conditions at plane of side-port axis
e	performance ratio, side ports
$\mathbb{F}$	densimetric Froude number
F_f	boundary force
f	Darcy-Weisbach friction factor
g	acceleration of gravity
H_d	downstream excess head, annular port
H_g	head gain of entrained flow, annular port
H_L	head loss of conduit flow
H_p	excess head of approach flow in conduit
h_f	friction head loss in conduit
L	specified length of conduit

n	number of ports in multiple-port manifold
p	average pressure in conduit, downstream
p_e	pressure in ambient fluid
p_i	average pressure at plane of nozzle outlet
p_o	average pressure in conduit, upstream
p'	effective pressure over section of area A'
Q	volumetric flow rate in conduit, downstream
Q_o	volumetric flow rate in conduit, upstream
q	volumetric flow rate, port inflow
$\mathbb{R}_a$	Reynolds number, annular port
$\mathbb{R}_e$	Reynolds number, circular port
$\mathbb{R}_o$	Reynolds number, for approach flow in conduit
r	radius of curvature of port lip, circular port
r_i	radius of nozzle outlet, annular port
t	thickness of conduit wall
u	local axial velocity in conduit
V	average velocity in conduit, downstream
V_n	average velocity in conduit, downstream from n-th port in multiple-port manifold
V_o	average velocity in conduit, upstream
V'	average velocity in conduit, through area A'
v	average velocity through port
X	distance between ports, or distance downstream from nozzle outlet of annular port
x	axial distance along conduit
y	jet penetration distance
γ	specific weight of downstream fluid in conduit
γ_o	specific weight of initial upstream fluid in conduit
ΔH	pressure head difference across port, exterior to conduit

Δh	piezometric head drop in conduit, across port
Δp	$p_e - p_o$, for side port
$\Delta \rho$	$\rho_e - \rho_o$
μ_e	viscosity, ambient fluid
μ_o	viscosity, undiluted approach flow in conduit
ρ_e	density, ambient fluid
ρ_o	density, undiluted approach flow in conduit
ρ'	local fluid density at a point in the mixing chamber

I. INTRODUCTION

The work described in this report is a laboratory study of the hydraulic and mixing characteristics of two forms of suction manifolds. The study was prompted by the desire to obtain background data necessary to determine the feasibility of utilizing the concept of predilution in marine sewer outfalls.

When sewage effluent is discharged from an outfall structure into a body of salt water, the lower density of the sewage causes it to rise as a buoyant plume toward the surface of the denser receiving sea water. As the buoyant plume rises it mixes with the surrounding water and there results a continual growth in size and increase in density (hence, decrease in the buoyant force causing the upward motion) of the plume. The fluid mechanics of buoyant jets has received much attention; a typical treatment is that by Abraham (1967), which also summarizes other experimental and theoretical studies. The characteristics of sewage plumes in sea water have been presented by Rawn, Bowerman, and Brooks (1961). If the mixture of sewage and sea water remains lighter than the ambient fluid throughout its entire rise the plume will ultimately reach the water surface. It may be possible to take advantage of density stratification of the receiving water in the engineering design of outfalls where the discharge at times may not rise to the free water surface; such considerations in a typical design have been presented by Brooks and Koh (1965).

The design objective is to minimize the pollutant concentration which may ultimately reach the surface or enter into layers near the surface. Types of outfall structures designed to produce satisfactory pollutant concentrations near the surface have been summarized by Pearson (1956); the design of multiport diffuser outfalls has been discussed by Rawn, Bowerman, and Brooks (1961).

Appropriate changes in outfall conduit dimensions or in flow characteristics at the outlet can result in changes in pollutant concentrations at or near the water surface. Whether an outfall may consist of the most common type (a simple single-pipe structure discharging through the open end of a conduit laid on the ocean floor) or of a more complex

structure such as a multiport diffuser, decreased surface concentrations of the pollutant can be achieved for a given effluent discharge rate by decreasing the diameter(s) of the discharge opening or by extending the outfall so that it terminates at a greater depth. For a given outfall size and location, an increase in the effluent density or an increase in the total flow rate would result in reduced rise rates of the sewage plume. Acceptable surface conditions thus could be possible for shallower, hence shorter and less expensive, outfalls. Likewise, with no reduction in outfall length, the sewage concentrations near the surface would be reduced.

One possible mechanism for increasing the density of the effluent, as suggested above, is predilution of the sewage in the outfall conduit. A device suggested for obtaining the desired predilution is a suction manifold, a section of reduced conduit cross-sectional area within which the pressure could be reduced below that of the ambient fluid which would in turn be "sucked" into the venturi-like section through openings in the conduit wall. The mixture of the dilution flow with the initial effluent liquid in the conduit would produce a discharge mixture of increased density. Further advantages would exist if the receiving water were thermally stratified because the dilution flow would ordinarily be the cooler, denser water drawn from the vicinity of the bottom; such conditions could exist in lakes or partially mixed streams.

In order to determine the engineering and economic feasibility of the predilution scheme, it is necessary to obtain engineering design criteria. The primary external hydraulic characteristics are the possible entrainment flow rates and accompanying head losses. The predilution concept depends upon the efficacy of the mixing process within the manifold. Questions of particular concern from the standpoints of design and possible operation are the dimensions (primarily, length) of structure required for adequate mixing and the degree of mixture uniformity actually achieved in the device.

For a typical outfall placed on the ocean bottom the logical location for the entrainment opening(s) would be at or near the top of the conduit. In this way boundary effects of the ocean bottom on flow conditions at the dilution opening would be minimized. Likewise, the

possibility of drawing fine sediments from the bottom into the manifold is reduced, as is the possibility of subsequent undermining of the structure due to this sediment entrainment. For an initial concept of the problem, however, proximity effects of the bottom may be neglected. The fluid mechanics problem then may be stated more formally as an investigation of the entrainment, head loss, and mixing characteristics associated with flows through openings in the wall of and into a full-flowing circular conduit surrounded by an infinite body of fluid at rest.

An infinite variety of geometries could be employed to obtain predilution. The study reported here was restricted to two of the more simple configurations:

(1) Circular side ports (single or multiple openings, the latter in a straight row) in the wall of a circular conduit.

(2) Annular ports (either axially symmetric or partially closed) so shaped that the dilution flow enters the mixing region of the manifold in a direction parallel to the axis of the circular pipe.

Emphasis in the laboratory study was placed on the determination of the gross hydraulic characteristics of the configurations tested rather than on details of the internal flow pattern. Objectives were to find these characteristics for geometries and for fluid density differences that would be pertinent to outfall structures. In terms of relationships between approach velocities in the conduit and pressure differentials between the ambient and conduit fluids, laboratory data were obtained over wider ranges than those which could exist in sewer outfall applications. The mixing studies were confined mostly to the annular port configurations because this geometry possesses a greater hydraulic efficiency and also internal flow fields leading to better degrees of mixing than in the side port manifolds; the mixing studies conducted were largely exploratory in nature.

Chapter II contains descriptions of the apparatus and experimental procedures used in the laboratory investigation. Results for the two general manifold configurations are treated separately in Chapters III and IV; the theoretical analyses of the two geometries likewise are developed separately in the respective chapters. The two manifold types are compared in the concluding Chapter V.

II. EXPERIMENTAL APPARATUS AND PROCEDURES

A. Test Loop

The laboratory installation consisted of a straight horizontal pipe section simulating the conduit, a sealed container simulating the infinite volume of the ambient fluid and surrounding that part of the conduit treated as the manifold, and a separate piping system supplying the entrained fluid. These three components were called the "conduit", the "ocean box", and the "salt water supply", respectively. The conduit (fresh water line) and the ocean box are shown schematically in Fig. 1; the salt water system is shown in Fig. 2.

The 2-inch test line was supplied with fresh water from a constant head tank. Valves located at each end of the line provided regulation of both discharge rates and line pressures in the test section. Discharges were measured by interchangeable orifices, calibrated in place, located in the approach section. The approach and downstream sections of the line were galvanized standard 2-inch pipe; the 11-foot long test section was made of 2-inch inside diameter transparent cast acrylic tubing. All joints along the main conduit were flanged in order to minimize local disturbances; further, the flanges facilitated changes of the 2-foot long "manifold" section passing through the ocean box. Details of the respective manifold sections tested are described in Sections B and C.

The plastic test section was initially calibrated for pipe friction characteristics before any manifold openings were placed in the line; friction characteristics of the test section matched the smooth-pipe curve on the conventional Moody diagram.

The ocean box was a cubical tank 17 inches on a side and fabricated from clear acrylic plastic to allow visual observations. The dilution fluid entered the box at the bottom where a diffuser plate baffle dispersed the entering jet. The box was equipped with a thermometer, an air vent at the top to facilitate filling, and a dye injector which could be used for observations of the flow patterns through the manifold ports. The front of the box was removable for access to the manifold. Details of the ocean box, including some indication of the ring clamps (used in conjunction

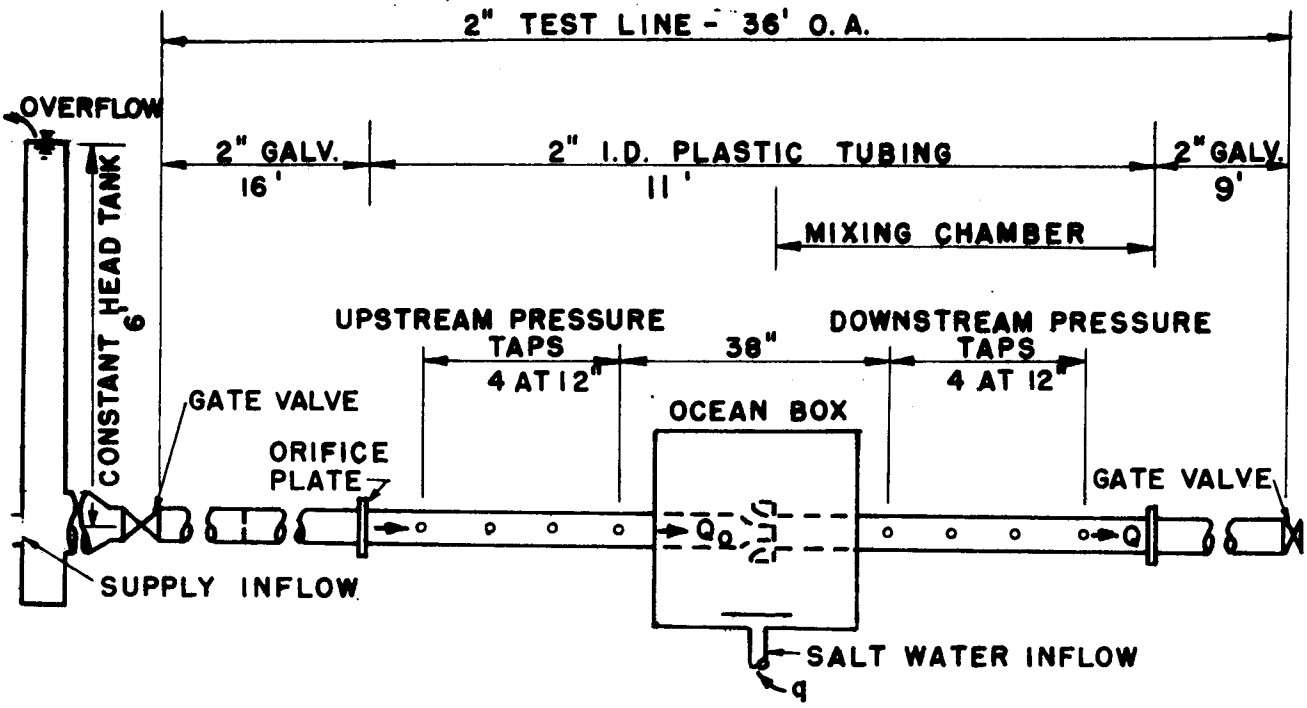

Figure 1. Laboratory Apparatus: Fresh Water Supply System

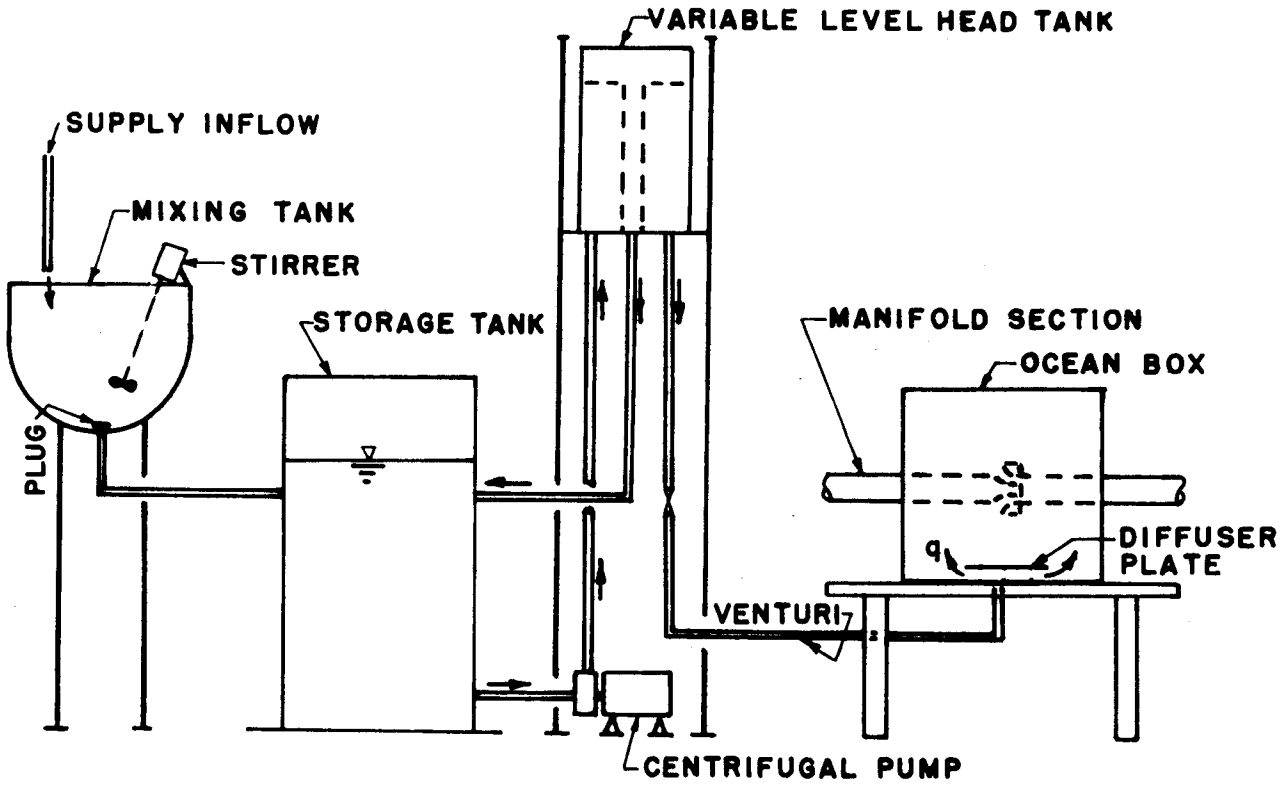

Figure 2. Laboratory Apparatus: Salt Water Supply System

with O-rings) used for sealing the box where it was pierced by the main conduit, are shown in Fig. 4.

Pressure levels in the ocean box were controlled by a variable level head tank, used in conjunction with a regulating valve, in the salt water supply system. Salt solutions of desired densities were mixed in the mixing tanks and piped to the storage tank. A pump lifted the salt water to the constant head tank: overflow from the elevated head tank returned directly to the salt water storage tank. Entrainment (dilution) flows were measured by interchangeable venturi meters, machined from plastic and then calibrated in place, in the supply line leading to the ocean box. For tests in which there was no density differential between the conduit and dilution flows, fresh water was piped directly and continuously into the "salt water" system, via the mixing tanks. Densities were measured by extracting samples from the storage tank and testing these samples on a commercial specific gravity balance.

Relative pressure levels at various points in the test loop were measured by piezometer columns mounted on a central manometer board. Four pressure taps evenly spaced at 12 inches upstream from the ocean box and four comparable taps downstream from the box allowed the hydraulic grade line to be determined on both sides of the suction manifold. A pressure tap in the ocean box wall provided a reading of the piezometric head of the ambient fluid. When the annular port manifold was installed, a pressure tap was provided through the conduit wall and opposite the end of the nozzle. The individual piezometer columns to which the pressure taps were connected were in turn manifolded so as to have a common air pressure above the water columns on the manometer board. The flow meters in both the fresh water and the salt water supplies were connected to air-water differential manometers. Discharges in the upstream conduit were in the range 0.022-0.135 cfs, while flows through the salt water supply line were in the range of 0.001-0.033 cfs.

As indicated in Figs. 1, 2, and 4, the test manifold was approximately centered in the ocean box.

B. Details of Side Port Manifolds

Six individual circular side port configurations were tested.

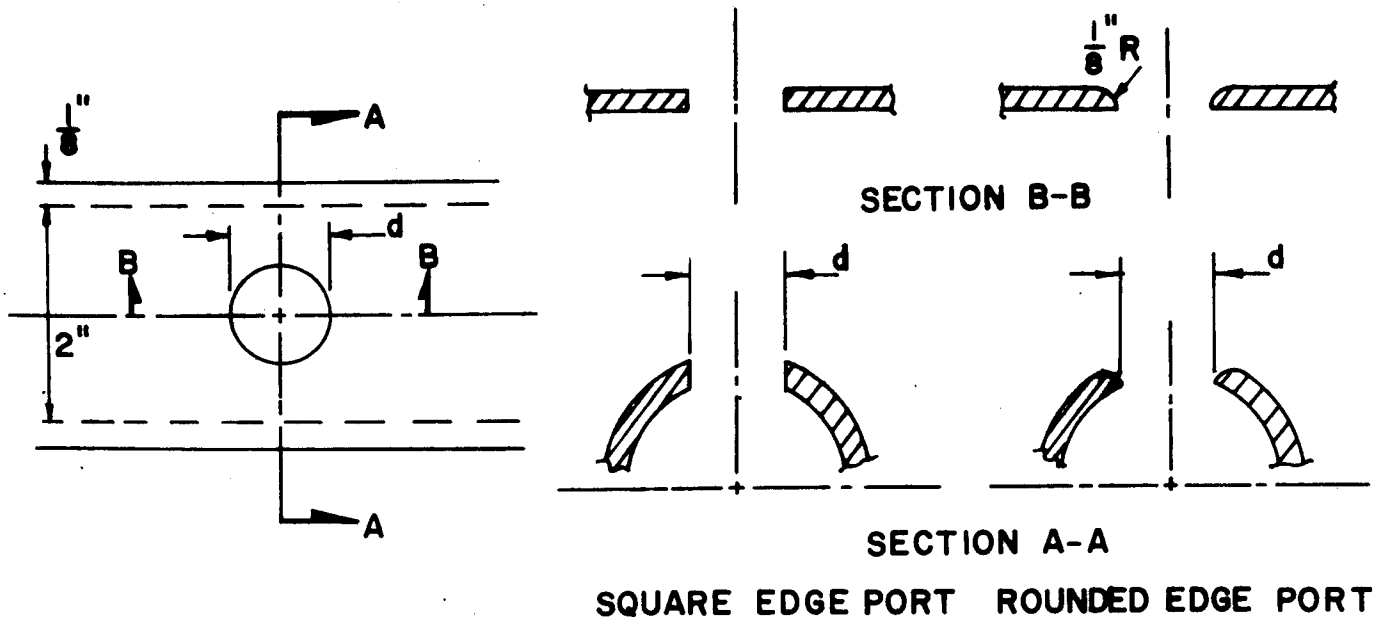

Figure 3. Notation and Details for Single Circular Side Ports

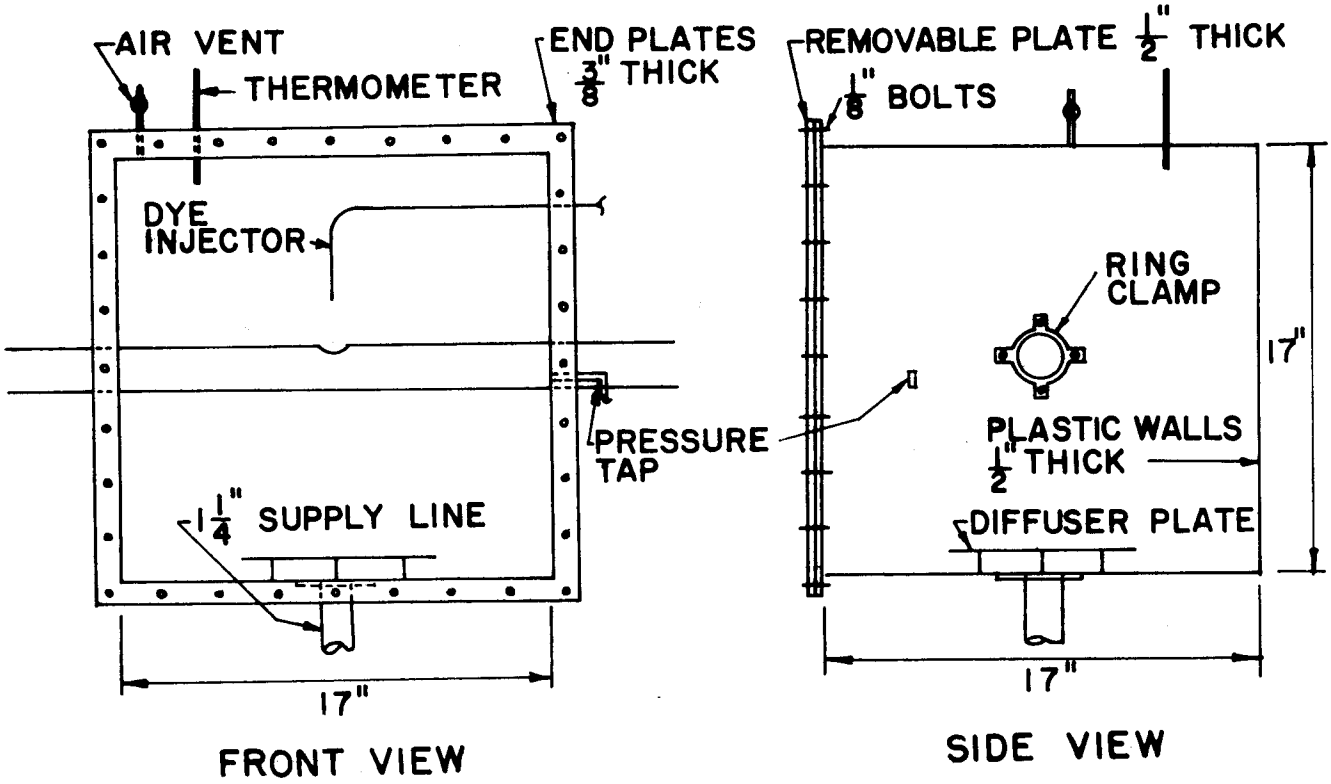

Figure 4. Details of Ocean Box

In each case the circular port was located at the top of the conduit as indicated schematically in Fig. 4. The actual inside diameter, D, of the nominal 2-inch plastic tubing was 2.003 inches. Nominal port-to-conduit diameter ratios (d/D) of 1/8, 1/4, 1/2, and 1/1 were tested. Square-edged ports were tested for all four diameter ratios; in each case the ports were drilled and then reamed to provide burr-free openings through the conduit wall. Rounded-edge ports were tested for nominal d/D ratios of 1/8 and 1/4. In each case the radius of the lip curvature was equal to d/4. For all ports other than d/D = 1/8, the actual wall thickness was 0.144-inch (nominal, 1/8-inch); the wall thickness for the d/D = 1/8 openings was 0.072-inch. The general geometry and notation for the circular side ports is indicated in Fig. 3. The port and conduit diameters used in all calculations of experimental results were measured to ±0.002-inch. Dimensions of the single side ports are listed in Table I.

Table I.

Dimensions of Circular Openings, Side Port Manifolds

Nominal $\frac{d}{D}$	Lip Shape	d, Inches	a, Sq. Feet
1/8	Square Edge	0.251	0.000345
	Rounded Edge	0.258	0.000362
1/4	Square Edge	0.503	0.00138
	Rounded Edge	0.500	0.00136
1/2	Square Edge	1.031	0.00580
1/1	Square Edge	2.032	0.0226

The port-to-diameter ratios of 1/4, 1/2, and 1/1 were selected so that results could be compared with those obtained by McNown (1954) for head losses in pipe manifolds. The smaller value, d/D = 1/8, was selected, so that trends in parametric behavior could be determined for relatively smaller ports.

Multiple port configurations using circular side ports were obtained by drilling more than one hole (of equal diameters) in a straight row along

the top of the conduit. Square-edged ports only were investigated, and for all cases the conduit wall thickness was 0.144-inch. (It is noted here that the d/D = 1/8, square-edged ports predictably have the same performance for the two wall thicknesses tested). Double- and triple-port arrangements were tested, with the distance along the conduit between centers of consecutive ports given the notation, X. Configurations of the multiple port manifolds tested are listed in Table II.

Table II.

Configurations of Multiple-Port Manifolds

Nominal $\frac{d}{D}$	Double- or Triple-Port	X/D Spacing
1/8	Double	2.5, 5
"	Triple	2.5
1/4	Double	2.5, 5
"	Triple	2.5
1/2	Double	2.5, 5

In the multiple port tests the multiple openings were located in the manifold so that the centerline of the port or ports closest to the end wall(s) of the ocean box was no closer than 3-1/2 inches from the wall. Preliminary investigations by Goldstern (1963) indicated that wall proximity effects would not be present so long as ports were spaced at least this distance from the walls of the ocean box.

The dye injector shown in Fig. 4 was made of stainless steel tubing of 1/8-inch nominal outside diameter. The injector, which was connected to an external supply of neutrally buoyant dye, could be axially aligned with the port axis in order to make visual observations of the flow of the jet entering through the port and into the conduit.

C. Details of Annular Port Manifolds

One basic configuration was used in all of the annular port manifold tests. Modifications which could be made in the geometry of the basic arrangement are detailed later in this section.

The manifold section was formed from a combination of two separate 2-inch (nominal) inside diameter clear, cast acrylic tubes with a 1/8-inch wall thickness. The two-section arrangement was required in order to assemble the manifold within the ocean box; unlike the side port manifold, a single plastic test section could not be inserted through both end walls of the ocean box which could be moved horizontally allowing access for changing test sections. The axis of the annular port and nozzle combination coincided with the axis of the conduit. The annular passage was so shaped that the dilution flow passing through this inlet would enter the conduit with streamlines parallel to the conduit axis. A bell-mouth outer lip provided smooth flow conditions near the inlet to the annulus, and minimized possibilities of separation and resultant increased turbulence in the annular chamber. Details of the manifold are shown in the cutaway drawing of Fig. 5; the plug arrangement used to obtain partial closure of the annular ring was entirely removed for tests on the basic, axi-symmetric arrangement. The nozzle attached to the approach conduit likewise was shaped to be hydraulically efficient and to discharge parallel to the conduit axis. The location of the pressure tap considered to register pressures at the nozzle outlet also is shown in Fig. 5.

A rig to support, connect, and align the two separate parts of the manifold consisted of three rows of three acrylic supports glued to the periphery of the conduit and evenly spaced about the circumference, and in turn joined by connectors which were shimmed as necessary for proper alignment. One support row-connector grouping was placed below the conduit invert. The entire unit was constructed in order to insure initial axial symmetry of the flow, of concern especially in the annular port mixing studies. Details of the support assembly are shown in the drawing, Fig. 6.

The assembled manifold rig is shown in place in the ocean box in Fig. 7, and the assembly alone is shown in Fig. 8. The plastic connectors were slightly rounded and feathered opposite the port entrance, as shown in Fig. 8, to minimize any possible effect upon entrance flow conditions. The separate plastic segments shown in Fig. 8 are the acrylic plugs indicated in Fig. 5.

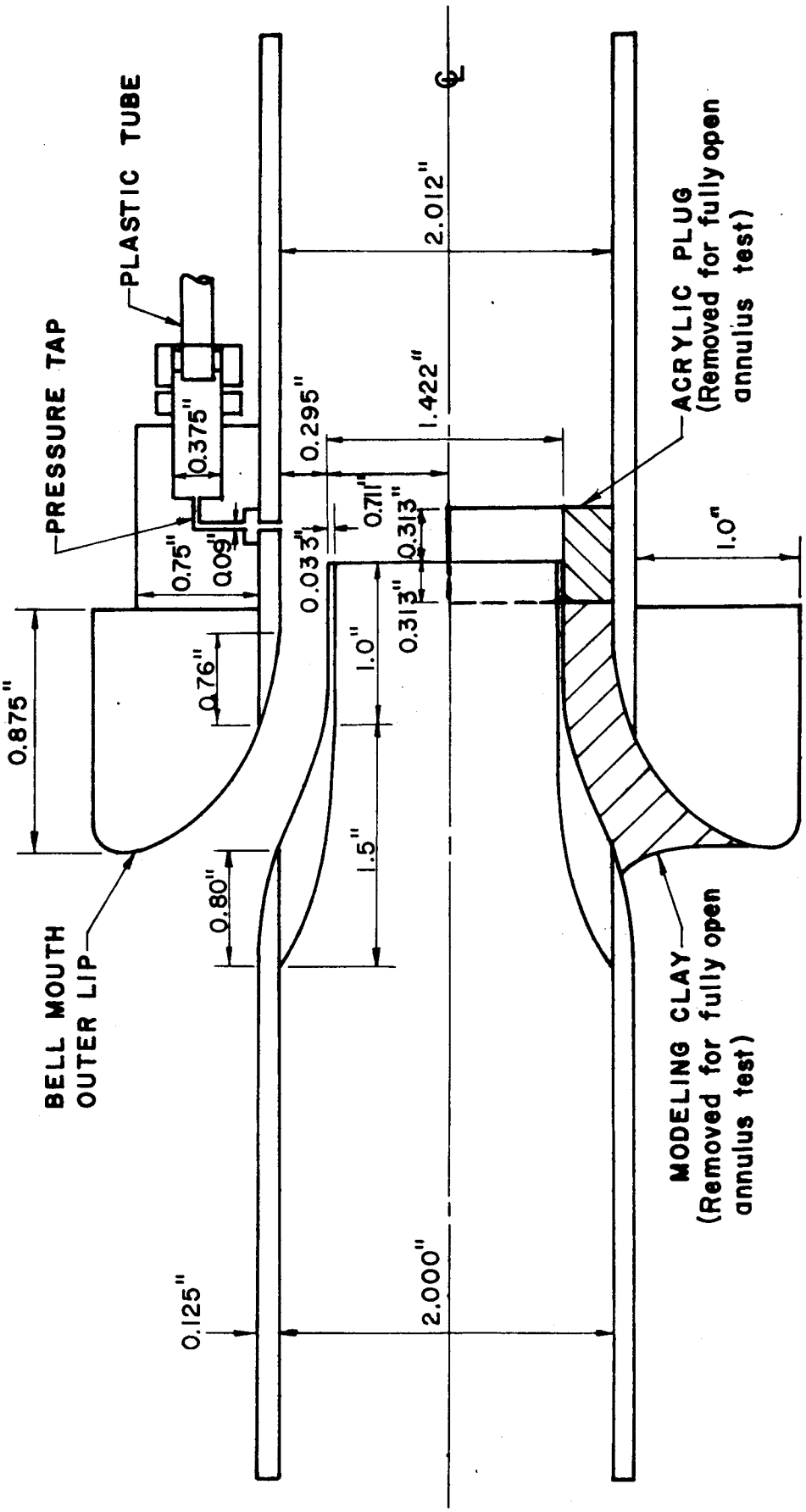

Figure 5. Details of Annular-Port Manifold

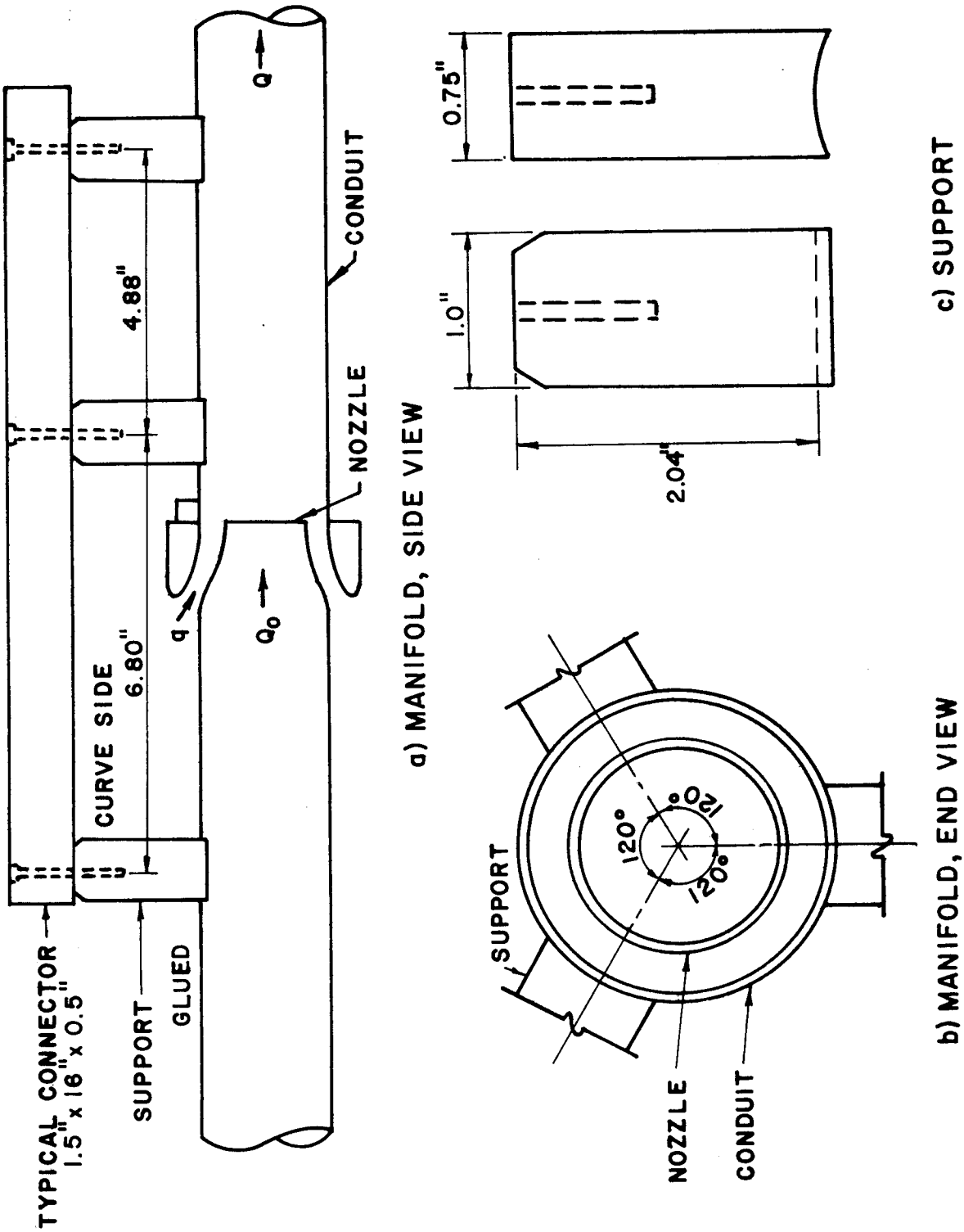

Figure 6. Details of Manifold Positioning Arrangement

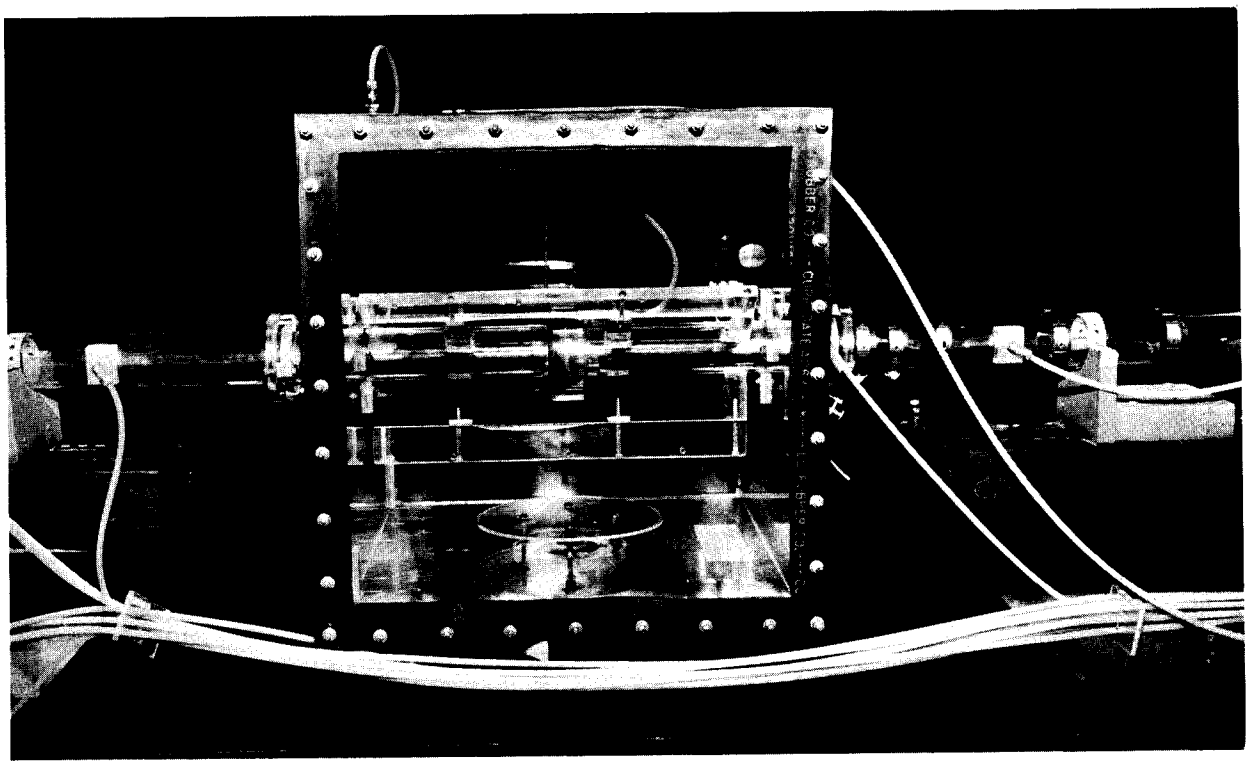

Figure 7. Ocean Box and Manifold

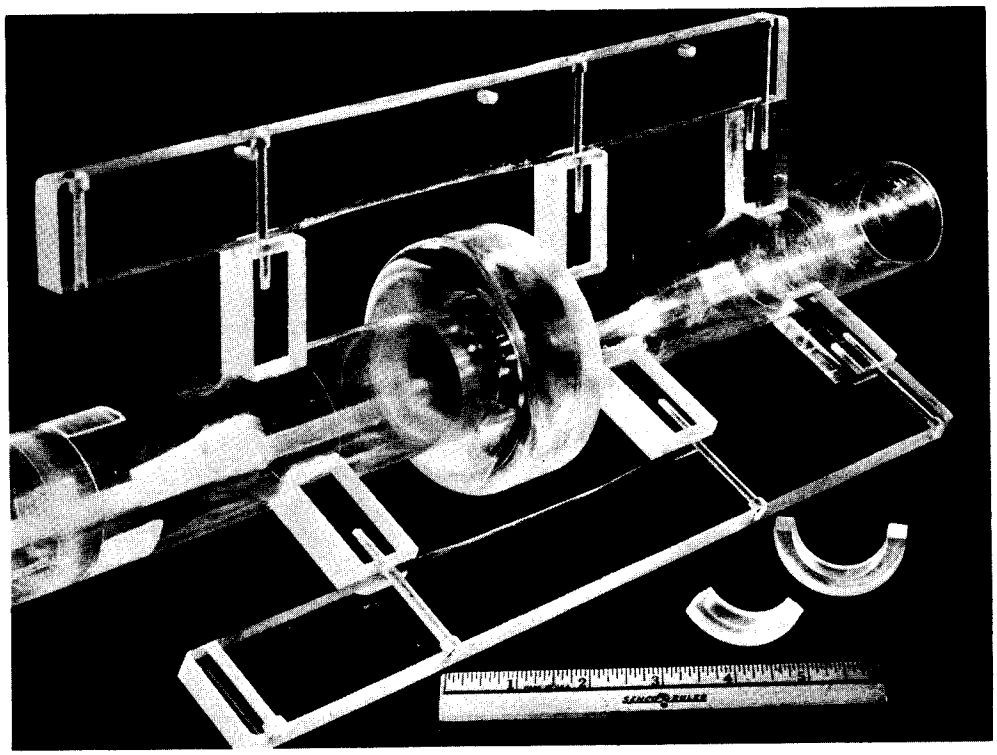

Figure 8. Annular-Port Manifold

Various ratios of annular port area: downstream conduit area were obtained by the use of plugs in the annular port. If such an annular port were to be used in a sewer outfall it would be logical, as indicated in Chapter I, to close part of the lower portion of the annular opening. Two partial closures were tested, one closing off the bottom one-half of the annulus and the other closing off the lower one-third; the former might be considered in an outfall when floor protection is the main matter of concern, while the smaller plug may be of use when questions of alignment of the port and nozzle are most important and floor protection is less significant. Modeling clay was used to complete the partial closures; the clay was shaped to provide as streamlined a flow as possible, with the objective again being to produce a discharge from the annulus which was parallel to the conduit axis. In Fig. 9 the plug and modeling clay are in place for the one-half closure of the annular port.

Data on the geometry of the three manifolds tested are listed in Table III. Introducing notation to be utilized throughout this report, a is the cross-sectional area of the port opening at its discharge plane, A_i is the nozzle area, and A is the area of the downstream conduit.

Table III.

Configurations of Annular Port Manifolds

Nozzle wall thickness	:	0.033 inches
A_i	:	0.01003 sq. feet
A	:	0.02182 sq. feet
A_i/A	:	0.460

Annulus configuration	Nom. a/A	a - sq. ft.	a/A
Fully Open	1/2	0.01078	0.494
1/3 Closed	1/3	0.00743	0.340
1/2 Closed	1/4	0.00539	0.247

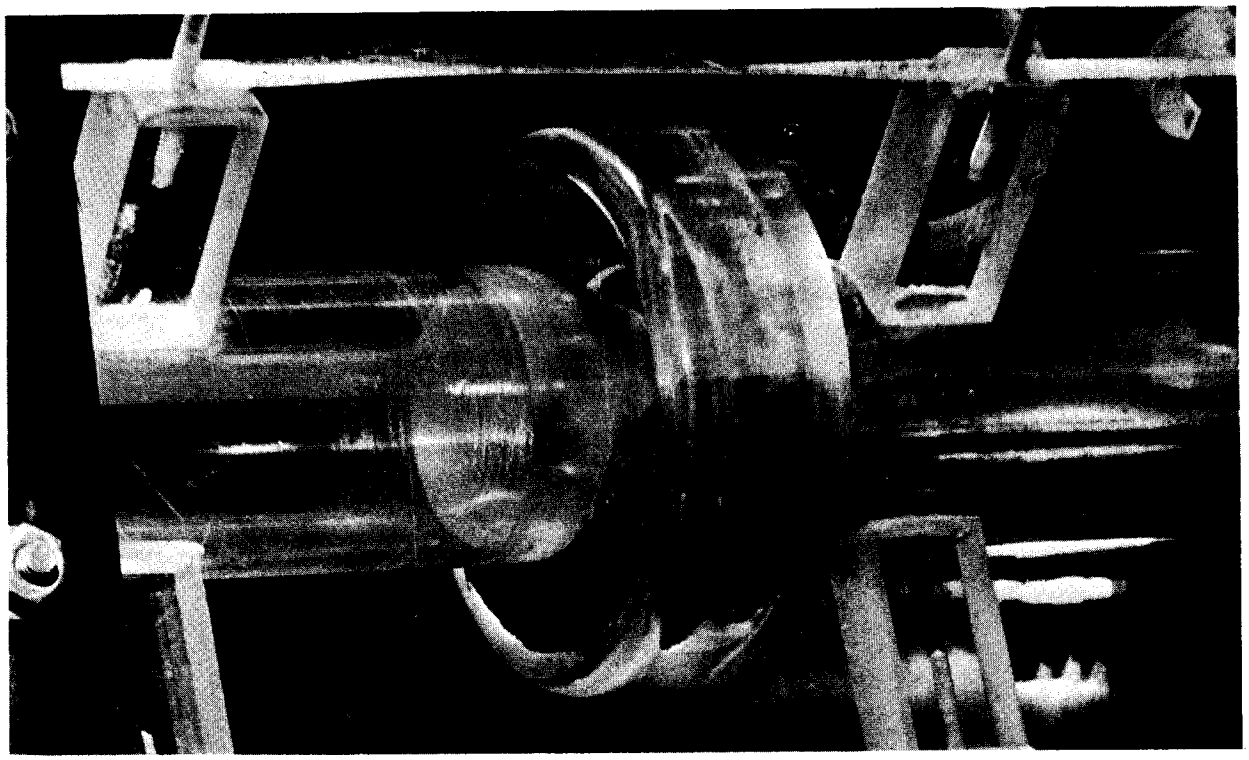

Figure 9. Annular-Port Manifold with Partial Closure

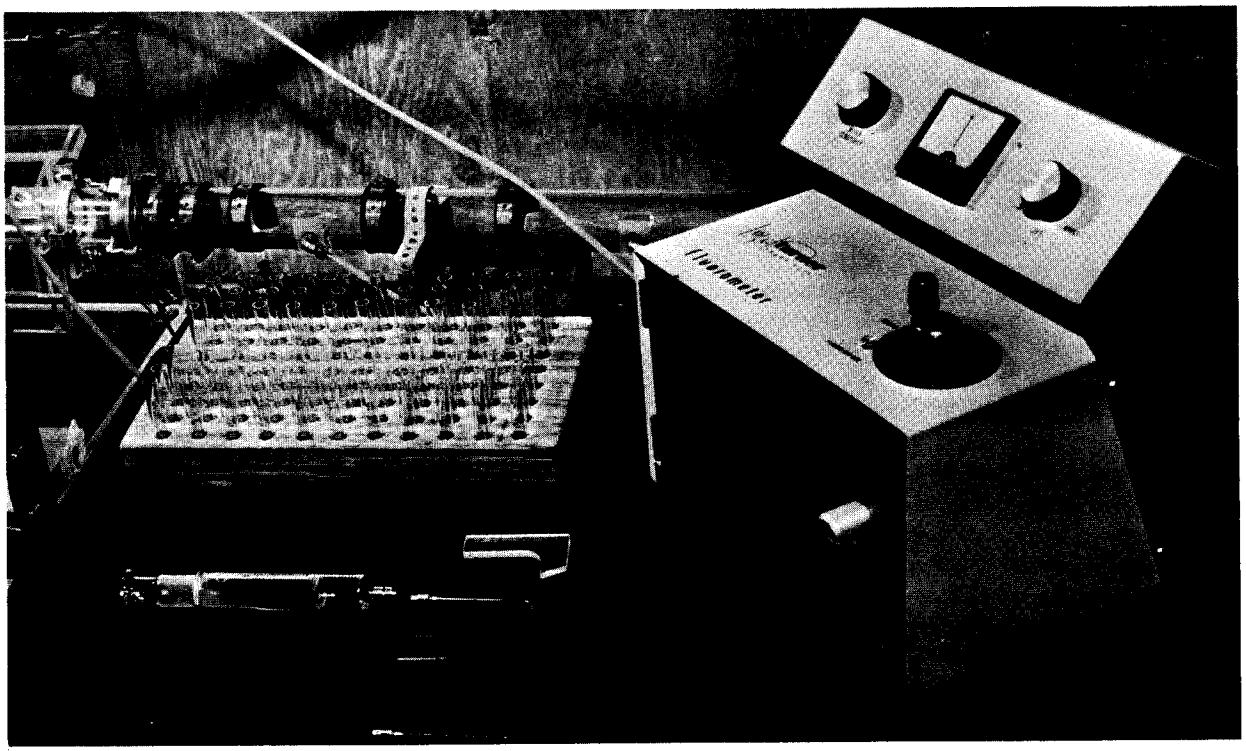

Figure 10. Dye Sampling Section and Apparatus

D. Methods for Determining External Hydraulic Characteristics

Data taken for one run included pressure heads along the conduit and in the ocean box, and manometer readings on the conduit orifice and on the venturi in the entrained fluid supply line. Temperatures were recorded for each series. Slightly different procedures were used for the side port manifold and for the annular port manifold, and are described briefly below.

For a single circular side port, piezometric grade lines were extended both downstream (from the upstream pressure taps) and upstream (from the downstream taps) to the station of the port axis. These lines were drawn by plotting the conduit pressure head readings to scale, and drawing the best fit straight line through each set as determined by the smooth pipe friction factor for the corresponding conduit Reynolds number; the slopes of the grade lines were determined from the Darcy-Weisbach equation,

$$\text{slope} = \frac{h_f}{L} = \frac{f}{D}\frac{V^2}{2g}$$

where V is the appropriate average velocity. Following conventional hydraulic practice, the difference in levels of the hydraulic grade lines when extended to the port station was taken to be the piezometric head differential Δh across the port. The head loss was determined after adding the upstream and downstream velocity heads, using average velocities, to the appropriate hydraulic grade line elevations at the port. Manifold head losses so determined would be added to conventional pipe friction losses in design calculations. The difference between the external fluid pressure and that of the conduit flow at the port was the difference between the box piezometer reading and that of the upstream hydraulic grade line extended to the port.

Head loss tests involving density differentials were restricted to the single port manifolds. In these runs the entrained salt water was sampled at the base of the ocean box pressure column on the piezometer board, after bleeding. The driving pressure differential between the ocean box and the approach conduit was calculated at the elevation of the

port entrance at the top (inside diameter) of the conduit.

In computing results for the multiple port manifolds, it was assumed that downstream ports have no effect upon upstream ports. Goldstern (1963) had determined in a preliminary study that this assumption is valid so long as X/D is greater than 1/1, the case for geometries tested in the study reported here. Hydraulic grade lines were extended as described above downstream and upstream, respectively, to the most upstream and most downstream ports. The upstream port characteristics were assumed to be those of a single port, as determined in the prior tests; the port head loss and piezometric head drop were known, establishing levels of the total head line and hydraulic grade line at the downstream side of the port. Head gradients in the pipe reach leading to the next port downstream again were calculated using the Darcy-Weisbach equation but including the entrained flow from the upstream port. The upstream head levels at the subsequent port were established by the extension of the grade lines to the port. The procedure was extended for as many ports as necessary; in all cases, the measured grade line in the conduit downstream from the manifold provided the loss characteristics at the port farthest downstream. The practice described assumes linear grade lines between ports, whereas in reality flows between ports are not one-dimensional; again, however, the practice is conventional and also allows a simple way of defining or calculating pressures at intermediate ports. The head losses for multiple port manifolds listed in this report do not include friction losses between ports; this point is discussed further in Section B of Chapter III.

In the annular port manifold tests the pressure head differential between the ocean box and the nozzle tip was measured directly. The nozzle pressure head reading was used to establish the total head at the entrance to the mixing chamber of the manifold; the downstream grade line was extended upstream to the plane of the nozzle opening. Head losses and piezometric head drops so calculated and listed in this report apply only to the mixing chamber region downstream from the nozzle tip. Losses associated with the conduit nozzle section itself could be obtained by use of the upstream grade lines, but these calculations were not made on a routine basis.

E. Mixing Study Procedures

To determine the efficiency of the suction manifold as a mixing device, some observations were made of mixing patterns downstream from the manifold. These tests were limited in the case of the side port manifold, being confined to inflows from a single port and with zero density differential between conduit and ambient fluids. Tests with the annular port were more extensive in both number and spatial coverage, as well as being extended to flows with density differentials.

Mixing patterns were determined through the use of rhodamine B as a fluorescent tracer. Dye was added to the dilutant in the mixing tank; none was added to the "fresh water" supplying the upstream conduit. The dye concentration of the "salt water" was controlled through careful batching processes, and served as the reference value during the runs. Openings (0.13-inch diameter) were drilled in the test section conduit wall to allow the withdrawal of samples by means of 15-gauge hypodermic needles attached to syringes. At each station where dye patterns were measured a rubber ring around the conduit exterior was retained in place by a hose clamp; holes drilled in the clamp allowed the hypodermic needle to be inserted through the wall and into the flow. Test samples were withdrawn slowly in order to obtain time-average samples of the dye concentration at the particular locations in the turbulent flow. The needle used for withdrawing samples was pointed upstream; spacers were used to control the particular position of the needle within the conduit in order to insure the accuracy of the sampling location, and a template was used to insure that the curve in the slender needle remained constant throughout the tests. Relative dye concentrations of all individual samples, as well as of the original dilutant, were determined with a Turner Model 110 fluorometer. Figure 10 shows the test section and the equipment used for withdrawing and measuring the relative dye concentrations of the samples.

Samples were withdrawn at various cross-sections and lateral locations as shown in Fig. 11. Section A-A in the drawing indicates the sampling locations on horizontal, diagonal, and vertical transects; a complete mixing traverse at a station involved 27 separate samplings, three being taken on the the centerline and serving as a check on consistency. Mixing patterns could be deduced from the local dye concentration values; no attempt was

STATION	X-DISTANCE (INCHES)	X/D
1	0	0
2	11.4	5.7
3	12.9	6.4
4	14.9	7.4
5	20.1	10.0
6	25.0	12.5
7	35.0	17.5
8	59.0	29.5
9	100.0	50.0

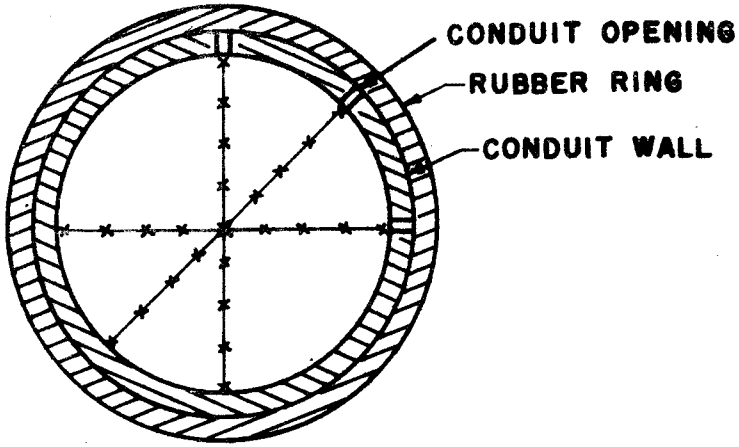

SECTION A-A

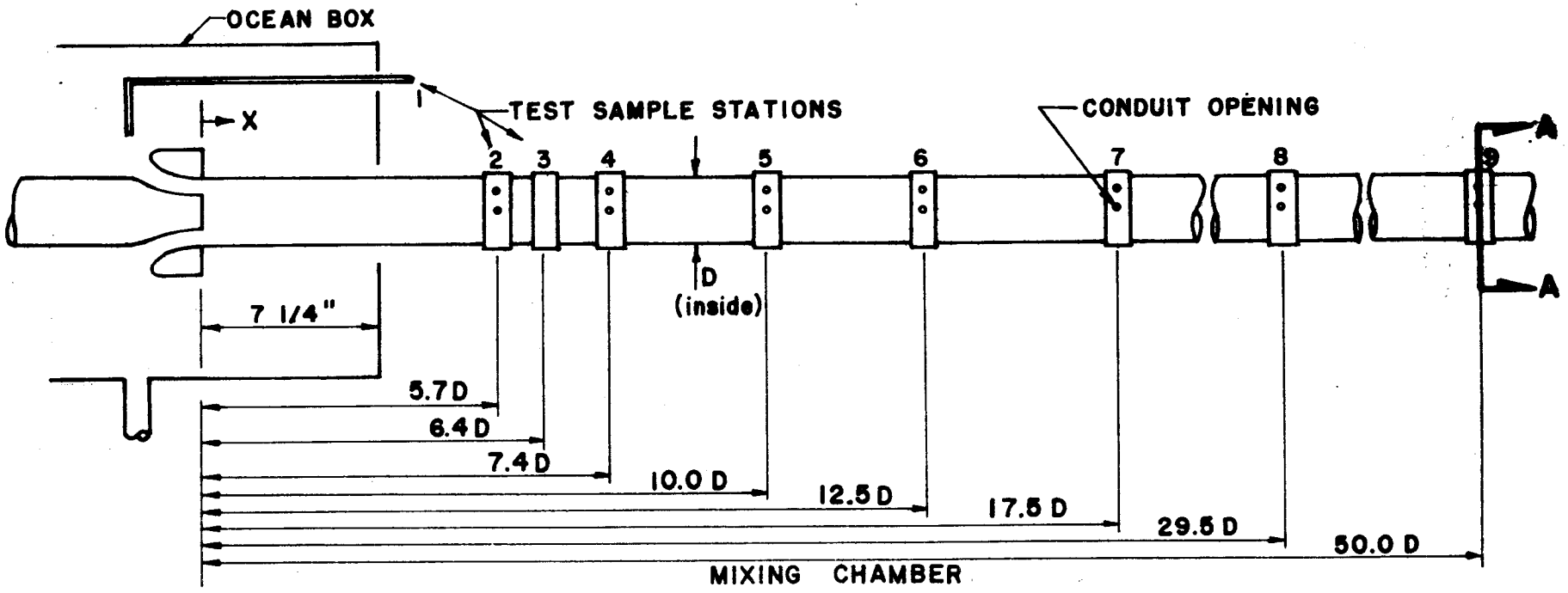

Figure 11. Test Section and Sampling Locations for Mixing Data

made to measure velocity profiles in the mixing region.

The same technique was applied whether density differentials (obtained by adding salt to the dilutant) were present or not. Separate comparisons indicated that measured due concentrations correlated directly with the specific gravities of samples withdrawn from the mixing region and that the quantitative agreement between the two types of measurement was within 5 percent. Because of the recognized limits on the accuracy and reproducibility of the single spot measurements in a turbulent flow, and considering the exploratory nature of the mixing tests, the faster and more convenient dye measurement technique was used throughout. Further, gross checks on the method were provided by measuring the dye concentration of the ultimate effluent at the downstream (waste) end of the test loop where, due to exit piping configuration, complete mixing could be assumed; the ratio of this concentration to that of the initial dilutant should equal the ratio of dilutant discharge to combined downstream discharge. Satisfactory checks were obtained.

F. Flow Visualization by Hydrogen Bubble Technique

The hydrogen bubble flow visualization technique was attempted with the side port manifold in order to make observations of the behavior of a jet entering normally into a cross-flow in a confined space. Whereas previous reports on the use of this method, such as that of Schaub, Kline et al (1964) have concentrated mostly on velocity measurements by tracing the motion of the hydrogen bubbles in a plane, the attempt in the present investigation was to observe the deformations in cross-sectional shape of the entering jet as it penetrates into the conduit flow. Observations were for purely qualitative purposes, and apparatus costs were kept low.

The entrainment jet was circumscribed with hydrogen bubbles produced on a wire ring (cathode) placed on the lip of the port. Both cathode and anode were mounted in the enclosed ocean box; oxygen bubbles formed at the anode (a length of steel piano wire taped to the side of the box) rose to the top of the box without disturbing the field of vision. The cathode installation is illustrated in Sketch A; the 0.005-inch wire was cemented in place on a shoulder trimmed from the lip of the port. The cement, a thinned liquid insulation (GE Electronics #176-2) was placed at six equal intervals around the wire ring, and was also used to insulate and cover

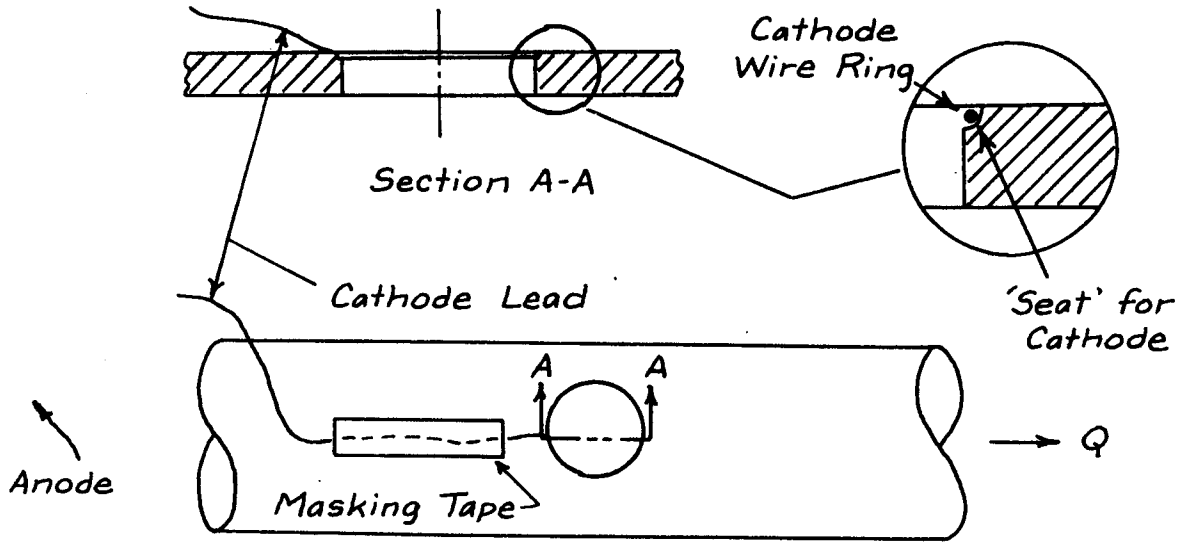

SKETCH A

all other lengths of bare wire near the port.

Cross sections of the jet were observed at various depths of penetration into the conduit by illumination with a narrow slit of light directed horizontally across the conduit at various elevations. The set-up is shown in schematic form in Fig. 26, in which the location of the camera used for attempted photographic work also is indicated. The width of the light band through the conduit was 0.25-inch as a maximum, typically smaller; refraction coefficients of the plastic and water were sufficiently close so that refraction was not a problem. The hydrogen bubbles are generated by pulsed DC currents. For a maximum bubble spacing of 0.25-inch so that a bubble would be visible in the light band at all times, a maximum average jet velocity of 10 fps required a 500 cps pulsing frequency. The circuit adopted is shown in Sketch B. The 20-volt output from the audio oscillator was amplified, and the voltage difference anode and cathode was increased to 180 volts by a small transformer. The diodes removed the positive portion of the sine wave. A sodium sulfate solution of 15 grams per liter was injected into the ocean box, causing an increase in current and decrease in voltage (to 105 volts) from the 180-volt figure which applied for fresh water throughout. As the volume of hydrogen bubbles produced is proportional to the electrical current, the salt solution was helpful to bubble generation.

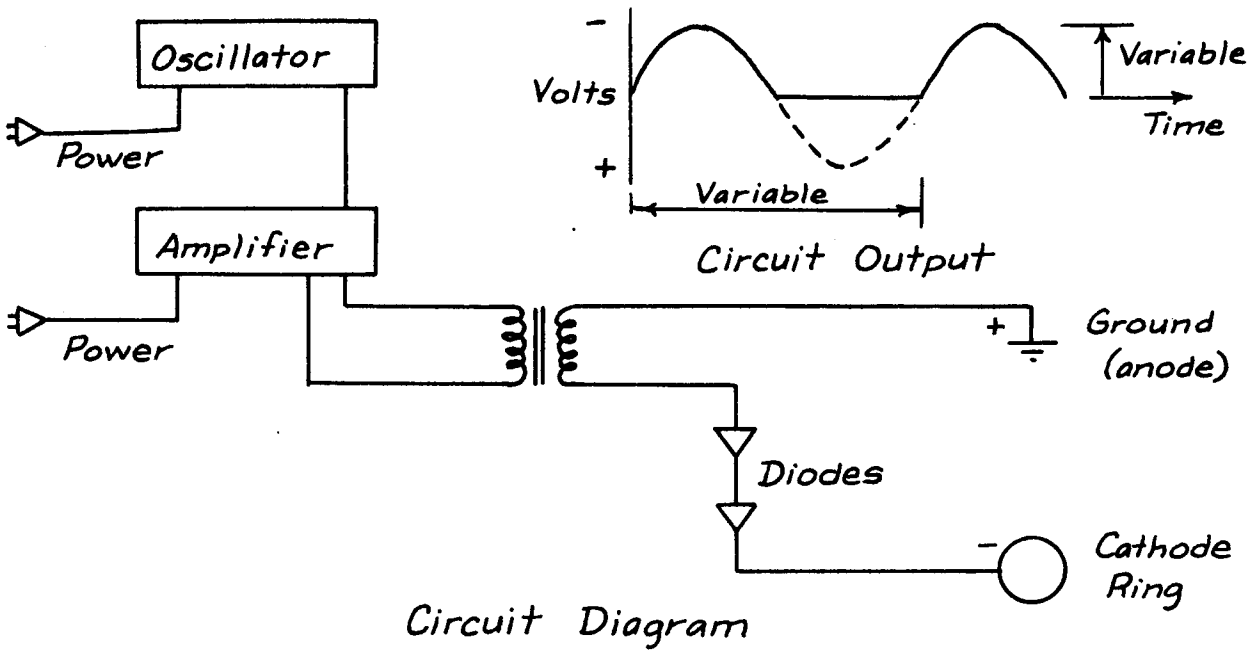

SKETCH B

The light beam was produced by mounting a 650-watt iodine vapor lamp in a hooded box open at the back and containing two independent adjustable-width horizontal slits; the adjustable slits produced a distinct beam of variable width which shown through the rear wall of the ocean box. The iodine vapor lamp was replaced with a 1000-watt flash lamp when photographs were taken in an otherwise darkened room. The angle of incidence of the light reflected from the bubbles did not allow directly downward vertical observation of the illuminated horizontal plane. As shown in Fig. 26, an angle of approximately 15 degrees from the vertical was optimum for the naked eye, and the camera was placed at a slightly greater angle to accommodate the tripod.

III. SIDE PORT MANIFOLD

A. Theoretical Analysis

A single-port manifold located in a simple outfall is shown in Fig. 12; for operation of the manifold, it is located in a "venturi" section in which conduit pressures are reduced below that of the ambient receiving water. Pertinent variables of the problem are identified in the definition sketch, Fig. 13. Two limitations must be noted in the application of Fig. 13: conventional frictional losses are neglected, and because the effective total head level of the quiscent ambient fluid is greater than that of the conduit flow the figure represents a general case, but one which is not possible in an outfall. The limitation on the general analysis for use with outfall situations will be indicated later. The treatment below is restricted to a single circular side port.

Primary interest centers on the amount of dilutant fluid which may be drawn through the port to dilute the initial conduit flow. The dependence of the port inflow on the physical variables of the problem may be stated as

$$q = q(d, D, t, r, V_o, p_e - p_o, \rho_o, \rho_e, \mu_o, \mu_e) \qquad (1)$$

in which q = the volumetric rate of entrained dilutant flow, V_o = the velocity in the conduit upstream of the port, p_e = the static pressure in the ambient fluid, p_o = the pressure in the conduit flow upstream from the port, ρ_o and ρ_e are the densities of the conduit and external fluids, respectively, and μ_o and μ_e are the corresponding viscosities; the geometry terms d, D, t and r have been defined.

Application of dimensional analysis yields eight dimensionless groups from this set of eleven variables. The first four terms within the parentheses serve to describe the geometry of a particular configuration as a particular combination of d/D, d/t, and d/r.

Five other dimensionless parameters can be formulated and which in turn may be isolated in a test program:

$$\text{Density ratio} = \frac{\rho_e - \rho_o}{\rho_o} = \frac{\Delta\rho}{\rho_o} \qquad (2)$$

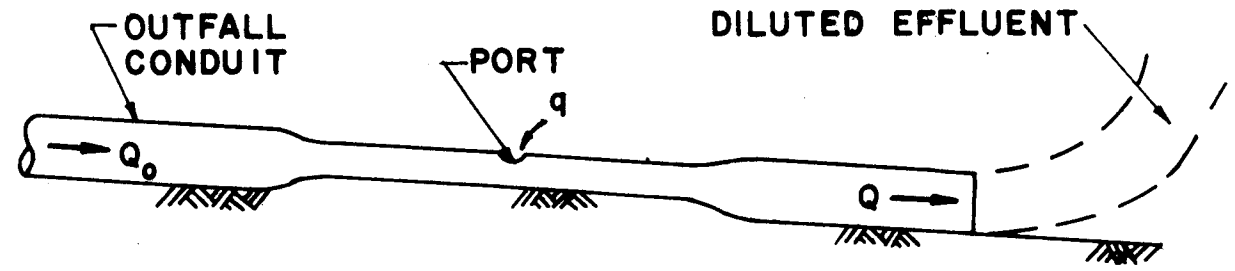

Figure 12. Side-Port Manifold in Outfall

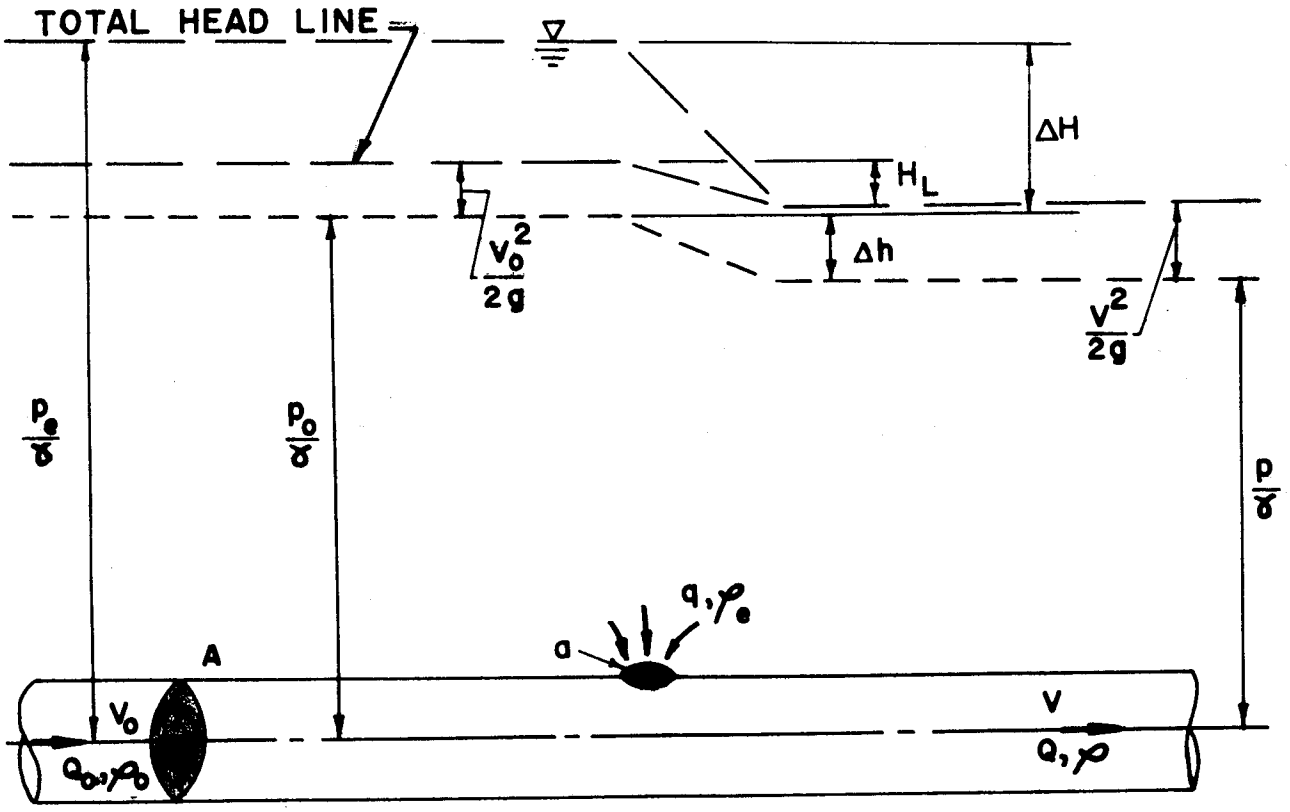

Figure 13. Definition Sketch, Side-Port Manifold

$$\text{Port Reynolds number} = \mathbb{R}_e = \frac{\rho_e \left(\frac{q}{a}\right) d}{\mu_e} \tag{3}$$

in which a = cross-sectional area $\pi d^2/4$ of the port;

$$\text{Conduit Reynolds number} = \mathbb{R}_o = \frac{\rho_o V_o D}{\mu_o} \tag{4}$$

$$\text{Euler number} = \mathbb{E} = \frac{p_e - p_o}{\frac{\rho_o V_o^2}{2}} = \frac{\Delta p}{\frac{\rho_o V_o^2}{2}} \tag{5}$$

$$\text{Entrainment coefficient} = C_e = \frac{q}{a\sqrt{\frac{2\Delta p}{\rho_e}}} \tag{6}$$

For ambient and conduit fluids of equal density, Eqs. 5 and 6 may be written, respectively, as

$$\mathbb{E} = \frac{\frac{p_e - p_o}{\gamma_o}}{\frac{\rho_o V_o^2}{2\gamma_o}} = \frac{\Delta H}{\frac{V_o^2}{2g}} \tag{7}$$

where ΔH is a pressure head difference across the port, and

$$C_e = \frac{q}{a\sqrt{2g\Delta H}} \tag{8}$$

For a given geometry the entrainment flow q would be expected to depend most significantly by the variables incorporated in $\mathbb{E}$ because the inflow velocity through the port should be proportional to $\sqrt{\Delta H}$, or $\sqrt{2\Delta p/\rho_e}$. The Euler number can be considered an approximate index of the ratio of inflow jet velocity to upstream conduit velocity. The entrainment coefficient C_e has the form of a conventional discharge coefficient. Following the reasoning above, C_e would be expected to depend upon the geometry, $\Delta\rho/\rho_o$, $\mathbb{R}_e$, $\mathbb{R}_o$, and $\mathbb{E}$. In an outfall application both the port and conduit Reynolds numbers would be sufficiently large that flow characteristics would be independent of variations in viscous effects. Practically, then, the entrainment coefficient could be expressed as

$$C_e = C_e \text{ (geometry, } \mathbb{E} \text{ , } \Delta\rho/\rho_o) \tag{9}$$

The assumed independence from Reynolds number effects would have to be verified experimentally.

Figure 13 shows that the terms Δp and ΔH are defined by the conventional procedure of extending the upstream uniform flow piezometric head line to the center of the port; this definition is retained throughout. In actuality, the effective pressure within the conduit flow as it passes the port is reduced below that predicted by the conventional procedure because the stream entering laterally from the port occupies some of the conduit cross-section area and hence reduces the effective flow area in the conduit.

The ratio of the dilutant flow rate q to the sum of q and Q_o is defined as the dilution ratio. In terms of the volumetric continuity equation

$$Q = Q_o + q \tag{10}$$

in which Q_o and Q are the conduit flow rates upstream and downstream from the port, respectively, the dilution ratio may be expressed as

$$\frac{q}{Q} = \frac{q}{Q} = \text{(geometry, } \mathbb{E} \text{ , } \frac{\Delta\rho}{\rho_o} \text{)} \tag{11}$$

if once again variations in viscous effects may be neglected.

Momentum and energy equations, along with simplifying assumptions, may be used in a one-dimensional flow analysis to give expressions for conduit pressure drop across the port and for the conduit head loss associated with the lateral inflow through the port. The results of such an analysis are given below, and are the same as those given by McNown (1954) in a study of pipe manifolds in which there was a combining of flows from a continuing straight pipe and from a single pipe lateral perpendicular to the conduit. The following assumptions are inherent in Eq. 12 and apply to the control volume shown in Sketch C; the control volume is extended to where the velocity is everywhere essentially zero in the ambient fluid.

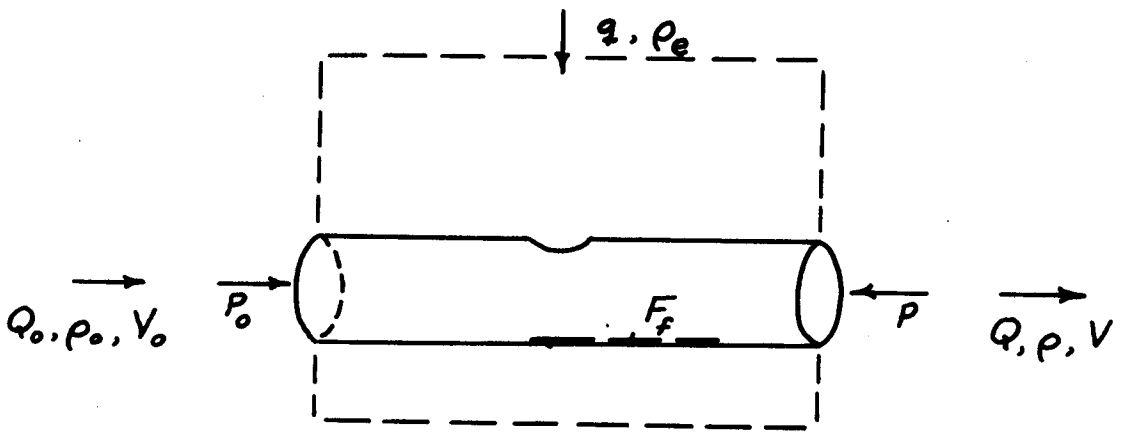

SKETCH C

1. Uniform velocities exist over the conduit where these velocities are V_o and V, respectively, with corresponding pressures p_o and p; full mixing of the initial conduit flow and port flow is assumed where the velocity is V.
2. Boundary shear stresses due to pipe friction are assumed to be zero; all other boundary forces, such as those due to pressure distribution on the port lip and non-uniform conduit wall shear stress distribution associated with directional changes and dissipation of the entering jet, are accounted for by the F_f term (F_f is considered positive if acting upstream).
3. The entrained fluid has zero initial momentum in the direction of the conduit flow.

It is noted that in a real flow case the head losses calculated by the resulting equations must be superposed on frictional losses calculated on the basis of uniform flows in the conduit both upstream and downstream from the port. The momentum equation consistent with the listed assumptions is (with A = the conduit area):

$$p_o A - pA - F_f = (\rho_e q + \rho_o Q_o)V - \rho_o Q_o V_o \qquad (12)$$

Simultaneous solution of Eqs. 10 and 12 yields

$$\frac{p_o - p}{\frac{\rho_o V^2}{2}} = 2\frac{q}{Q}\left(1 + \frac{\rho_e}{\rho_o} - \frac{q}{Q}\right) + \frac{2F_f}{\rho_o QV} \qquad (13)$$

When the two fluid densities are nearly the same ($\Delta\rho \approx 0$), Eq. 12 reduces to

$$(p_o - p)A = \rho_o Q V - \rho_o Q_o V_o + F_f \tag{14}$$

Solution of Eqs. 10 and 14 yields

$$\frac{p_o - p}{\frac{\rho_o V^2}{2}} = \frac{\Delta h}{\frac{V^2}{2g}} = 2\frac{q}{Q}\left(2 - \frac{q}{Q}\right) + \frac{2F_f}{\rho_o Q V} \tag{15}$$

where Δh is defined as the piezometric head loss due to the port inflow. Equations 13 and 14 are identical when $\Delta\rho = 0$.

The one-dimensional energy equation for the conduit flow may be written

$$\frac{p_o}{\gamma_o} + \frac{V_o^2}{2g} = \frac{p}{\gamma} + \frac{V^2}{2g} + H_L \tag{16}$$

in which H_L is the additional head loss caused by the port inflow and which is not included in the uniform flow frictional losses. When $\Delta\rho = 0$, simultaneous solution of Eqs. 10, 15 and 16 yields

$$\frac{\frac{H_L}{V^2}}{\frac{V^2}{2g}} = \frac{q}{Q}\left(2 - \frac{q}{Q}\right) + \frac{2F_f}{\rho_o Q V} \tag{17}$$

Equations 15 and 17 give first approximations of the head drops along the conduit if the F_f term is ignored. Further, the assumption of $F_f = 0$ for a multiple port manifold is equivalent to ignoring all frictional losses between ports in the manifold; therefore, Eqs. 15 and 17 are suitable for multiple port manifolds as well when the losses are those associated with inflows only and when $q|Q$ is replaced by $\Sigma q|Q$, where Σq is the sum of the individual port inflows. Because these equations (with $F_f = 0$) are independent of the port geometry, it is logical to expect that different port configurations would yield different experimental results.

With respect to possible outfall applications, it must be noted that the conduit velocities included in the above equations would be those existing in the manifold section of the outfall (as shown in Fig. 12) and therefore are larger than the velocities in the regular sections of the outfall conduit.

Further, in an outfall application, the velocity head $V_o^2/2g$ in the manifold must be greater than the driving head across the port, ΔH, causing the entrainment. The Euler number was defined in Eq. 7 as the ratio of this driving head to the velocity head in the approaching manifold flow. Conduit friction and exit losses therefore limit the maximum value of E in an outfall installation to less than 1.0. (Figure 13 shows a case where $E > 1.0$). There was no limit on E in the simple analysis listed above, and test values were obtained for $E > 1.0$, so that the study was not restricted solely to the range of possible outfall applications.

B. Experimental Results: Hydraulic Characteristics of Single-Port Manifolds

The six side port configurations tested were discussed in Section B of Chapter II; specific dimensions have been listed in Table I.

Data for all six ports were obtained for the case of $\Delta\rho/\rho_o = 0$. Salt water runs to investigate effects of density differences were made for some square-edged ports. The density differentials used corresponded to $\Delta\rho/\rho_o$ ratios of 0.015, 0.030, and 0.042; these ratios cover the range of values which would be present in ocean outfalls.

Conduit approach velocities, V_o, were in the range of 1-6 fps for all runs; upstream Reynolds numbers thus were within the range $10^4 < R_o < 10^5$, so conduit flows were definitely turbulent. Port Reynolds numbers R_e varied over the approximate range $2 \times 10^3 < R_e < 4 \times 10^4$. For plane circular orifices, the data of Lea as presented by Rouse (1946) show that in this range the discharge coefficient varies from 0.70 to 0.62 as the Reynolds number increases, compared with an asymptotic value of 0.61 at high Reynolds numbers. The data of the present tests show that C_e depends upon E and not upon R_e; e.g., at equal values of R_e, corresponding at times to widely varying E values, a wide range of C_e values was obtained. There was no correlation between R_e and C_e. Therefore, it seems reasonable to extrapolate the C_e vs. E relationships shown in this section without change of values to physically larger ports for which R_e values also would be higher. Likewise, negligible effects on head drop characteristics would be expected.

Entrainment coefficients are plotted as functions of the Euler number for all six ports tested in Fig. 14. Each experimental curve is based on a

minimum of twenty points. Individual points are shown for the d/D = 1 case only; test data for the other geometries had less scatter than did the points plotted. Figure 14 is for the case $\Delta\rho/\rho_o = 0$.

All six ports have comparable trends in entrainment characteristics. Asymptotic values of C_e are approached at very high E values; maximum values of C_e are reached when $E \approx 1$; and in all cases, C_e decreases as E approaches zero. At the limiting value of $E = 0$, of course, C_e is indeterminate. A phenomenological, semi-empirical model predicting the trend of C_e vs. E over the full range of Euler numbers has been presented elsewhere by Nece, Goldstern, and Black (1966). The results of that argument, based upon the results summarized in the present report, are not summarized here. However, a brief discussion will indicate the reasons for the observed data trends.

The Euler number has been shown to be an index of the ratio of velocities (or, more properly, velocities squared) of the inflow jet to that of the conduit approach flow. At very high E values the jet penetrates across the conduit and is essentially normal to the conduit axis. For such conditions the effective flow area of the conduit discharge past the jet is a constant and minimum so that the effective head differential across the port is significantly greater than ΔH; under these conditions the side port behaves akin to a conventional orifice, and it is expected that little change would occur in C_e over a fairly wide E range. In the neighborhood of $E = 1$, however, conditions of the jet are markedly different. Jet and conduit approach flow velocities are nearly equal, so the jet has a pronounced deflection in the downstream direction as it enters the conduit. Reductions in effective driving head as well as in jet cross sectional area occur. For low Euler numbers ($E < 1$), the inflow jet is deflected even more and so tends to hug the top of the conduit; effective jet areas through the port are reduced and there is little increase in effective driving head over that computed by the conventional methods described. Consequently, there is a monotonic decrease of C_e as E decreases.

All four square-edged ports have maximum C_e values in the vicinity

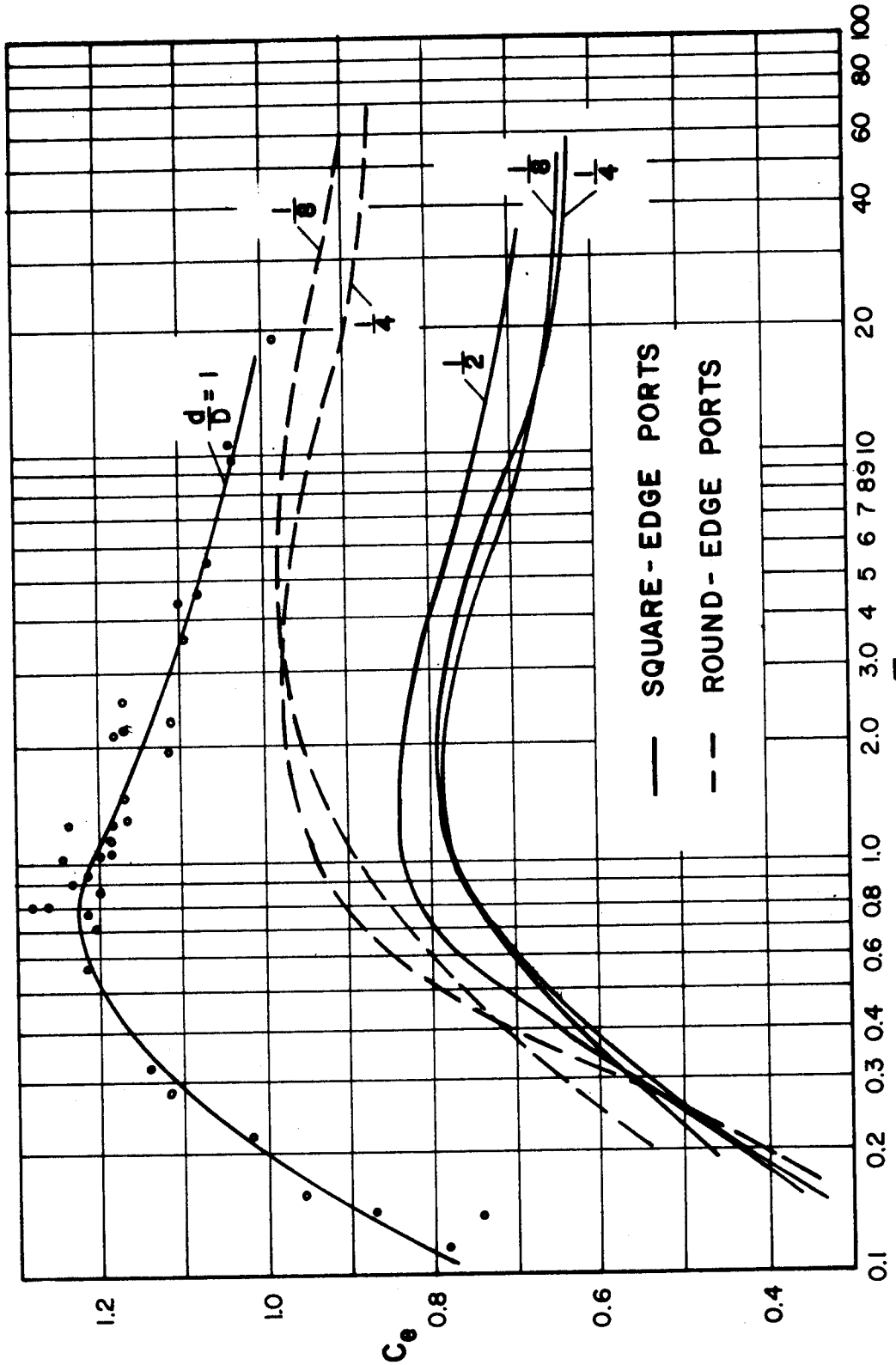

Figure 14. Entrainment Coefficient vs. Euler Number

of $\mathbb{E}$ = 1; asymptotic C_e values for high Euler numbers are approximately 0.64, 0.63, and 0.68 for the cases of d/D = 1/8, ¼, and ½ respectively. The peak $\mathbb{E}$ value obtainable for the d/D = 1/1 port was less than 20. Values of C_e for this largest port are noticeably higher than for the other square-edged ports; the area definition of $a = \pi d^2/4$ used in all calculations is not realistic with respect to observed flow patterns.

Approximate asymptotic C_e values for the two rounded-edge ports at high Euler numbers are 0.90 and 0.87 for the ports of d/D = 1/8 and ¼, respectively. These values are slightly lower than might be expected for bell-mouth orifices, so the contour of the conduit outer wall seems in part to override the degree of rounding at the port lip.

Values of the dilution ratio for a given configuration at particular Euler numbers also may be calculated by inserting the experimentally determined values of C_e in

$$\frac{q}{Q} = \frac{C_e\, a\, \sqrt{2g\Delta H}}{Q_o + q} = \frac{\mathbb{E}^{\frac{1}{2}}}{\frac{1}{C_e}\left(\frac{D}{d}\right)^2 + \mathbb{E}^{\frac{1}{2}}} \qquad (18)$$

Dilution ratios are shown as functions of $\mathbb{E}$ for three of the ports tested in Fig. 15; the curve drawn for d/D = ½ with an assumed constant value of C_e = 1.0 emphasizes that effects of varying C_e are most pronounced at the lower Euler numbers.

Test data in the range $\mathbb{E}$ < 0.1 were very limited, mostly due to the lack of accuracy possible with the test set-up. Dilution ratios for such low $\mathbb{E}$ values become very low, so there was little incentive to extend the test range downward because of reduced possible interest in outfall applications for the continually decreasing dilution rates obtained.

The effect of density differences on entrainment behavior is shown in Fig. 16, which gives results for the square-edged port of d/D = ¼. The plotted curve is taken from Fig. 14; experimental points are shown for $\Delta\rho/\rho_o$ ratios of 0.015, 0.030, and 0.042. These points essentially follow the $\Delta\rho/\rho_o$ = 0 curve, although C_e is slightly higher than for the zero density differential case for $\mathbb{E}$ < 1, and somewhat lower for $\mathbb{E}$ > 2

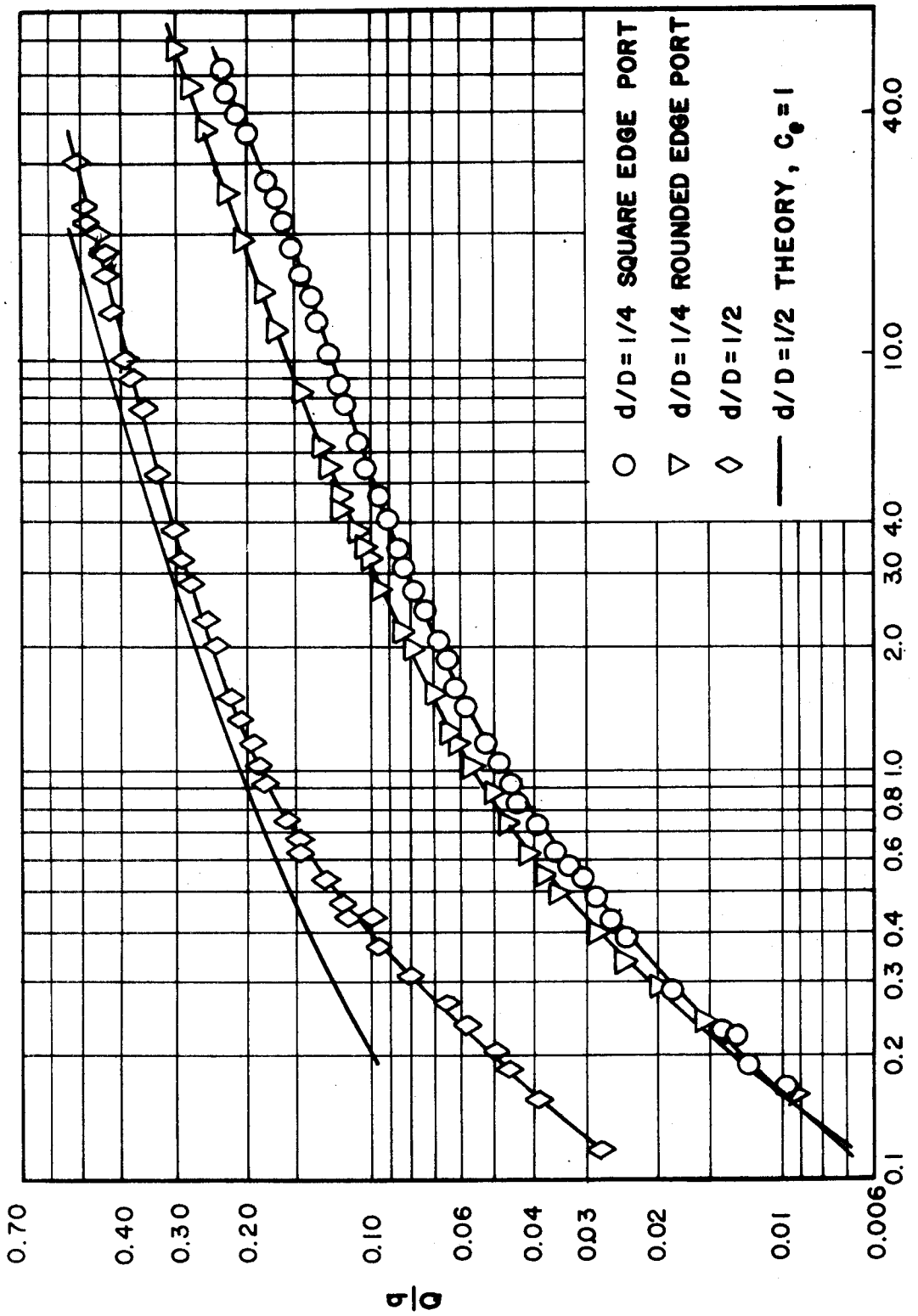

Figure 15. Dilution Ratio vs. Euler Number

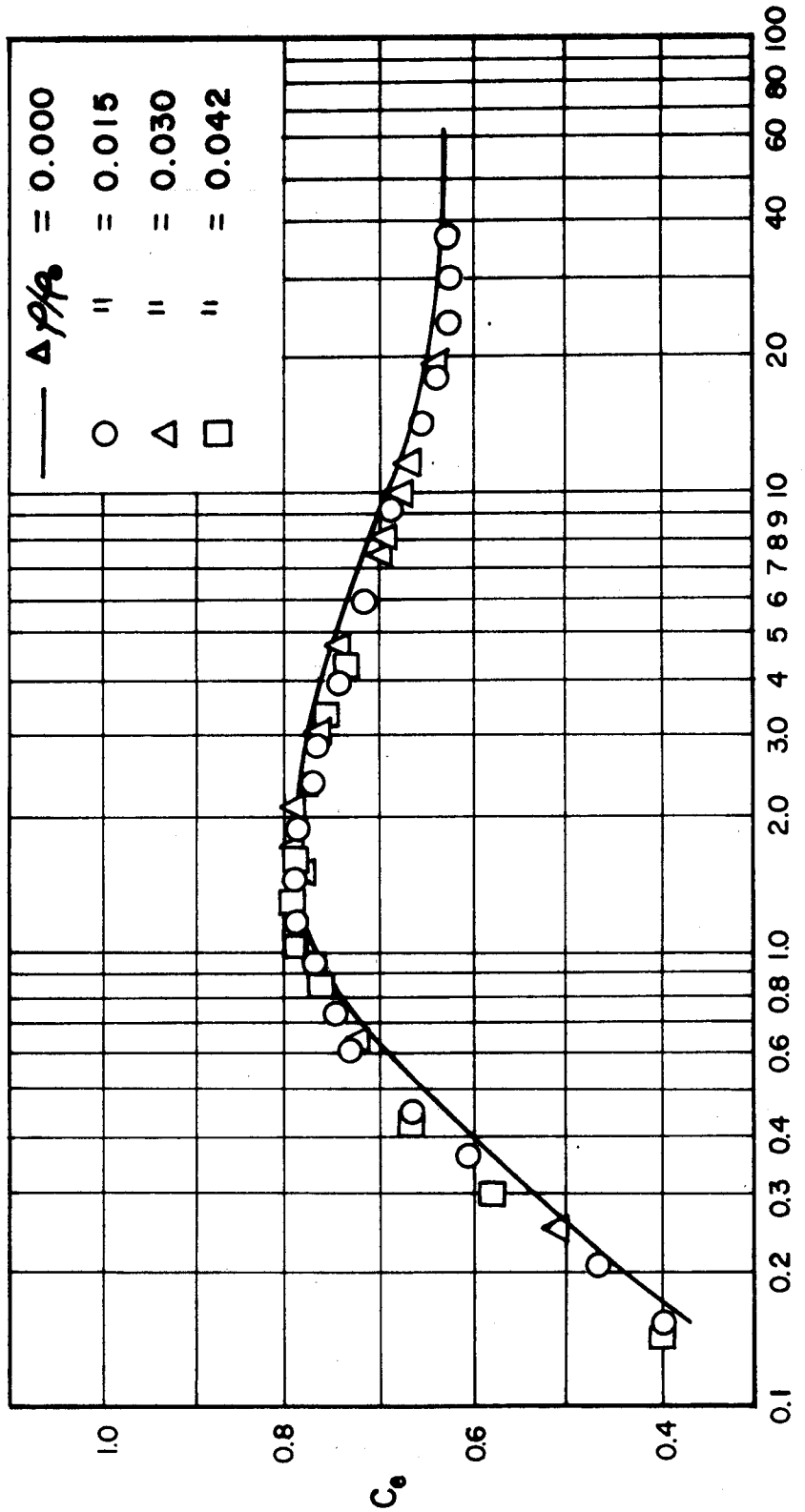

Figure 16. Effect of Density Differential on Entrainment Coefficient

although approaching the same asymptote at high Euler numbers. The differences at the smaller E values are logical because the "heavier" jet tends to enter the conduit flow in a direction more normal to the approach velocity. The pressure differential $p_e - p_o$ was defined in the density differential runs as the difference between the box pressure and the conduit pressure, both measured at the elevation of the top of the conduit.

No consistent trend of variations in C_e with $\Delta\rho/\rho_o$ was observed over the density ranges tested. Therefore, for the density ranges encountered in marine outfalls, the zero density differential case results should be adequate, at least for any preliminary design calculations. In the range $E < 1$, as seen in Fig. 16, the $\Delta\rho/\rho_o = 0$ results would give slightly conservative results.

Some piezometric head drop data are shown in Figs. 17 and 18. Figure 17 is for the $d/D = \frac{1}{2}$ port, and illustrates the effect of density differentials. For each case ($\Delta\rho/\rho_o = 0$ and $\Delta\rho/\rho_o = 0.042$) the theoretical curves were determined from Eq. 13, with the assumption of $F_f = 0$. The relative increase in head drop due to increased density differential is predicted quite well by the theoretical expression. This increased head drop due to a more dense ambient liquid is only a few percent of the downstream conduit velocity head and is negligible in the range of applicability to a marine outfall; again, $\Delta\rho/\rho_o = 0$ values would suffice for initial calculations.

Figure 18 shows data for three ports, all for the $\Delta\rho/\rho_o = 0$ case. The effect of relative diameter, d/D, is apparent; the $d/D = \frac{1}{2}$ case tends to follow the one-dimensional prediction of Eq. 15, with $F_f = 0$, as shown on Fig. 17. The effect of rounding the port edge is also apparent. The simple analytical model result is independent of the actual geometry (i.e., relative diameters, and/or lip form), depending solely upon the dilution ratio. The fact that the experimental piezometric head drops are considerably larger than those predicted by the simple theory, especially so for the smaller ports, is due to entrainment velocities being much higher for smaller ports at equal dilution ratios; the jet penetration is more perpendicular to the conduit axis, and the resulting higher velocities reaching the opposite wall induce relatively higher boundary shear stresses at the wall. Increased pressure drops are associated with these larger shear stresses (i.e., relatively

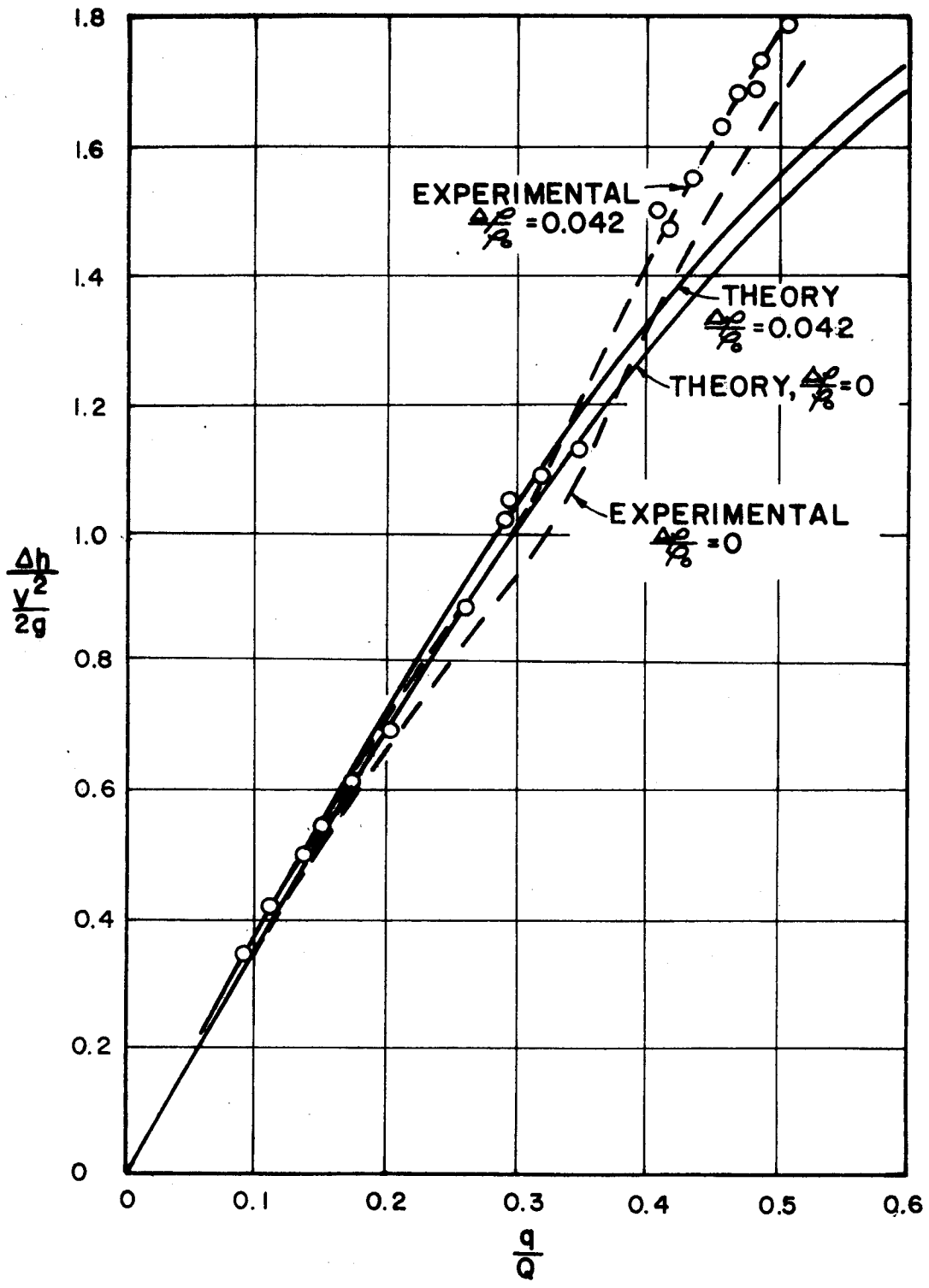

Figure 17. Effect of Density Differential on Piezometric Head Drop

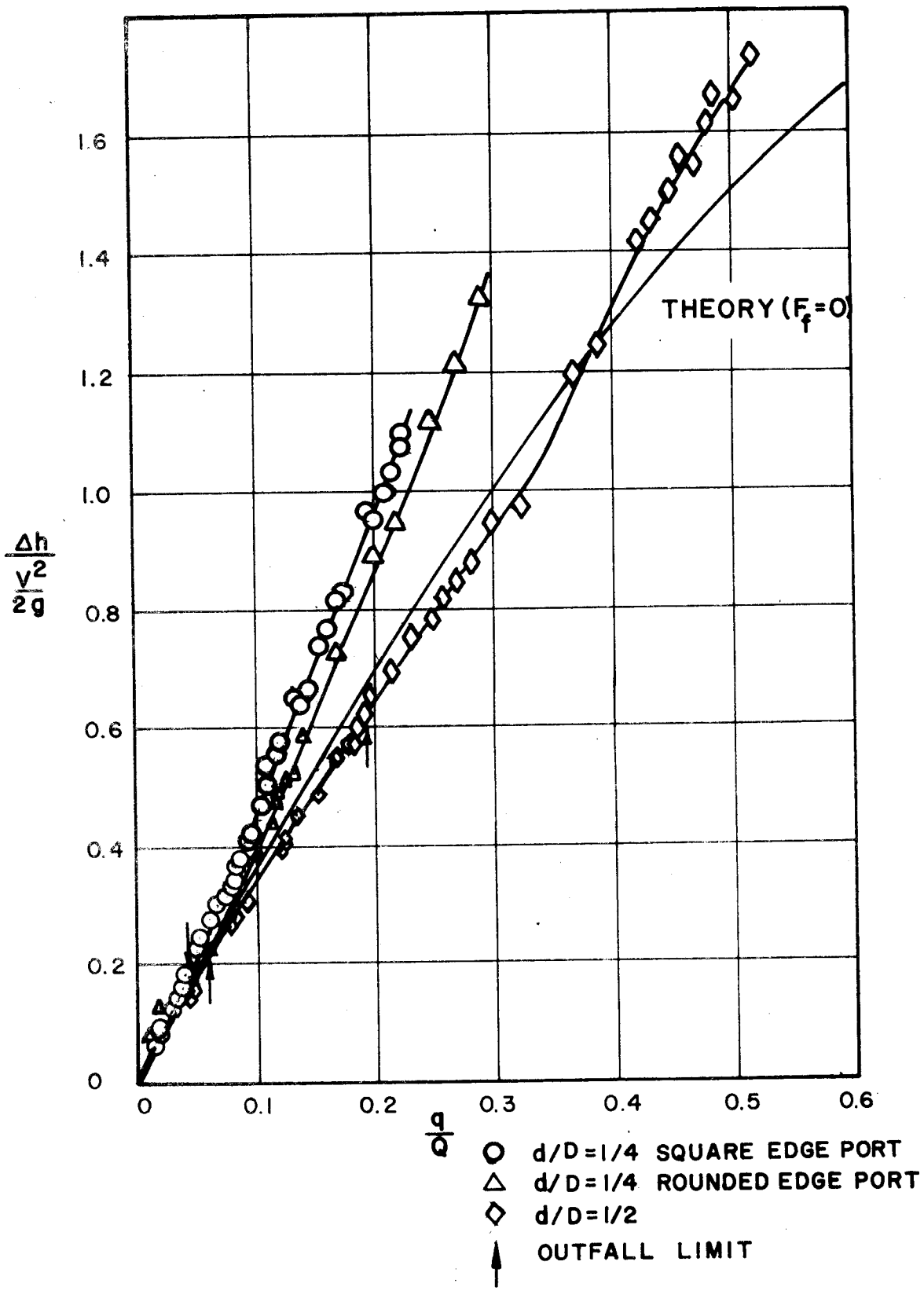

Figure 18. Effect of Port Size and Lip Rounding on Piezometric Head Drop

larger F_f term). Limits of outfall operation ($E = 1$) are shown on Fig. 18 for the three ports; again, differences between measured head drops and those predicted by the theory are very small in the range of outfall use.

Dimensionless head loss characteristics of the ports tested are shown in Fig. 19. All data are for the case $\Delta\rho/\rho_o = 0$; in each part of the diagram, predicted results from Eq. 17 are plotted, again assuming $F_f = 0$. Larger relative head losses occur for the smaller ports, as indicated above. For all diameter ratios except d/D = 1/8 the present data also are compared with head loss results for 90° pipe laterals. These latter results, labeled "Iowa" and "SAF" (St. Anthony Falls Hydraulic Laboratory), have been presented by McNown (1954) and by Blaisdell and Manson (1963), respectively.

The curves indicate relative efficiencies, with respect to head loss, of the two types of manifolds -- i.e., pipe junctions and suction ports. For the smallest ports it may be concluded that changes in the initial shape of the entering jet between port and pipe lateral inflows do not markedly affect the flow field in the conduit and around the jet and therefore head loss characteristics are quite comparable. As d/D increases, the port losses become larger than those with pipe laterals and in general are larger than predicted by Eq. 17. Higher losses for d/D = 1/8 than for d/d = ¼ at equal ratios of q/Q again reflect a greater degree of jet penetration from the smaller port into the main conduit flow and also relatively higher jet velocities which must be dissipated by turbulent mixing and, in part at larger E values, increased boundary shear stresses on the conduit wall opposite the port. At the larger d/D ratios, the reduced efficiency of the port compared to the pipe lateral is expected because the momentum of the entrained flow in the upstream direction increases with port size. For the d/D = 1/1 case, this condition is less prevalent because almost all entrained flow enters the conduit through the downstream part of the non-planar port opening.

The experimental results for q/Q, E, Δh, and H_L for all six configurations tested are plotted in the four-quadrant diagrams of Figs. 20 and 21. All curves summarize test data and cover the ranges tested. The first and fourth quadrants relate Euler numbers and head drops; the second

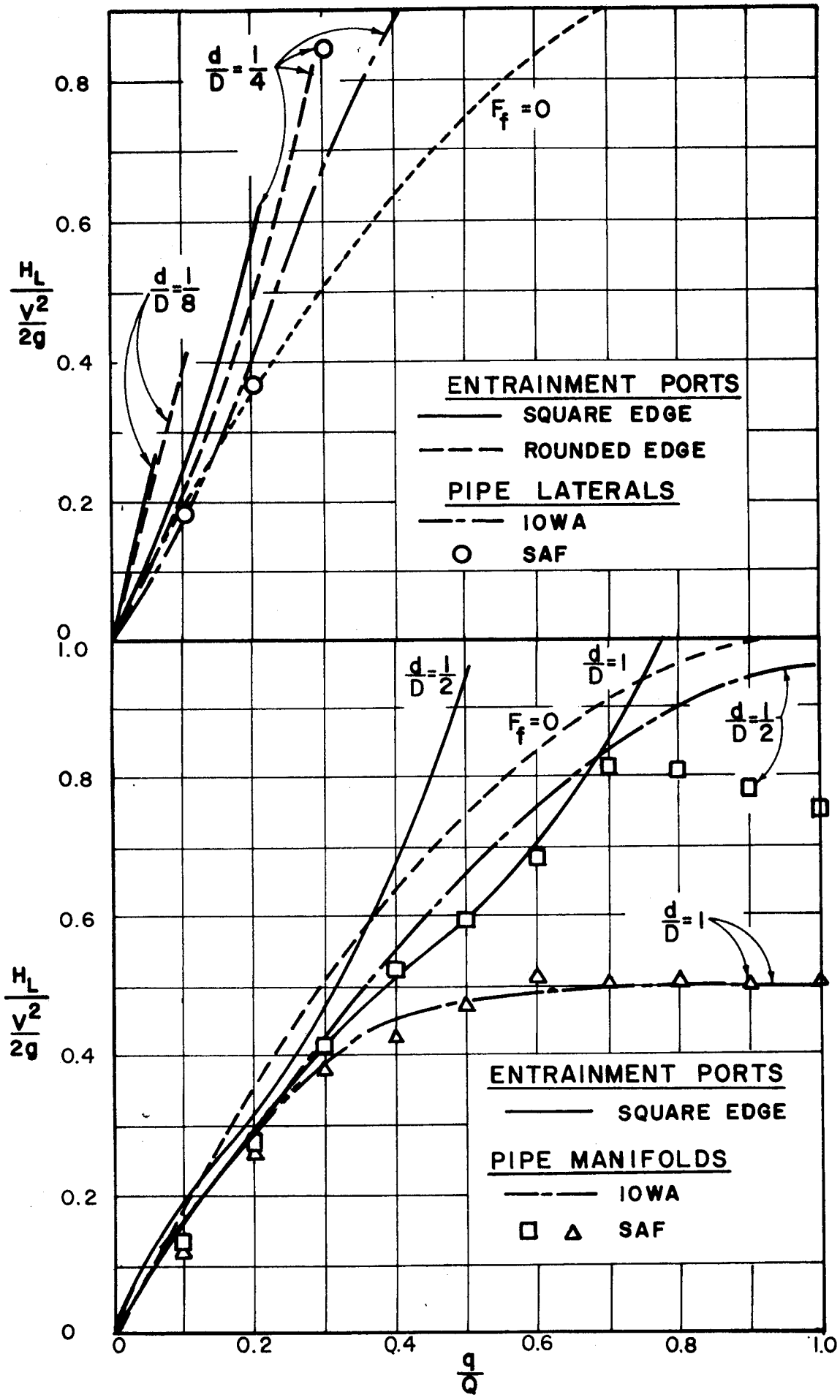

Figure 19. Head Loss Characteristics of Single Side Ports

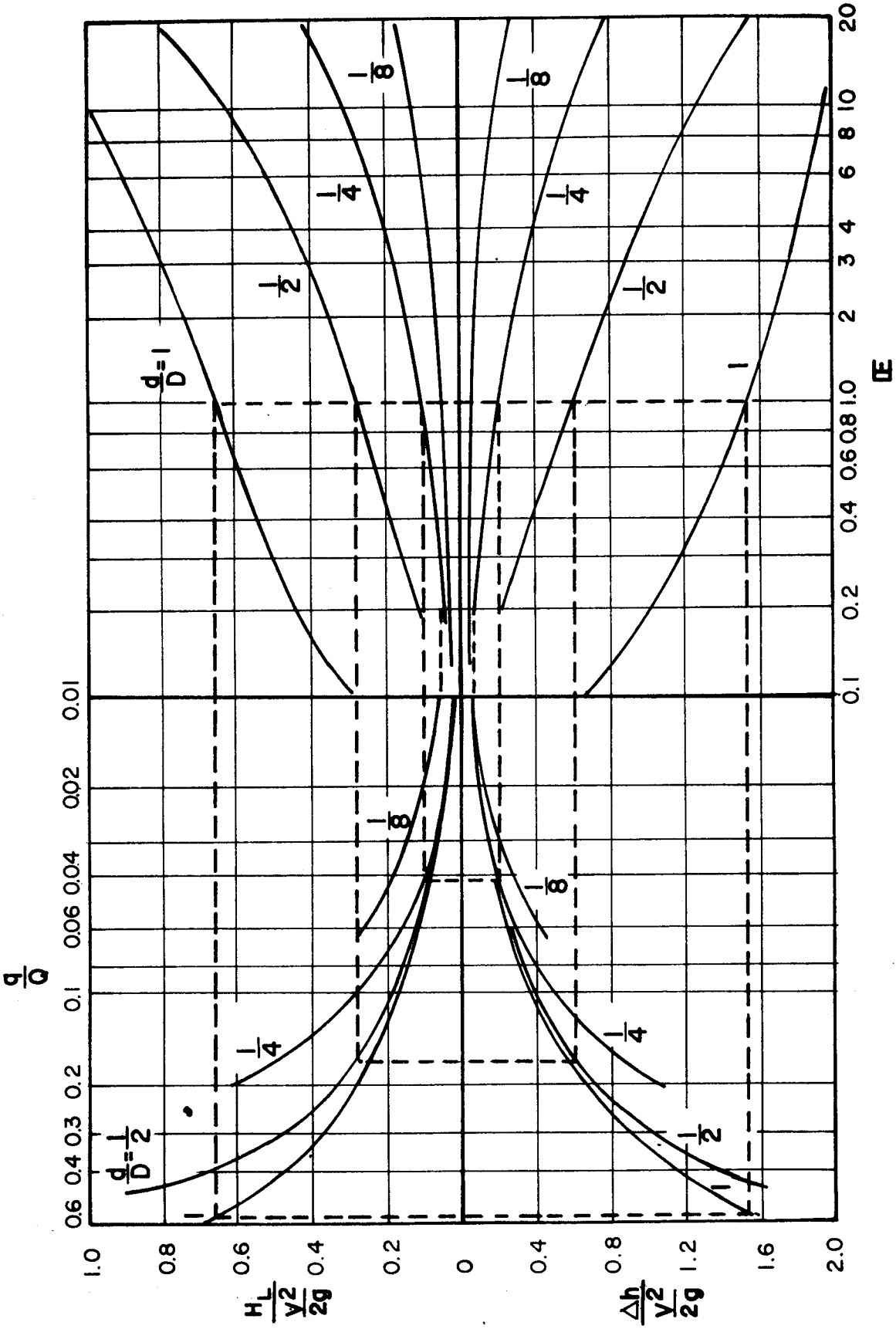

Figure 20. Experimental Result Summary: Performance Characteristics of Single Square-Edged Ports

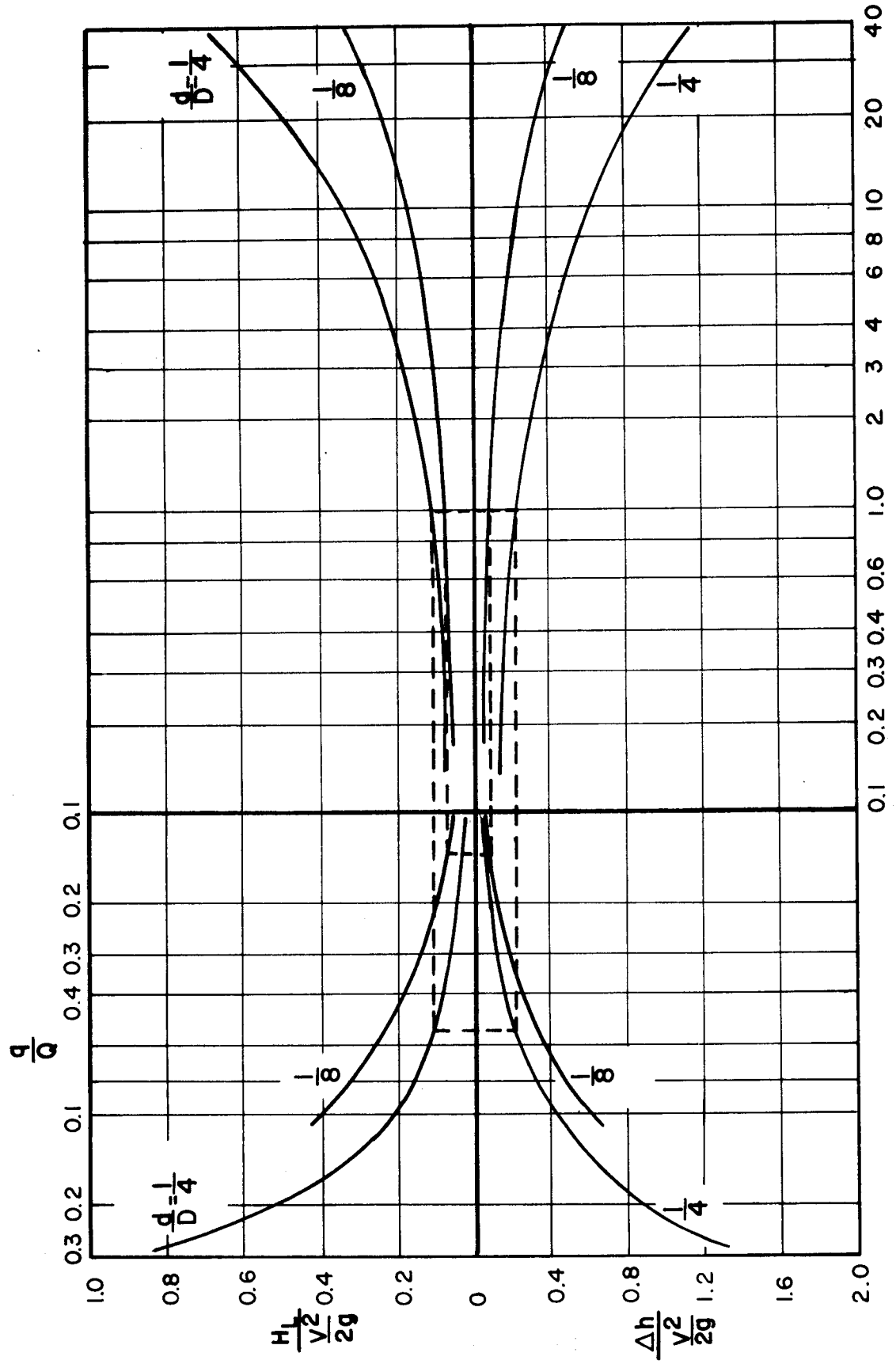

Figure 21. Experimental Result Summary: Performance Characteristics of Single Round-Edged Ports

and third quadrants relate the dilution ratio q/Q to these head drop terms, Δh and H_L, which are plotted in the dimensionless forms used in Eqs. 15 and 17, respectively. All four parameters for a particular port geometry can be determined if one of the parameters is either known or assumed. The dashed lines on the plots link the results for $\mathbb{E} = 1$, and thus delineate the regions of the diagrams lying within the limits of outfall applications.

Data for the four square-edged ports are shown in Fig. 20. Limiting values of q/Q at $\mathbb{E} = 1$ are 0.012, 0.047, 0.18, and 0.55, respectively, in ascending order of port size. These limiting dilution ratios follow approximately the progression of the port area ratio, a/A. The performance of ports having intermediate diameter ratios can be estimated by interpolation. For example, if a dilution ratio of 40% were desired at $\mathbb{E} = 1$, the required port size could be expressed as d/D = 0.8.

Rounded-edge port data are summarized in Fig. 21. The dilution ratios at the limiting value of $\mathbb{E} = 1$ are q/Q = 0.015 and 0.055 for d/D = 1/8 and ¼, respectively.

C. Experimental Results: Hydraulic Characteristics of Multiple-Port Manifolds

Experimental results for the multiple-port manifolds listed in Table II are summarized on the four-quadrant diagrams of Figs. 22, 23, and 24 for which the d/D ratios are 1/8, ¼, and ½ respectively. As with the comparable figures for the single-port manifolds, Figs. 22-24 span the experimental ranges covered in the tests. All data were obtained for the case $\Delta\rho/\rho_o = 0$.

The first quadrant relates the dimensionless head loss for the entire manifold, $\left(H_{L_{1-n}}\right) / \left(V_n^2/2g\right)$ to the Euler number at the upstream port, $\mathbb{E}_1$. Here, $\mathbb{E}_1$ is defined in the same way as for a single port, n is the number of ports in a particular manifold, and V_n is the mean conduit velocity downstream of the n-th port. The fourth quadrant relates the dimensionless total head loss to the total dilution ratio for the manifold, $\Sigma q/Q$. The third quadrant relates the dilution to the total piezometric head drop across the entire manifold. The arrangement of these three quadrants allows determination of head loss and pressure drop for a particular manifold when either $\Sigma q/Q$ or $\mathbb{E}_1$ is known. The head differential terms presented in the three

figures are those associated with the port inflow only, and frictional losses between the ports have been excluded. Calculations for total head losses in a particular manifold would require that frictional losses between ports be calculated by application of the Darcy-Weisbach equation and that the friction drops so calculated be added to those shown on the figures.

The second quadrant applies to multiple-port manifolds only and relates Euler numbers of the various ports in a particular manifold. Such information is necessary because the Euler number at each port must be less than unity. The coaxial plot is discontinuous in the second quadrant, and E_n cannot be related directly to any drops. As with Figs. 20 and 21 for the single-port manifolds, dashed lines on Figs. 22-24 indicate limiting conditions for a possible outfall application: namely, $E_n = 1.0$. Further, because of the definition of the Euler number, it is necessary to include friction drops in the determination of E_n. This was done in the plotting of the second quadrant in each of Figs. 22-24, using appropriate values of f (0.019-0.025 for the laboratory runs). The procedures used have been outlined in Section D of Chapter II; effects of a port upon the port downstream from it are automatically accounted for in the equations defining C_e and Δh.

The double-port manifolds had head loss characteristics so similar for the X/D values of 2.5 and 5.0 that the results are shown as single curves in Figs. 22-24. However, because friction losses are included in the determination of E_2, slight differences in the results for the two X/D spacings are shown in the second quadrant. Differences are largest at low Euler numbers where friction losses are more important in the calculation of E_2. Further, the curves in the second quadrant would be different for other quadrants if f is significantly different from the values for these data.

Conditions at $E_n = 1.0$, as delineated on Figs. 22-24, may be used to compare the performances of the multiple-port manifolds tested; this comparison of experimental results is shown in Table IV. A performance ratio e, defined as

$$e = \frac{(\Sigma q/Q)}{\left(\frac{H_{L_{1-n}}}{\frac{V_n^2}{2g}}\right)} \qquad (19)$$

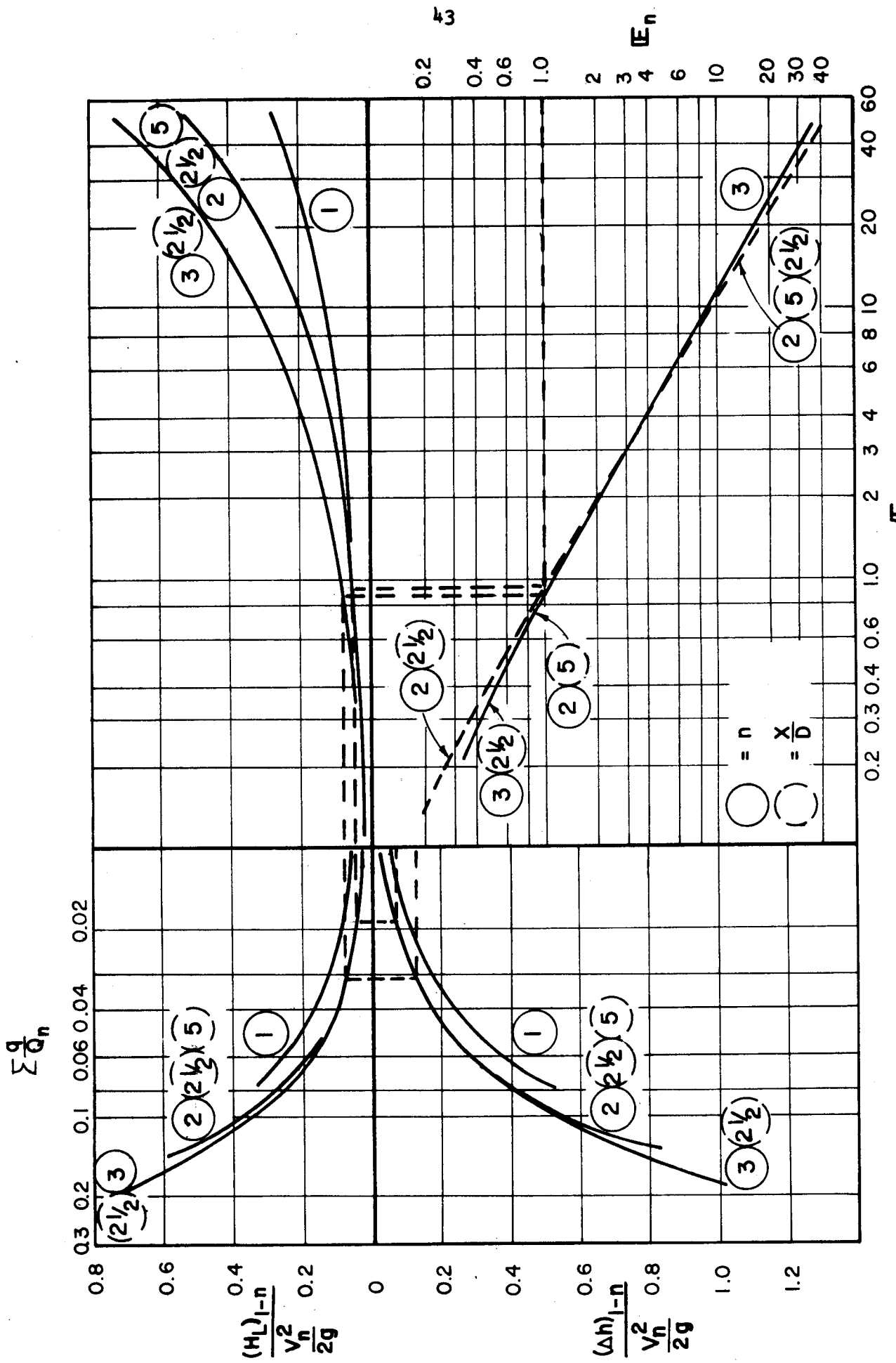

Figure 22. Experimental Result Summary: Multiple-Port Manifolds, d/D = 1/8

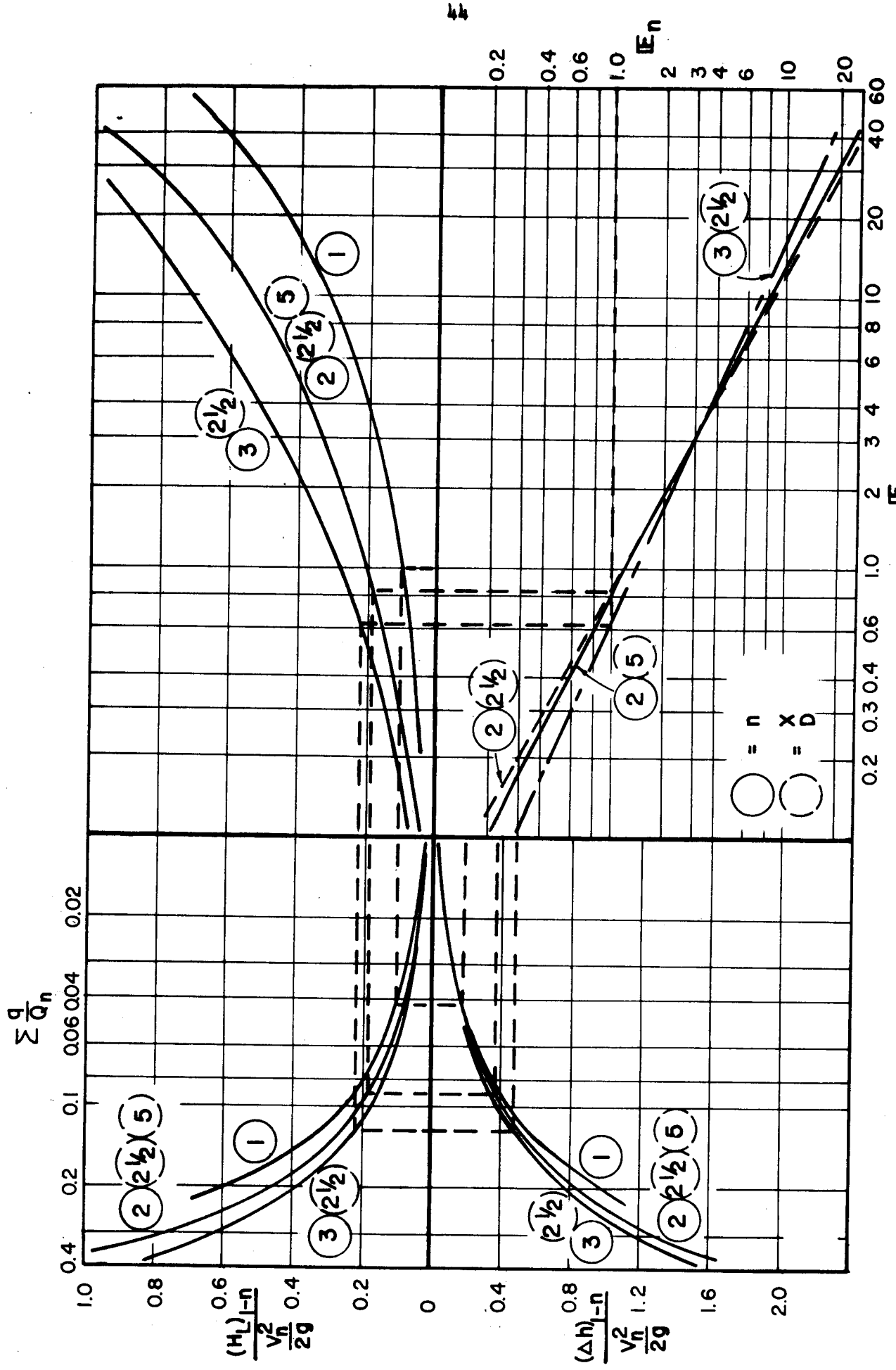

Figure 23. Experimental Result Summary: Multiple-Port Manifolds, d/D = ¼

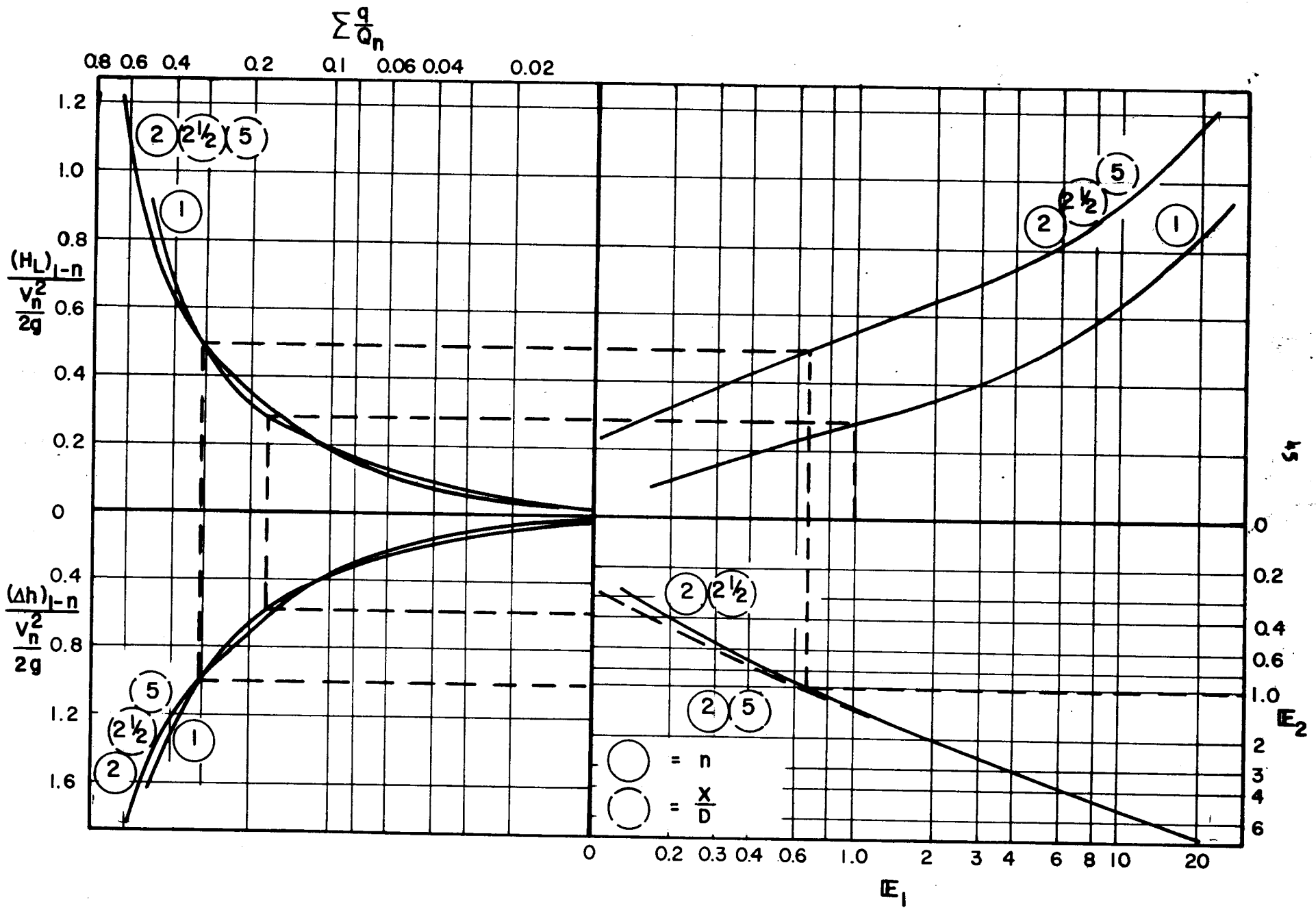

Figure 24. Experimental Result Summary: Multiple-Port Manifolds, d/D = ½

is used as an index of relative performance. Included in Table IV are values of friction losses between the extreme ports of a manifold assuming f = 0.02. These values illustrate relative magnitudes of friction losses in comparison to entrainment losses. Friction losses are relatively major for the small ports, minor for the large ports. If frictional losses are included, the large ports have a better relative (effective) performance as shown by the e_{eff} column in Table IV.

Table IV

Performance Comparison , $E_n = 1.0$

$\frac{d}{D}$	n	$\frac{X}{D}$	E_1	$\frac{\Sigma q}{Q}$	$\frac{H_{L_{1-n}}}{\left(\frac{V_n^2}{2g}\right)}$	e	$\frac{h_{f_{1-n}}}{\left(\frac{V_n^2}{2g}\right)}$	e_{eff}
1/8	1	-	1.00	0.012	0.05	0.24	-	0.24
	2	2.5	0.94	0.019	0.05	0.38	0.05	0.19
	2	5.0	0.94	0.019	0.05	0.38	0.10	0.13
	3	2.5	0.88	0.031	0.08	0.40	0.10	0.17
¼	1	-	1.00	0.047	0.10	0.47	-	0.47
	2	2.5	0.81	0.090	0.18	0.50	0.05	0.39
	2	5.0	0.81	0.090	0.18	0.50	0.09	0.33
	3	2.5	0.62	0.125	0.22	0.57	0.09	0.40
½	1	-	1.00	0.18	0.28	0.65	-	0.65
	2	2.5	0.62	0.31	0.48	0.65	0.04	0.60
	2	5.0	0.62	0.31	0.48	0.65	0.07	0.56
1/1	1	-	1.00	0.55	0.65	0.85	-	0.85

Entrainment coefficients were calculated for the downstream ports in the multiple-port manifolds. The results are not shown here, as the four-quadrant diagrams Figs. 22-24 contain sufficient data for calculation purposes. Briefly, however, C_e values calculated by procedures outlined tended to be higher for the downstream ports and the higher values tended to occur at

consistently lower values of E (curves of C_e vs. E , as in Fig. 14, are displaced upward and to the left). This is because, in calculations, the pressure drops due to entrainment are assumed to occur entirely at the port; the actual pressure gradient along the conduit in the vicinity of a port is much different. Goldstern (1963) made pressure measurements which showed that the piezometric grade line appears as shown qualitatively in Sketch D. Although differences between the calculated and effective pressure grade lines are exaggerated in the sketch, some indication of the previously discussed performance of a single port is indicated as well as the fact that because the effect on the conduit pressures is felt for some distance downstream it is apparent that ΔH values for any relatively close downstream port are greater than those calculated by the conventional procedures already outlined. Apparent shifts in the C_e - E relationship for downstream ports can be explained qualitatively by this explanation.

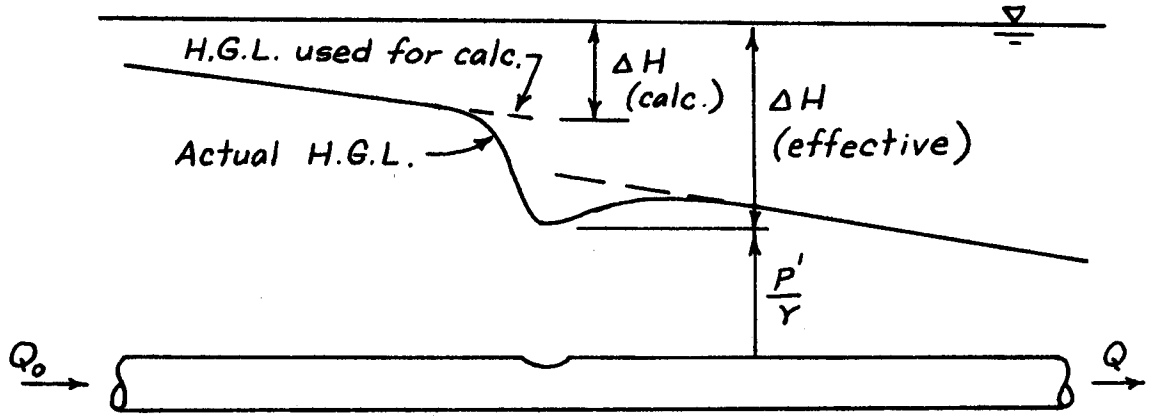

SKETCH D

D. Mixing Studies

Mixing studies for the side-port manifolds were limited to single ports only, to the case of $\Delta\rho/\rho_o = 0$, and most runs were made for values of $E > 1$. Results given here are limited to a single Euler number in the range $1.2 < E < 1.3$ for square-edge ports of d/D = 1/8, ¼ and ½. The Euler numbers are still relatively close to the outfall application range, however.

The mixing results are shown in terms of relative mixing expressed as

$(c'-c_o)/(c_e - c_o)$, where c' is the local dye (rhodamine B) concentration of the conduit flow upstream from the manifold, and c_e is the concentration in the ambient fluid. The equation for conservation for the dye is

$$Q_o c_o + q c_e = \int_A uc'dA \tag{20}$$

where u is the local velocity in the downstream conduit and "one-dimensional" dye as well as velocity distributions are assumed in the approach and inlet flows. A comparison with possible uniform mixing to be obtained downstream can be made by considering that if $c' = c_m$, to represent full mixing, Eq. 20 can be re-written:

$$\frac{q}{Q} = \frac{c_m - c_o}{c_e - c_o} \tag{21}$$

The mixing data given are based on measurements of the local tracer (dye) concentration only, and can be considered only an index of the actual fluid flow patterns because no velocity measurements were made. Actual mixing patterns can only be deduced. Because velocities are not known, it is not correct to attempt an integration over the cross section to check on the average dye concentration present for a particular q/Q.

The data in Fig. 25 indicate how dye mixing progresses downstream, with successive concentration patterns measured at X/D = 5.7, 10.0, and 17.5. For all three cases, mixing has become much more uniform at the most downstream station. Predictably, a greater uniformity is achieved with the larger dilution ratios achieved with the larger side ports.

Extension of these data to the case $\rho_e > \rho_o$, as in an outfall case, can only be inferred by comparing the data in Fig. 25 with results for annular ports in Chapter IV. The effect of a more dense inflow liquid on the mixing patterns, and a possible tendency toward stratification downstream, can only be determined by further tests. The part of the study dealing with mixing characteristics of side-port manifolds as given in this report is incomplete, and requires further experimental work.

E. Jet Penetration, Single Ports

Observations made using the hydrogen bubble technique were qualitative only; visual observations were employed mostly as successful photographic

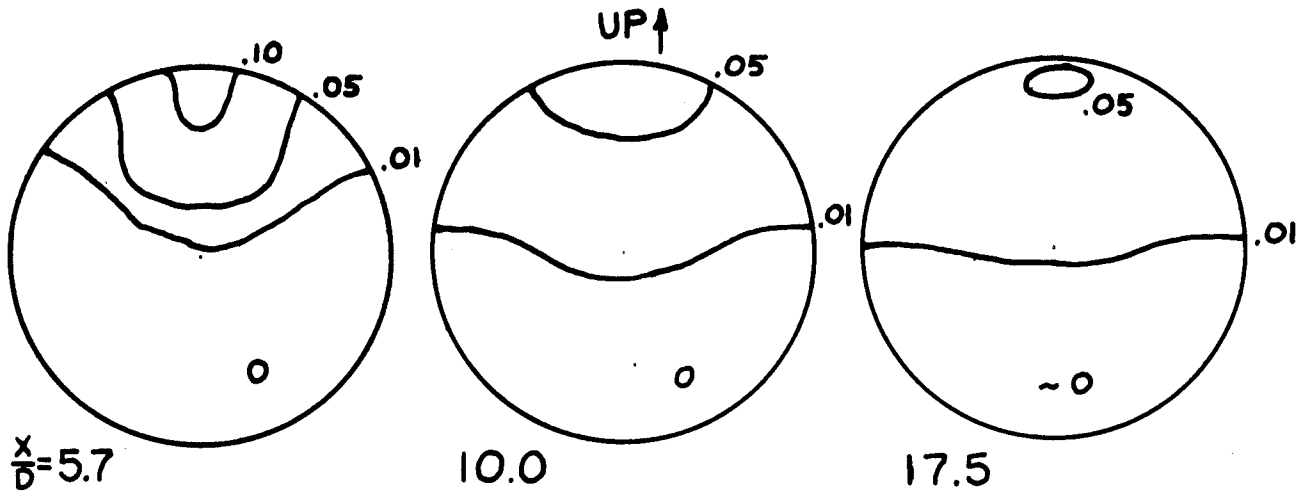

a) $\frac{d}{D}=\frac{1}{8}$, $\frac{q}{Q}=0.014$, $E=1.28$, $\frac{\Delta\rho}{\rho_o}=0$

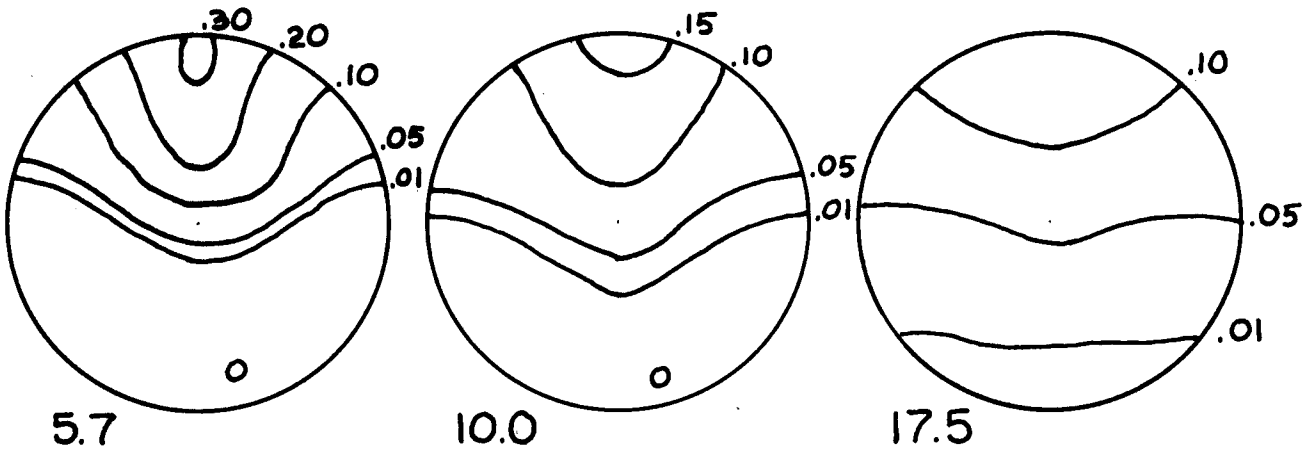

b) $\frac{d}{D}=\frac{1}{4}$, $\frac{q}{Q}=0.054$, $E=1.28$, $\frac{\Delta\rho}{\rho_o}=0$

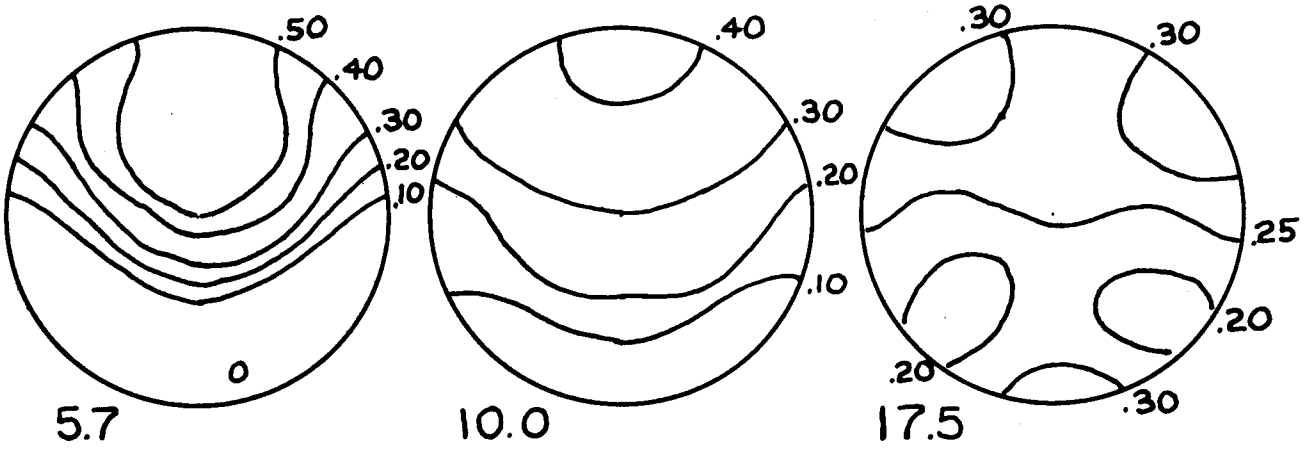

c) $\frac{d}{D}=\frac{1}{2}$, $\frac{q}{Q}=0.19$, $E=1.20$, $\frac{\Delta\rho}{\rho_o}=0$

Figure 25. Mixing Patterns, Side-Port Manifolds

records which could have been used for quantitative data were not achieved. No photographs are included in this report. Initial photographs were taken with an exposure time of 1/750 second on Royal 10 film (ASA 400) in an attempt to 'stop' the bubbles, but because the jet cross section did not become apparent using this short exposure time further efforts involved longer exposure times and faster film. The combination of exposure times as long as 1/5-second with a Polaroid film having an ASA 3,000 rating yielded improvement but did not yield results suitable for printing or for measurement purposes.

Figure 27 shows sketches of observations made with the naked eye, viewing the jet cross section from above. In Fig. 27 (a) the Euler number is much greater than 1.0, and d/D = ¼. The illuminated cross section (that sketched) is at y/D = ½, where y is measured vertically downward from the top of the conduit. A wake developes behind the jet in much the same way as it would if the jet were a solid two-dimensional circular cylinder, and although not evident in the sketch vortices were observed to form in this region and be shed from alternating sides of the jet much as if a solid cylinder were present in the flow. The bubbles shown near the conduit sidewalls indicate that the jet has penetrated to the conduit invert and has followed divided looping paths upward along the conduit walls. The sketch in Fig. 27(b) applies for a case of $\mathbb{E} \approx 1$, and for a lesser penetration y/D = ¼. A wake is still visible, and the upstream face of the jet is flattened as it deflects more rapidly than does the jet of higher relative velocity in Fig. 27(a). There is no evidence of bubbles in the field of vision that have returned along the walls from the conduit invert; such a flow pattern is not present, as observed from following the trajectories of jet inflows by dye injected opposite the port as indicated in Fig. 4.

Other hydrogen bubble observations indicated that as the initially circular jet penetrates into the conduit flow it does tend to assume a horseshoe, or kidney, shape with the open end downstream as it deflects in the main conduit stream. These observations confirm theoretical predictions and experimental deductions of some prior investigators who studied the behavior

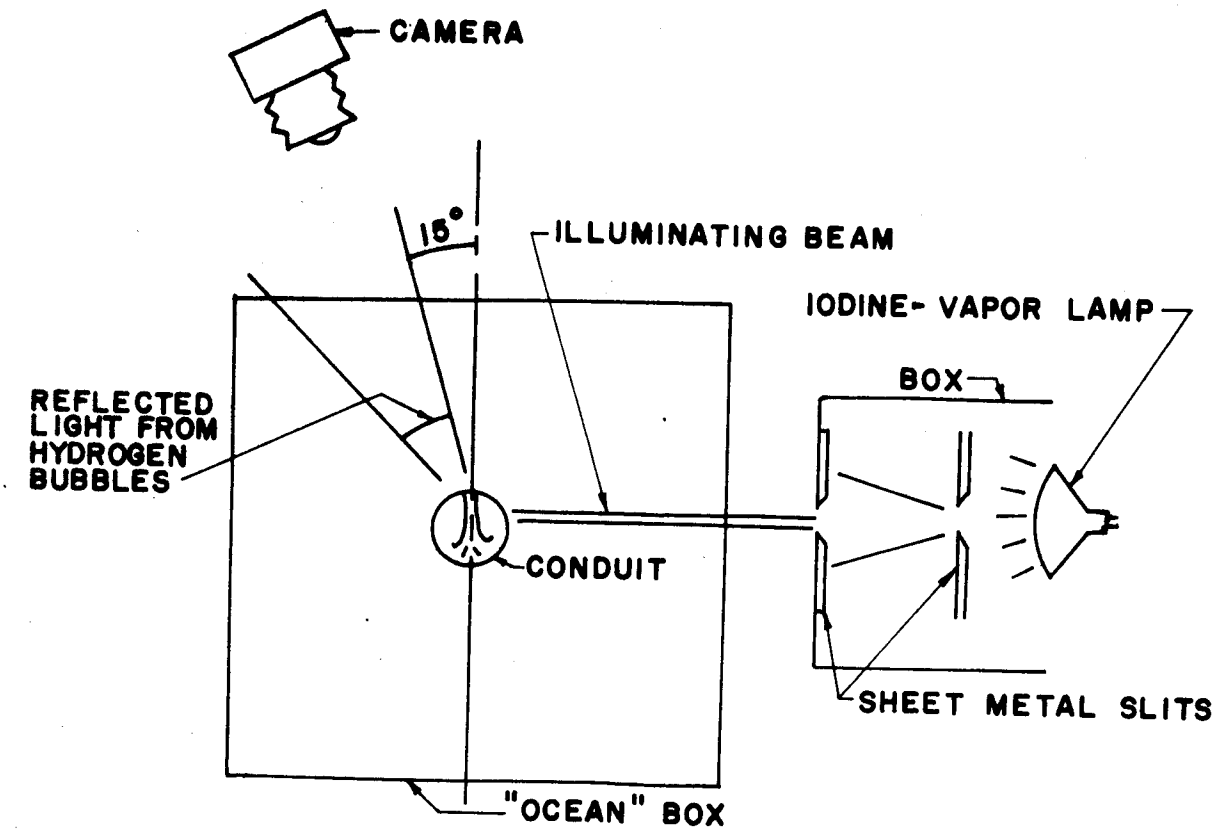

Figure 26. Photographic Set-up for Use with Hydrogen Bubble Technique

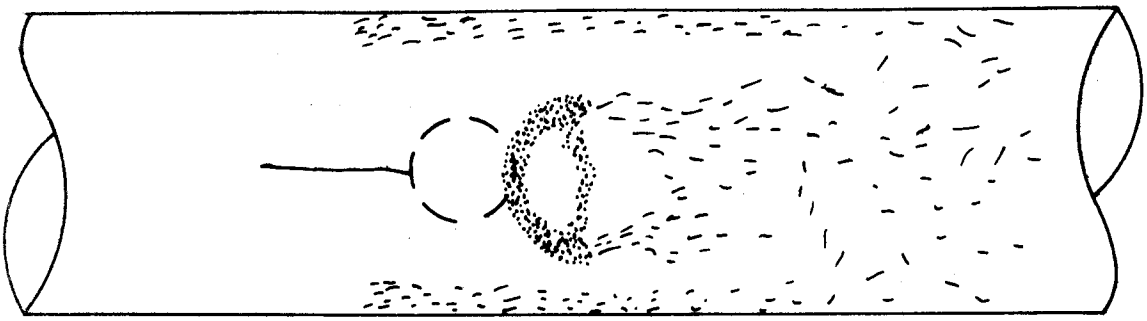

a) $\mathbb{E} \approx 1$, $\frac{Y}{D}=\frac{1}{2}$

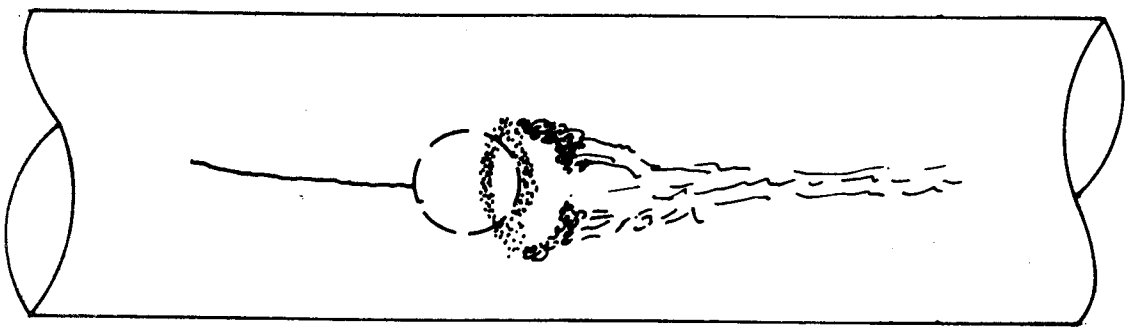

b) $\mathbb{E} \gg 1$, $\frac{Y}{D}=\frac{1}{4}$

Figure 27. Hydrogen Bubble Observations

of a jet penetrating a crossflow but in a much less confined cross section. Typical tests on jets entering somewhat confined crossflows were reported by Gordier (1959) and by Callaghan and Ruggeri (1948); in each case, while relationships were found linking jet and crossflow velocities, the jet itself was relatively small with respect to dimensions of the equivalent conduit flow so that results could not be applied directly to the present study.

Typical jet trajectories for the case $\Delta\rho/\rho_o = 0$ and $d/D = \frac{1}{4}$ are shown in the photographs of Fig. 28. The photographs were made with an exposure time of 1:500 second at f 11; dye traces observed visually tend to smooth out irregularities in the dye trace profile. The trajectories shown are parallel to the jet "axis", and substantiate comments already given. At the lowest $\mathbb{E}$, in the outfall range, the jet is deflected quickly and remains in the upper portion of the conduit before mixing further downstream. The $\mathbb{E}$ = 1.1 case is comparable to that of $\mathbb{E}$ = 1.28 shown in Fig. 25(b). At the highest $\mathbb{E}$ the jet penetrates to the far wall, and a "cloud" is noted which shows that some of the entrained fluid has diffused and moved upstream under the influence of the stagnation point where the penetrating jet impinges on the conduit invert. This action is partially responsible for the hydrogen bubbles observed along the walls in Fig. 27(a).

An empirical relation was developed to describe the jet trajectories. The approach is a quasi one-dimensional one, based on the assumption that all mixing occurs downstream from the port and the conduit fluid is accelerated as it passes around the entering jet. Conditions are summarized in Sketch E. The area through which the conduit flow passes at the plane of

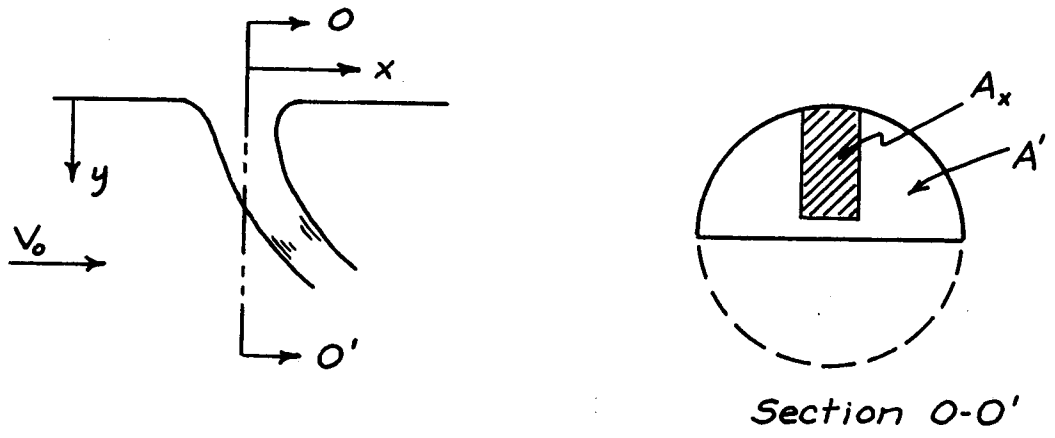

SKETCH E

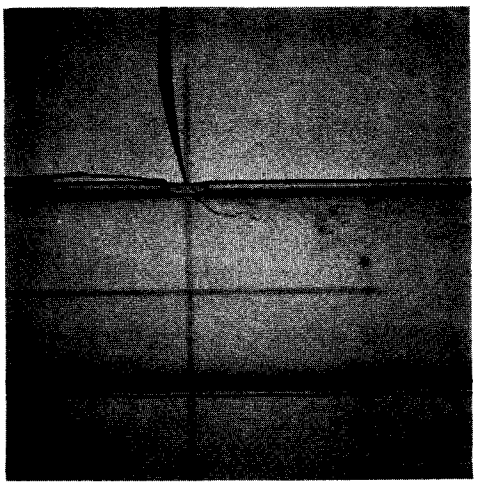

(a) $\mathbb{E} = 0.16$

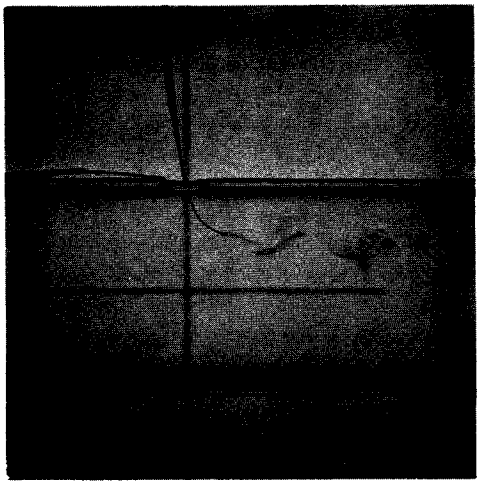

(b) $\mathbb{E} = 1.1$

(c) $\mathbb{E} = 3.8$

(d) $\mathbb{E} = 100+$

Figure 28. Photographs of Jet Trajectories

the port is $A' = \left(\frac{A}{2}\right) - A_x$, in which A_x represents the projected area of the entering jet in the plane O - O'; the average velocity across A' is $V' = (1/2)(Q/A')$, and the effective pressure is p' (see Sketch D).

The Bernoulli equation applied to the conduit flow gives

$$p_o + \frac{\rho_o V_o^2}{2} = p' + \frac{\rho_o V'^2}{2} \tag{22}$$

A new Euler number may be defined, making use of the more "effective" receiving pressure and conduit velocity:

$$\mathbb{E}' = \frac{p_e - p'}{\frac{\rho_o V'^2}{2}} \tag{23}$$

Continuity and Bernoulli equations applied to the conduit flow give

$$p' = p_o + \frac{\rho_o V_o^2}{2}\left[1 - \left(\frac{A}{A'}\right)^2\right] \tag{24}$$

and the revised Euler number becomes

$$\mathbb{E}' = \frac{p_e - p_o - \frac{\rho_o V_o^2}{2}\left[1 - \left(\frac{A}{A'}\right)^2\right]}{\frac{\rho_o V_o^2}{2}\left(\frac{A}{A'}\right)^2} = \frac{\mathbb{E} - 1}{\left(\frac{A}{A'}\right)^2} + 1 \tag{25}$$

Experimental jet center-line trajectories were determined for jets from the square-edge ports of d/D = 1/8, ¼, and ½, and for the rounded-edge port of d/D = ¼. Dimensionless plotting, using the definitions in the above equations along with the geometrical descriptions shown in Sketch E produced the following relationship:

$$\frac{y}{d} = 1.2\left(\mathbb{E}'\right)^{0.4}\left(\frac{x}{d}\right)^{0.4} \tag{26}$$

This empirical equation was obtained for the range $0.4 < \mathbb{E}' < 35$. In form, it has exponents quite similar to those in one of the empirical unconfined flow jet trajectories given by Abramovich (1963).

IV. ANNULAR PORT MANIFOLD

A. Theoretical Analysis

An annular-port suction manifold placed in a simple outfall is shown in Fig. 29. The manifold shown is located in a "venturi" section; it should be noted that because of the manifold geometry pressures at the inlet port may be dropped below those of the ambient fluid without resorting to a decrease in main conduit diameter. This point will be amplified later. Pertinent variables are shown in the definition sketch, Fig. 30. As in Fig. 13, conventional frictional losses are neglected. The situation shown in the figure does pertain to outfall applications because the total head line for flow along the conduit remains above the level of the ambient liquid. The treatment to follow is restricted to the case of $\Delta\rho/\rho_o = 0$. No dimensional analysis considerations are listed; effects of viscosity, ignored in the simple theoretical treatment, are considered later in the discussion of experimental results.

Axial symmetry is assumed initially (in line with Fig. 30) and the ambient fluid which completely surrounds the horizontal conduit is assumed to be at rest. The annular port has an area, a, and the port-nozzle configuration is so shaped that the dilution flow, q, enters the mixing chamber with a velocity, v, directed parallel to the conduit axis. Likewise, the nozzle of exit cross-sectional area A_i is shaped so that the initial conduit flow Q_o enters the mixing chamber with a velocity V_i which also is parallel to the conduit axis. The nozzle wall is assumed to have zero thickness. The parallel streamlines provide an hydrostatic pressure distribution over the mixing chamber entrance, with p_i being the average pressure over the entire area, A. It is assumed that the two coaxial streams mix fully within the mixing chamber; the downstream end of the mixing chamber is sufficiently far from the nozzle that the combined flow Q has an average velocity, V, and an average pressure, p. The analysis assumes then, that one-dimensional conditions exist at mixing chamber inlet and outlet. Boundary shears are neglected. The control volume selected is coincident with the mixing chamber;

the one-dimensional approach is indicated in Sketch F. Again, for application to real flow cases the head differential terms yielded by the

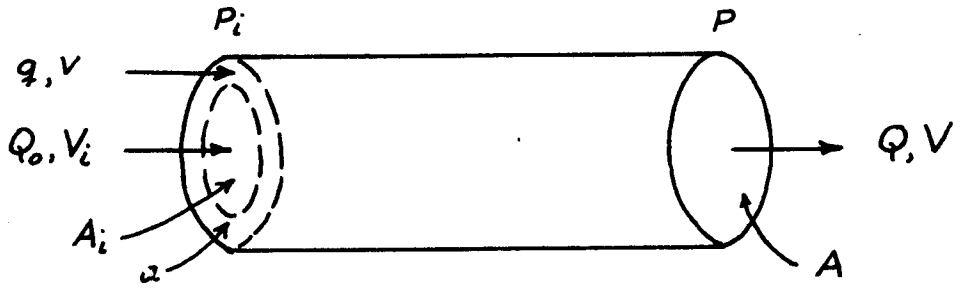

SKETCH F

following analysis would be superposed on the frictional losses in that portion of the conduit which is the mixing chamber. It is further assumed in the idealized analysis below that head losses through both the port and through the nozzle are zero. Even when $(a + A_i) < A$, as in the partially closed annuli listed in Table III, the one-dimensional analysis is still valid so long as the streamlines entering the mixing chamber can be assumed parallel and correspondingly the pressure distribution taken as hydrostatic over the entrance plane.

The total head line and the piezometric head line are shown in Fig. 30 for both q and Q_o as well as for the combined downstream discharge Q. As noted in Fig. 30, H_p is the excess total head of Q_o above the total head of the ambient fluid, H_g is the head gain of the entrained dilution flow q, H_d is the excess head above that of the ambient fluid for the combined flow Q as it leaves the mixing chamber, H_L is again the head loss experienced by the conduit flow, and Δh is the pressure head drop (defined consistently with the side port case across the mixing chamber.

Steady flow continuity, momentum, and energy equations can be written using the simplifications noted above.

Continuity:

$$Q_o + q = Q \tag{27}$$

$$A_i V_i + av = AV \tag{28}$$

Momentum:

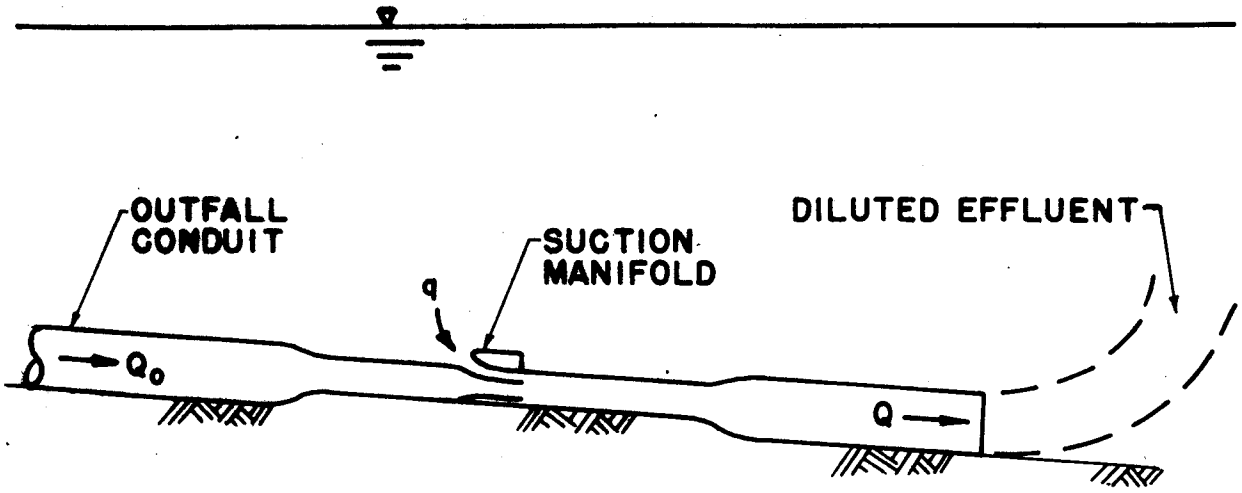

Figure 29. Annular-Port Manifold in Outfall

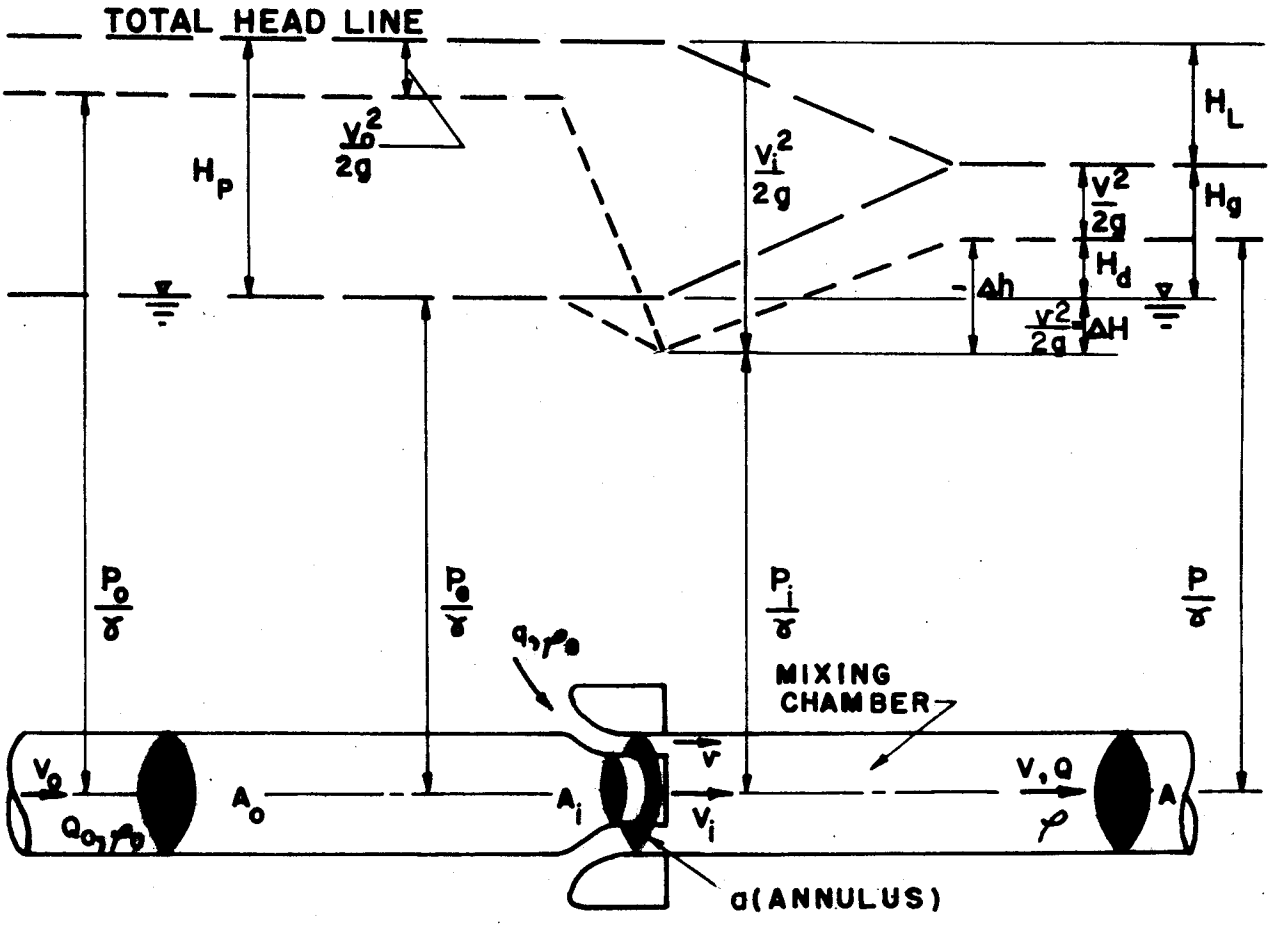

Figure 30. Definition Sketch, Annular-Port Manifold

$$(p_i - p)\,A = Q\rho V - (Q_o \rho V_i + q\rho v) \tag{29}$$

Energy, applied to the conduit flow, with head losses occurring in the mixing chamber only:

$$\frac{V_o^2}{2g} + \frac{p_o}{\gamma} = \frac{V_i^2}{2g} + \frac{p_i}{\gamma} = \frac{V^2}{2g} + \frac{p}{\gamma} + H_L \tag{30}$$

Energy, applied to the entrained flow and assuming no loss through the port:

$$\frac{p_e}{\gamma} = \frac{v^2}{2g} + \frac{p_i}{\gamma} = \frac{V^2}{2g} + \frac{p}{\gamma} - H_g \tag{31}$$

An entrainment coefficient may be defined for the annular port. The effective pressure head differential across the port is defined first as

$$\Delta H = \frac{p_e}{\gamma} - \frac{p_i}{\gamma} \tag{32}$$

and is seen to depend in part upon the geometry through the relation of A_i and A. The entrainment coefficient again is defined by

$$C_e = \frac{q}{a\sqrt{2g\Delta H}} \tag{33}$$

and in accordance with the assumptions made $C_e = 1.0$.

Again, a port Euler number is defined as

$$\mathbb{E} = \frac{\left(\frac{p_e - p_i}{\gamma}\right)}{\left(\frac{V_i^2}{2g}\right)} = \frac{\Delta H}{\left(\frac{V_i^2}{2g}\right)} \tag{34}$$

and for the assumed conditions is the square of the ratio v/V_i. Again the ideal upper bound for outfall operation is $\mathbb{E} = 1.0$, at which limiting condition the total heads of both the conduit and dilutant flows would be equal and for which no downstream exit loss from the manifold could be

possible. As with the side port manifold, a value of $E = 1.0$ could never be realized in a practical installation, but has been used as the upper limit in the following results.

Equations 27-34 may be solved simultaneously. Dilution ratios q/Q are related to the manifold geometry which may be characterized by the area ratio a/A in order to allow for non axi-symmetric arrangements. Head drops can be related to area ratios and to q/Q; results are normalized through division by $V^2/2g$, again in recognition that head loss calculations for an outfall would have to begin at the outlet end and proceed upstream toward the manifold. The resulting equations are:

$$\frac{q}{Q} = \frac{1}{1 + \frac{A_i}{a E^{\frac{1}{2}}}} \tag{35}$$

$$\frac{\Delta h}{\left(\frac{V^2}{2g}\right)} = 2\left[1 - \left(\frac{A}{a}\right)\left(\frac{q}{Q}\right)^2 - \frac{A}{A_i}\left(1 - \frac{q}{Q}\right)^2\right] \tag{36}$$

$$\frac{H_L}{\left(\frac{V^2}{2g}\right)} = 1 - 2\left(\frac{A}{a}\right)\left(\frac{q}{Q}\right)^2 + \left(1 - \frac{q}{Q}\right)^2\left[\left(\frac{A}{A_i}\right)^2 - 2\frac{A}{A_i}\right] \tag{37}$$

The other head change terms (H_d, H_g, and H_p) can also be expressed in comparable dimensionless fashion by noting their relationships to Δh, H_L and ΔH. As seen in Fig. 30:

$$H_d = (-\Delta h) - \Delta H \tag{38}$$

$$H_g = \frac{V^2}{2g} + (-\Delta h) - \Delta H \tag{39}$$

$$H_p = H_L + H_g \tag{40}$$

Dimensionless forms of Eqs. 38-40, along with Eq. 37, may be plotted on one diagram to illustrate the idealized behavior of an annular port manifold

when the upper limit of operation ($\mathbb{E}$ = 1.0) is approached. Results are plotted in Figs. 31-35. Figures 31-33 apply to the case of a fully open annulus ($a + A_i = A$) for three a/A ratios of ¼, 1/3, and ½, respectively. Figures 34-35 are for partially closed annular ports of a/A = ¼, $(a + A_i)/A$ = 3/4 and of a/A = 1/3, $(a + A_i)/A$ = 5/6, respectively. The plots in Figs. 33-35 are all for the case A_i/A = ½, the nominal case tested experimentally (Table III).

In Figs. 31-33 $H_g = H_L = 0$ at the q/Q ratio corresponding to the case $\mathbb{E}$ = 1.0. For these fully open annuli, the limiting q/Q = a/A, as seen by substitution in Eq. 35. For the partially closed annuli, the upper limit of outfall operation is reached when $H_g = 0$. With reference to Fig. 30, writing the energy equation as

$$\frac{P_i}{\gamma} + \frac{V_i^2}{2g} = \frac{P_i}{\gamma} + \Delta H + H_g + H_L \tag{41}$$

and letting $H_g = 0$ results in the equation

$$\mathbb{E} = 1 - \frac{H_L}{\left(\frac{V_i^2}{2g}\right)} \tag{42}$$

As evident from Figs. 34-35, $H_L \neq (H_g = 0)$ for this condition, and as a consequence the limiting situation when such a manifold can be used in an outfall occurs for $\mathbb{E} < 1.0$.

When H_d is negative an expanding diffuser is necessary downstream from the manifold in order to raise the pressure level at the outlet end of the outfall above that of the receiving water so that the outfall actually can discharge there. When H_d is positive, a diffuser is not necessary. (Again, frictional losses in the conduit downstream from the manifold nozzle have been neglected.) The limiting q/Q values for which expanding diffusers are needed are shown in Figs. 31-35, and are listed in Table V.

Table V

Dilution Ratio at which Diffuser is Necessary

a/A	A_i/A	$(a+A_i)/A$	Minimum q/Q
¼	3/4	1	0.1125
1/3	2/3	1	0.165
½	½	1	0.290
¼	½	3/4	0.225
1/3	½	5/6	0.258

The values given by Eqs. 35-37 are plotted in Figs. 36-41. Figures 36, 37 and 41 are for a range of a/A ratios for fully open annular ports so that $(a + A_i)/A = 1.0$ in all cases. Figures 38-40 apply for the case $A_i/A = ½$, but for various partially closed annular ports of a/A ranging from 1/8 to ½. In Figs. 38-40 the dashed lines indicate when limits of outfall use have been exceeded. Table VI lists the maximum dilution ratios possible with the various configurations.

Table VI

Maximum Dilution Ratios for Outfall Application

a/A	A_i/A	$(a+A_i)/A$	Maximum q/Q
1/8	7/8	1	0.125 (=a/A)
1/5	4/5	1	0.200 "
¼	3/4	1	0.250 "
1/3	2/3	1	0.333 "
½	½	1	0.500 "
2/3	1/3	1	0.667 "
1/8	½	5/8	0.186
1/5	½	7/10	0.273
¼	½	3/4	0.323
1/3	½	5/6	0.395

B. Experimental Results: Hydraulic Characteristics of Annular - Port Manifolds

The three annular-port configurations tested were discussed in Section C of Chapter II; specific dimensions are listed in Table III. All experiments used to determine the external hydraulic characteristics of the manifolds were run at $\Delta\rho/\rho_o = 0$.

The entrainment coefficient C_e serves as a measure of the efficiency of the manifold as an entrainment device. The annular port was shaped so as to minimize separation and development of boundary layers within the dilutant, in addition to insuring that the dilutant entered the mixing chamber parallel to the conduit axis. It is expected that $C_e < 1.0$ in a set-up such as that tested, primarily because of decrease in effective annulus discharge area due to boundary layer development.

Experimental values of C_e are plotted in Fig. 42, where the port Reynolds number is defined as

$$\mathbb{R}_a = \frac{vb\rho_e}{\mu_e} = \frac{(q/a)b\rho_e}{\mu_e}$$

where b is the gap width of the annular port at the mixing chamber entrance. Experimental errors are greatest for $\mathbb{R}_a < 3{,}000$, for which low flow runs accuracy of measuring the small manometer differentials was poor. The values of C_e tend toward asymptotic values as $\mathbb{R}_a$ increases. The asymptotic value for the axi-symmetric case agrees fairly well with a C_e estimated on the basis of a displacement thickness, calculated using equations for laminar boundary layers on flat plates, for the range of average velocities 1.3 fps $< v <$ 3.5 fps used in the tests. A prototype-scale manifold would be much larger than the device tested in the laboratory; with the larger scale, the effective reduction in the annulus discharge area due to the presumably turbulent boundary would be relatively smaller compared to the annular area itself and a higher asymptotic value of C_e than the experimental 0.93 could be realized through proper shaping. The difference in C_e values for the two partially-closed annular ports could in part be due to discrepancies in the shaping of the plug used for the $a/A = 0.247$ case. It is concluded that partial closure has little effect upon C_e so long as the port guide walls are

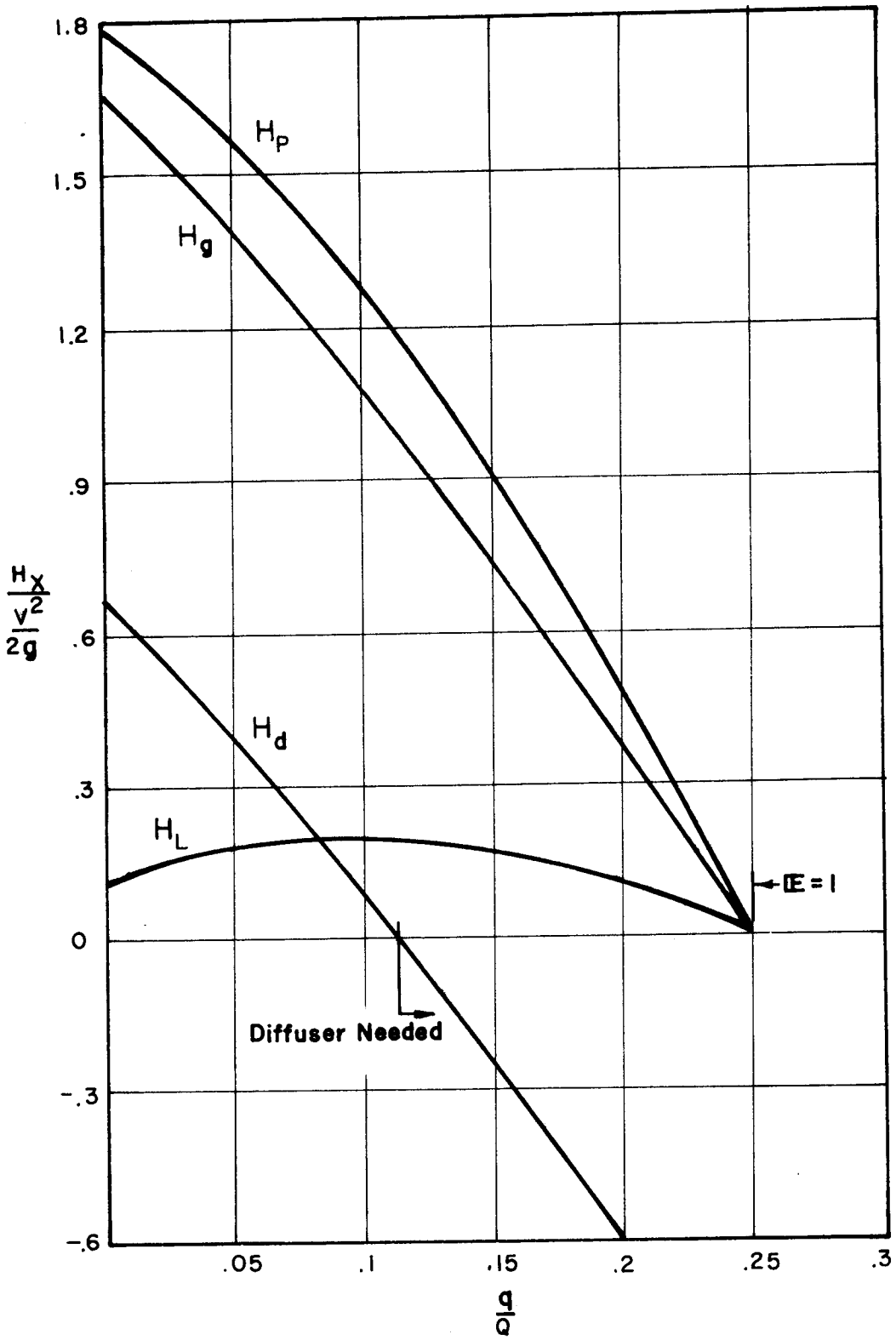

Figure 31. Annular-Port Manifold Head Losses (Theory), $a/A = \frac{1}{4}$, $(a/A) + (A_i/A) = 1$

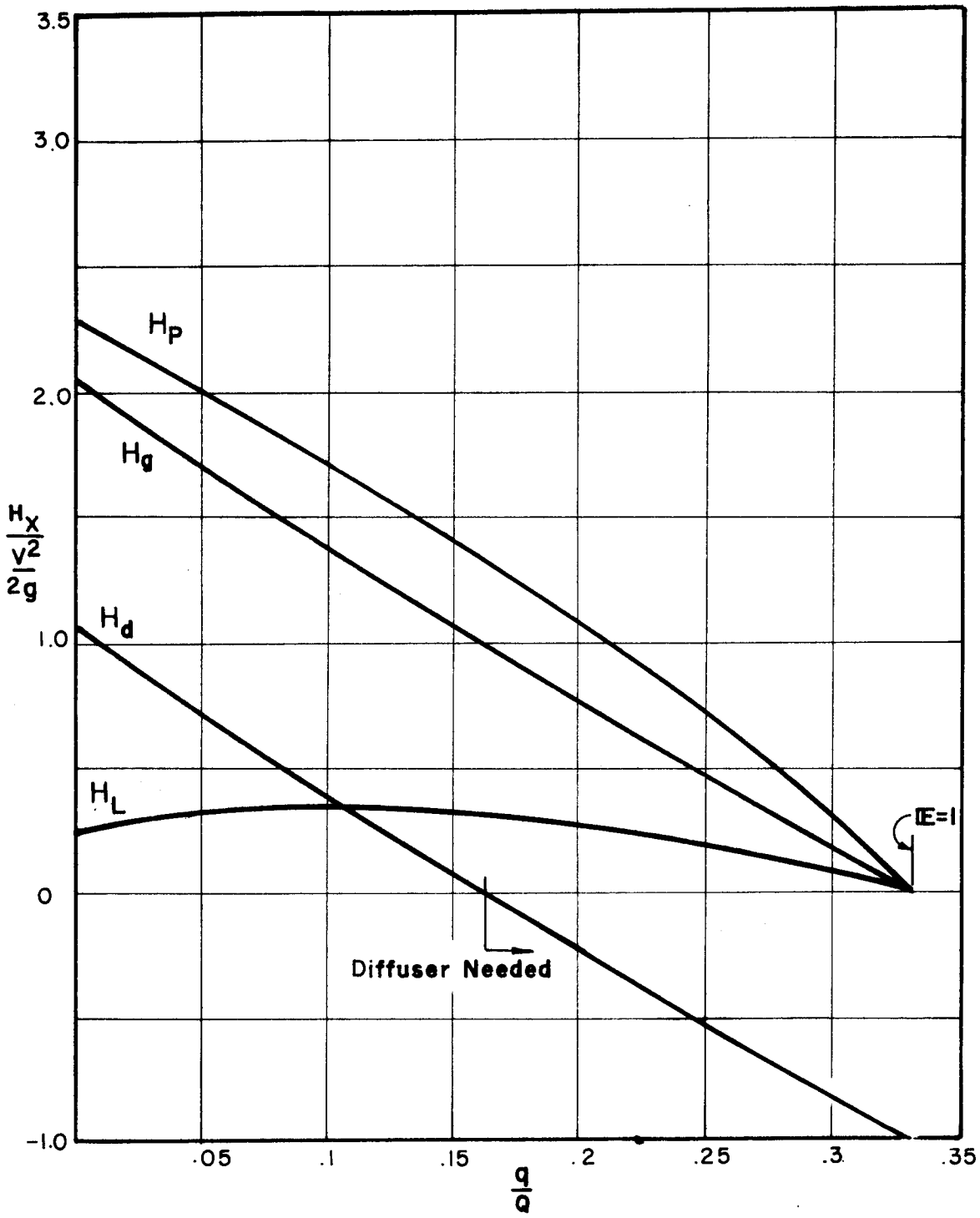

Figure 32. Annular-Port Manifold Head Losses (Theory), $a/A = 1/3$, $(a/A) + (A_i/A) = 1$

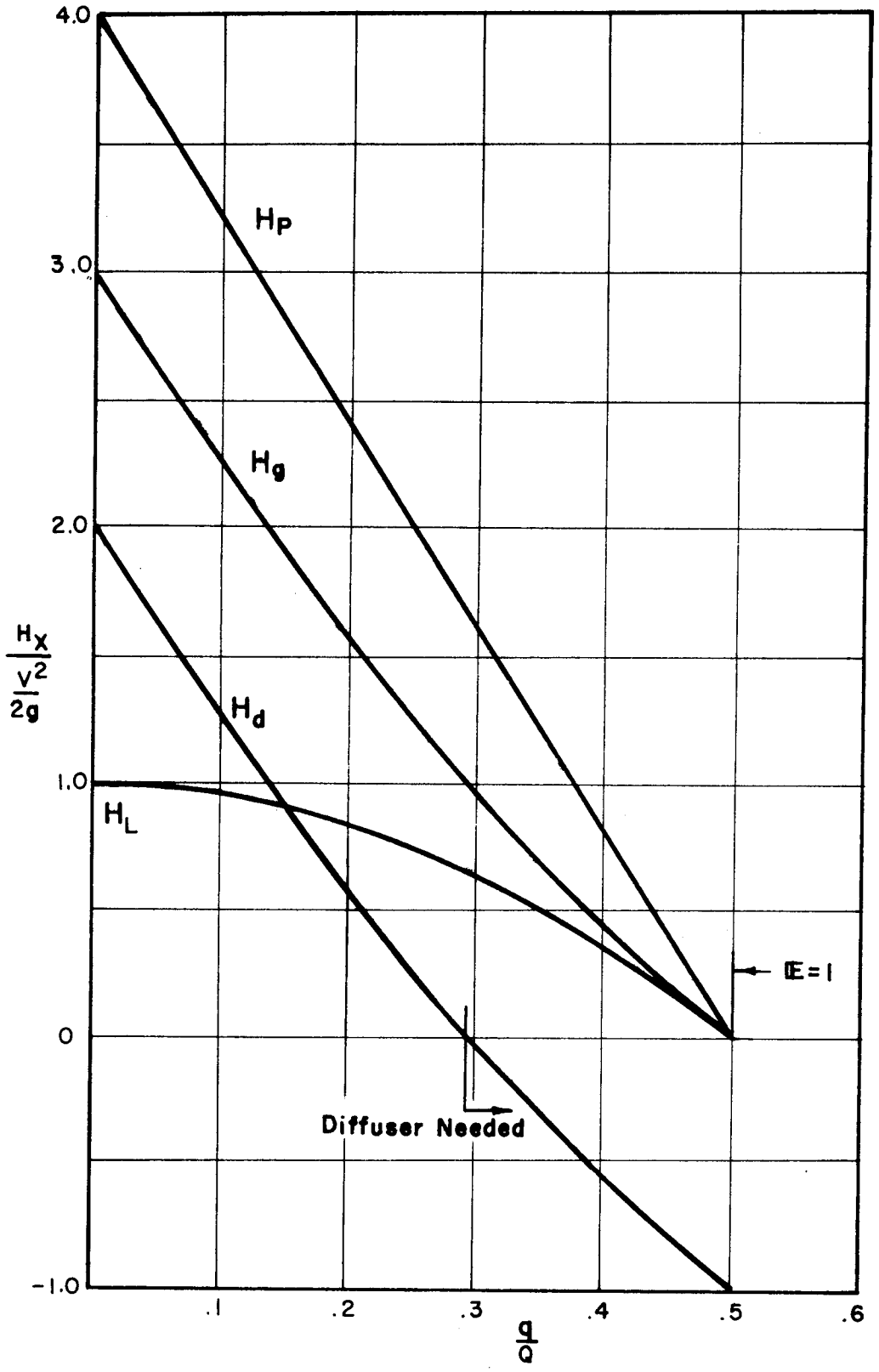

Figure 33. Annular-Port Manifold Head Losses (Theory), $a/A = \frac{1}{2}$, $(a/A) + (A_i/A) = 1$

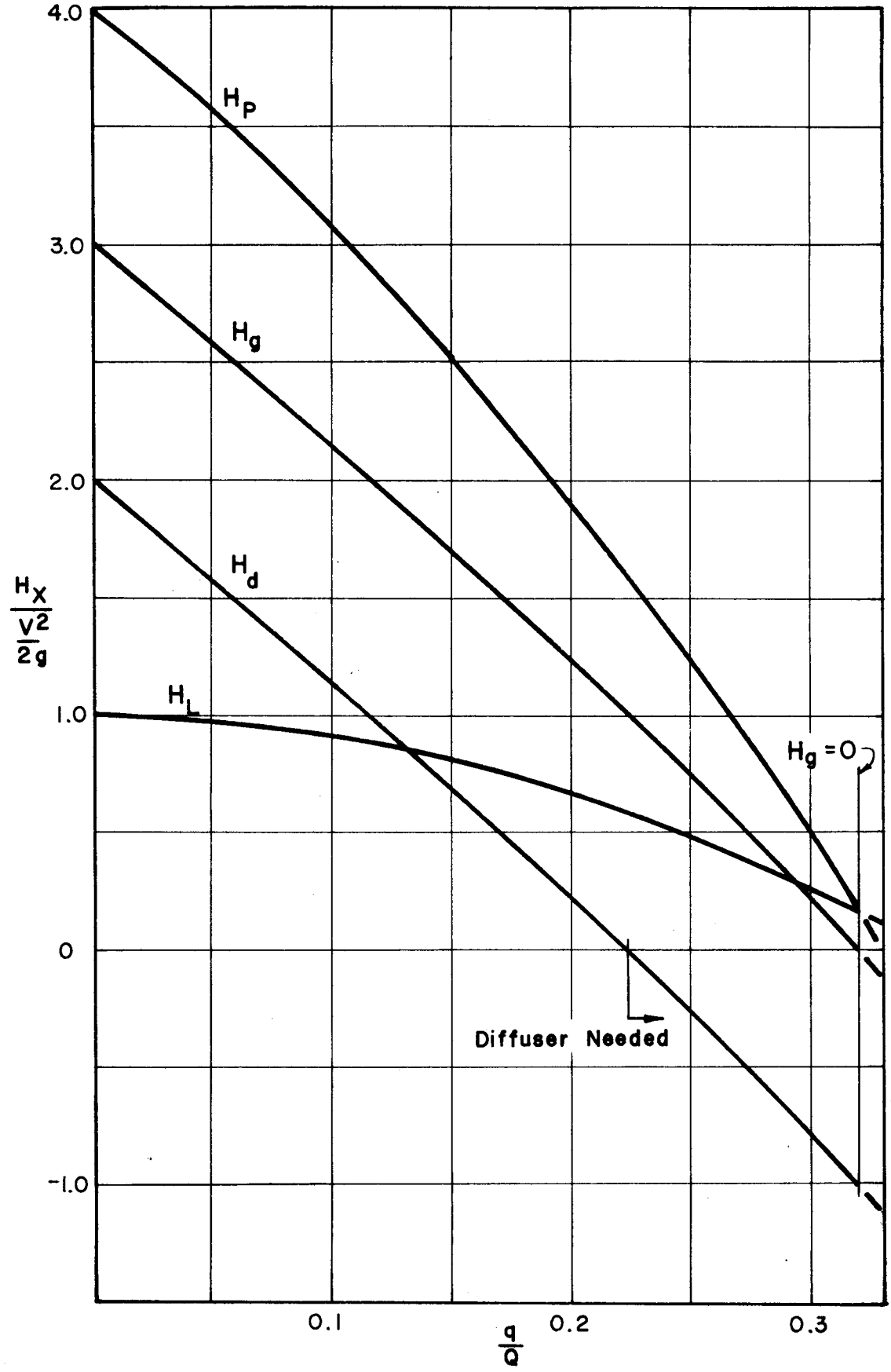

Figure 34. Annular-Port Manifold Head Losses (Theory), $a/A = \frac{1}{4}$, $(a/A) + (A_i/A) = 3/4$

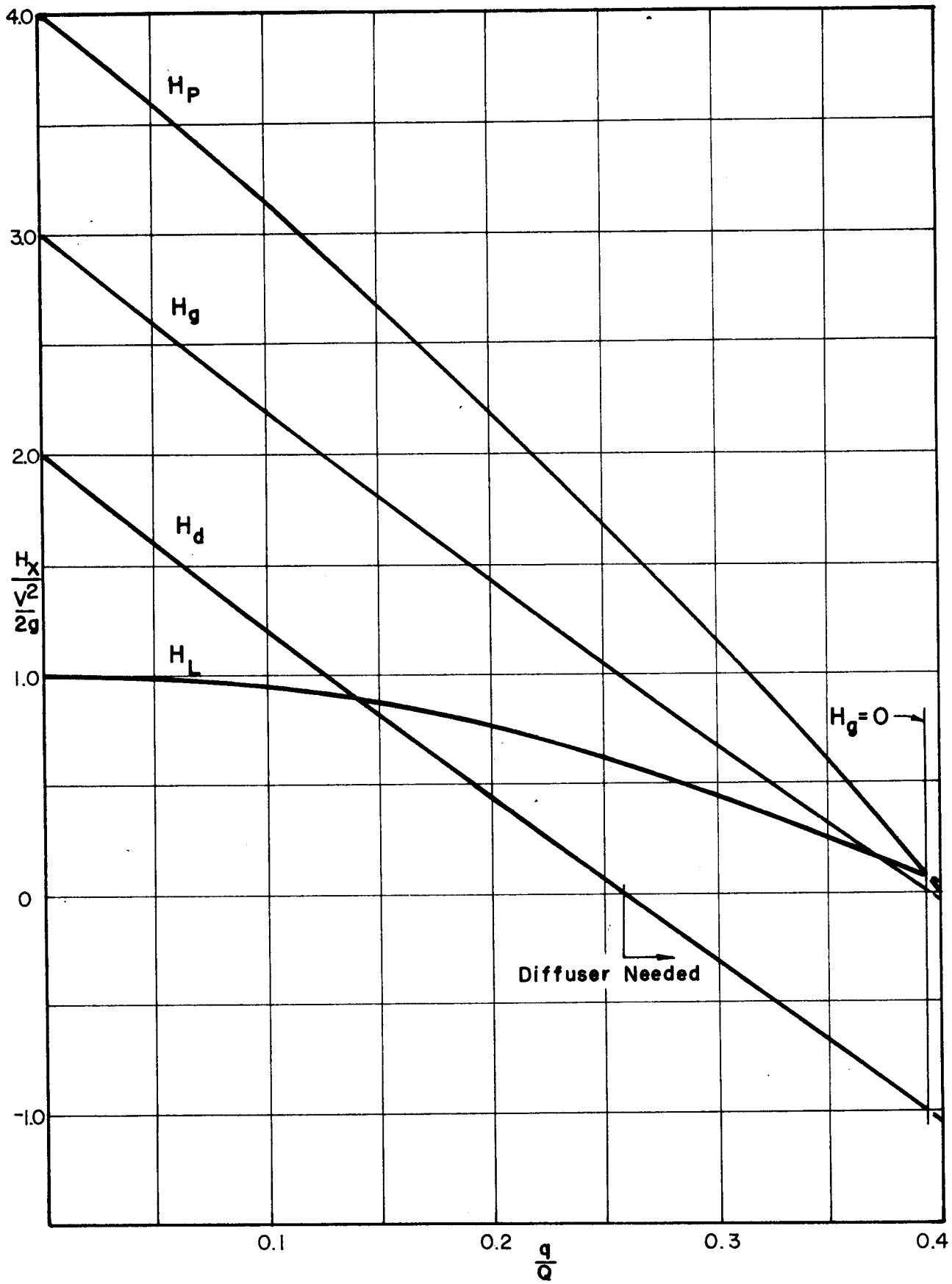

Figure 35. Annular-Port Manifold Head Losses (Theory), $a/A = 1/3$, $(a/A) + (A_i/A) = 5/6$

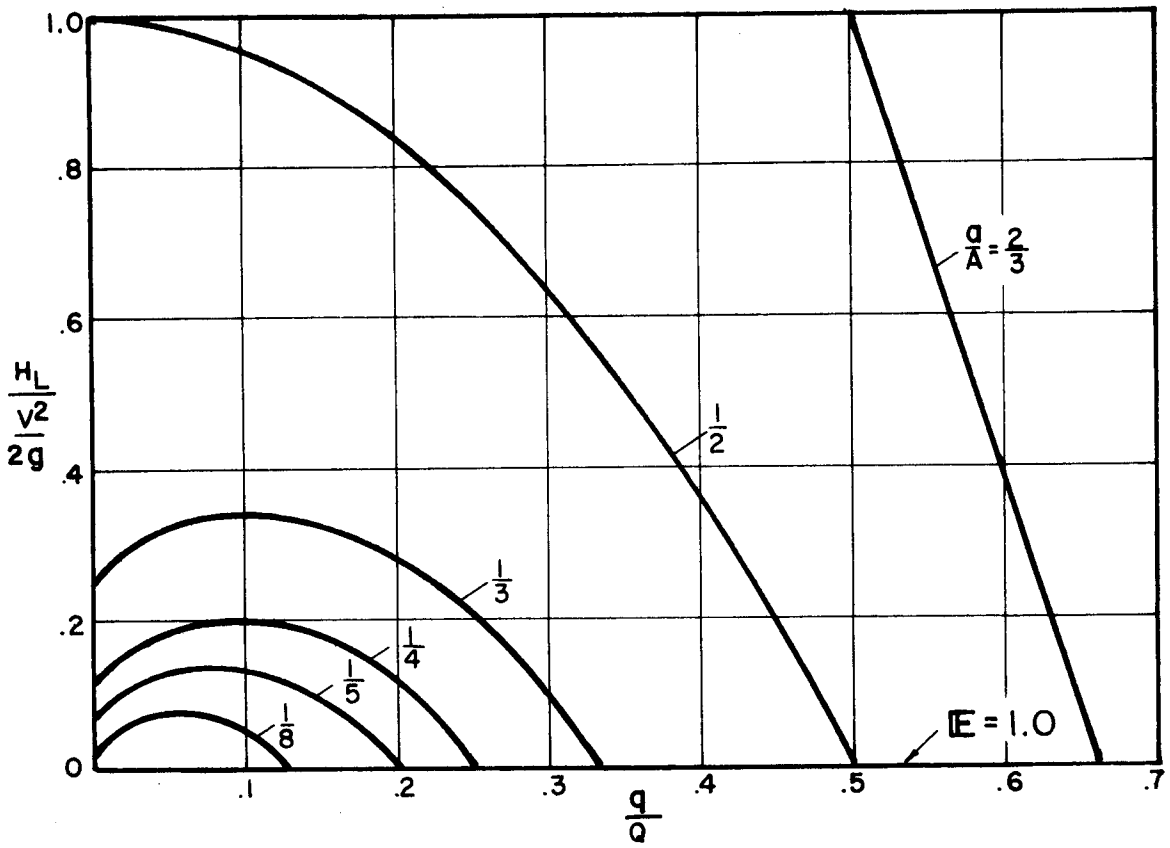

Figure 36. Head Loss (Theory), $(a/A) + (A_i/A) = 1$

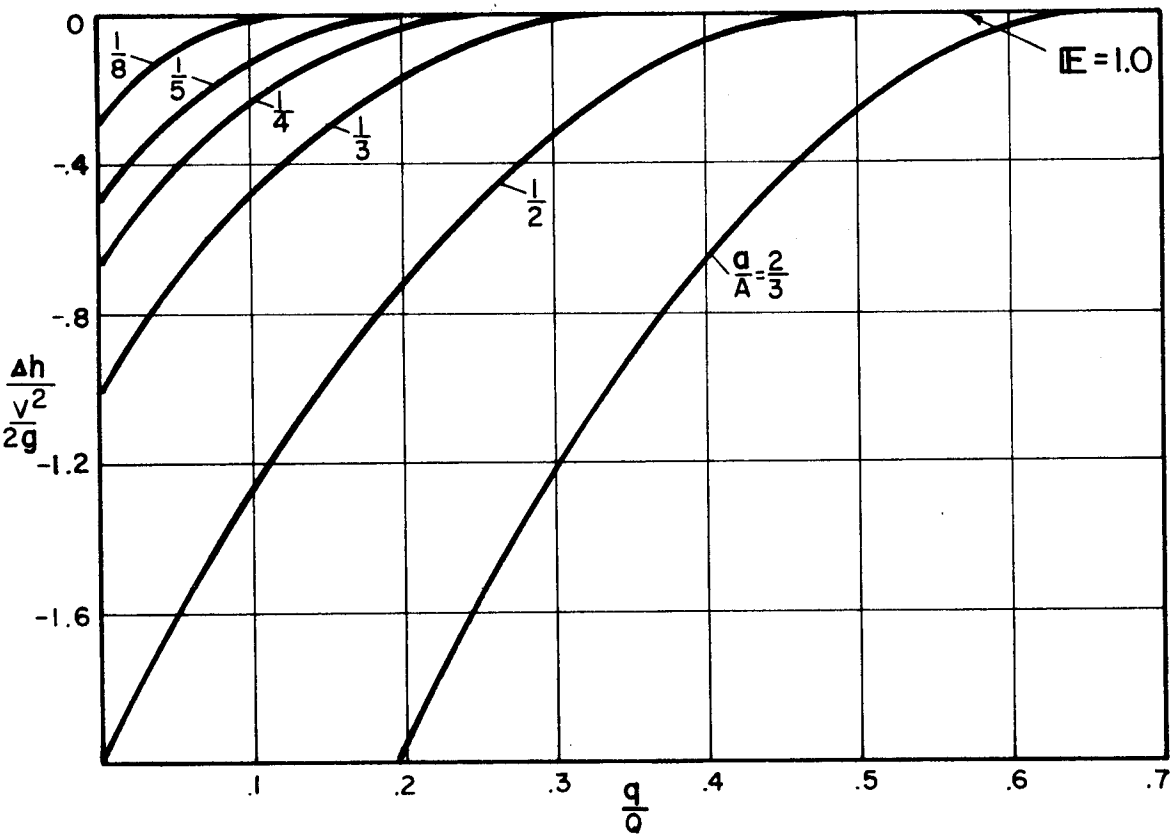

Figure 37. Pressure Head Drop across Mixing Chamber (Theory), $(a/A) + (A_i/A) = 1$

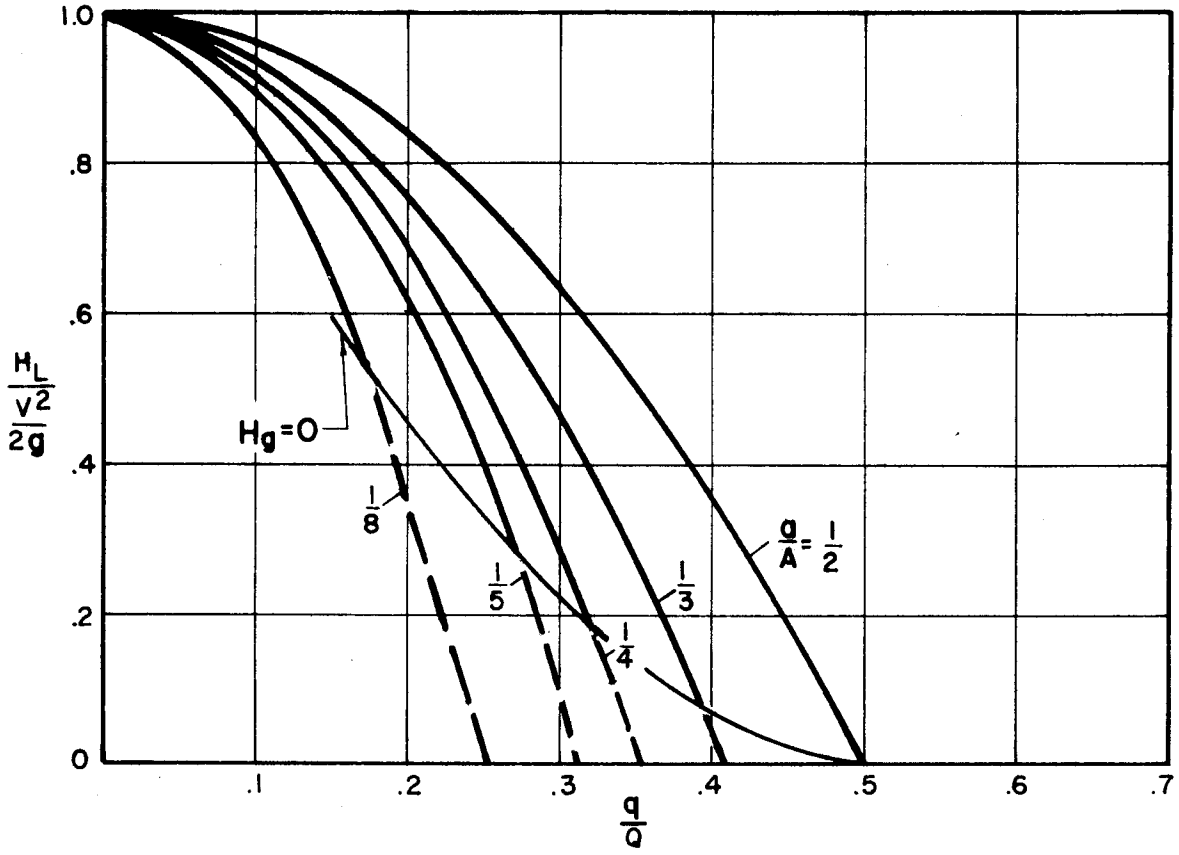

Figure 38. Head Loss (Theory), $(a/A) + (A_i/A) < 1$

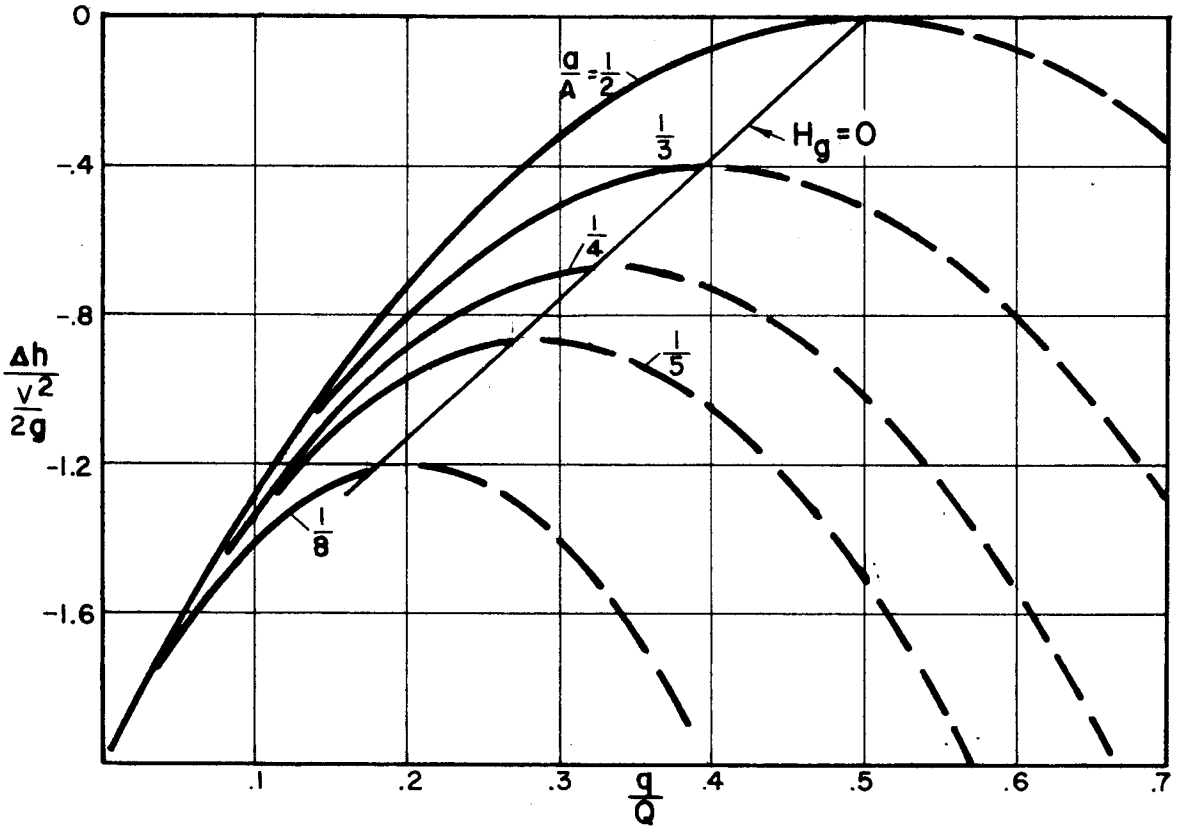

Figure 39. Pressure Head Drop across Mixing Chamber (Theory), $(a/A) + (A_i/A) < 1$

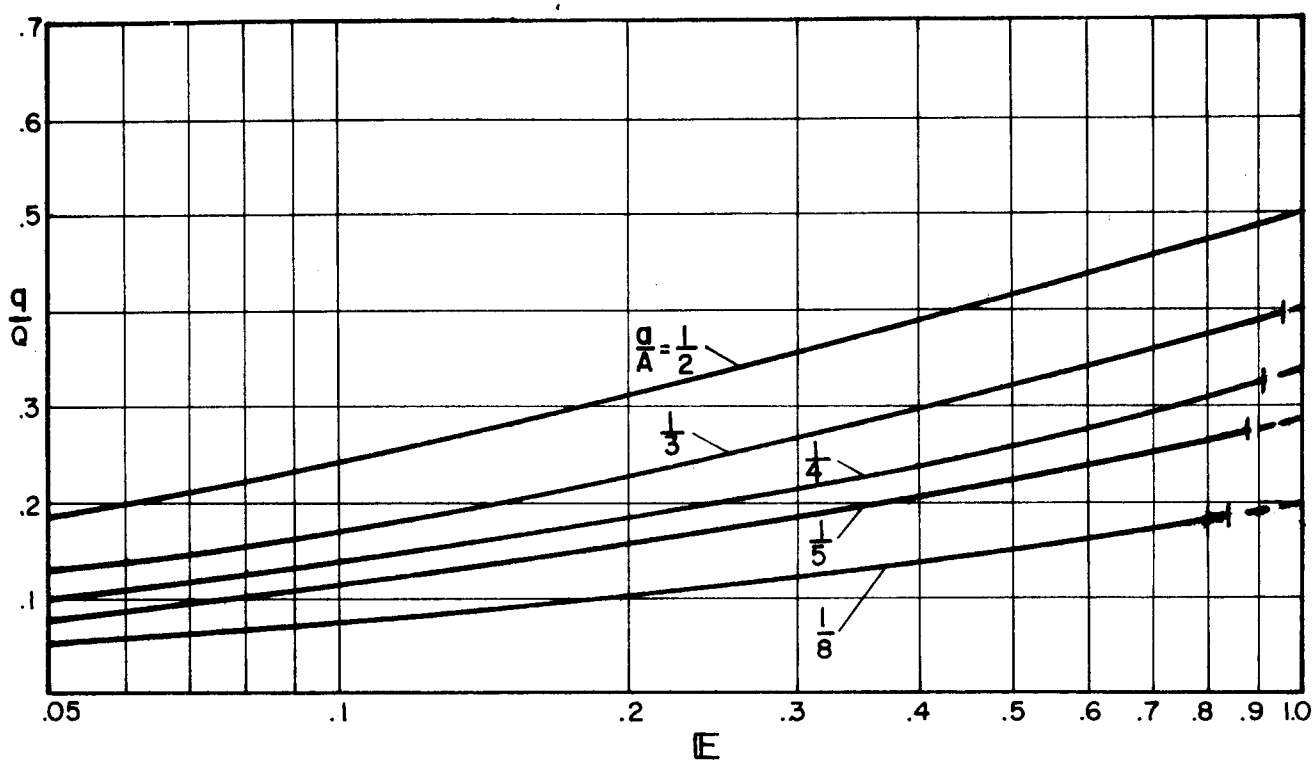

Figure 40. Dilution Ratio vs. Euler Number (Theory), Various Area Ratios, $(a/A) + (A_i/A) < 1$

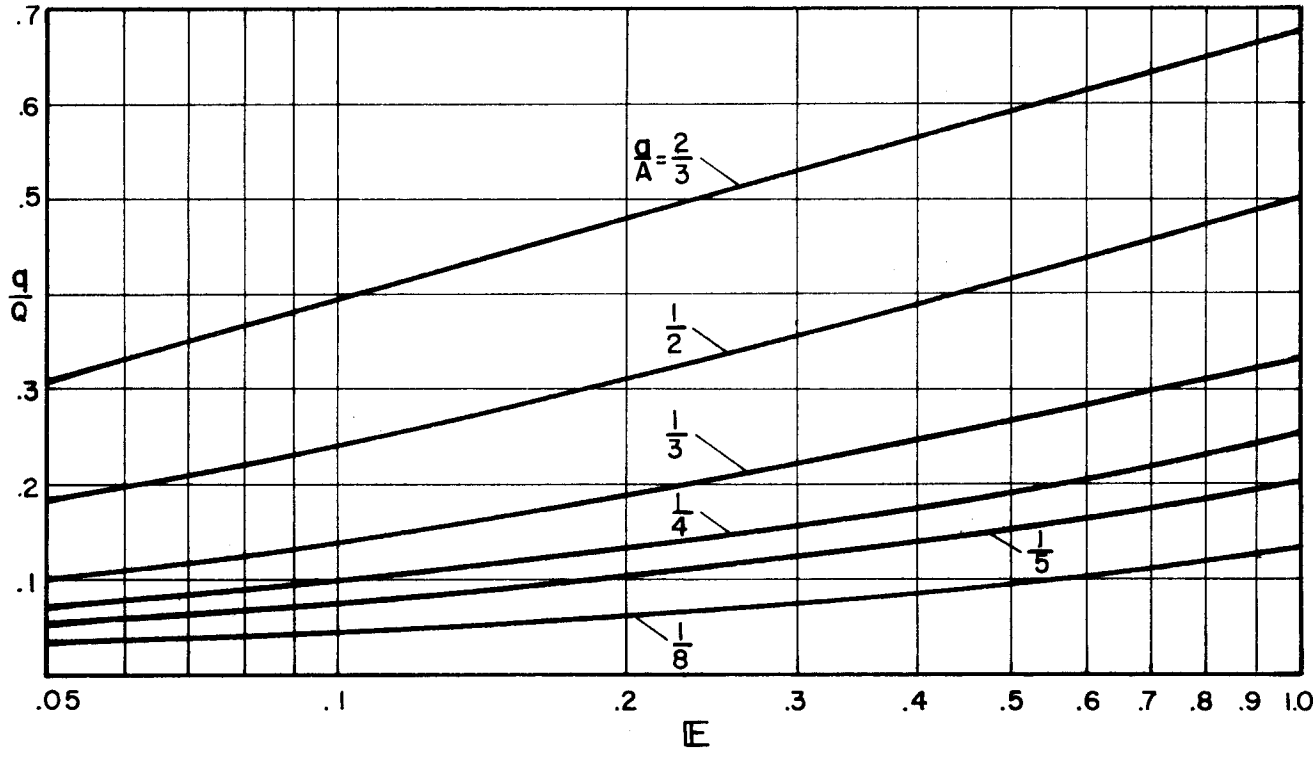

Figure 41. Dilution Ratio vs. Euler Number (Theory), Various Area Ratios, $(a/A) + (A_i/A) = 1$

properly shaped.

Experimental q/Q, H_L, and Δh data are presented in Figs. 43-45 for the three ports tested; in each figure the curves representing the simple one-dimensional theory are based upon the actual constructed area ratios being substituted in Eqs. 35-37. The limiting q/Q in an outfall situation is shown for each configuration. Head drop data agree quite well with predicted values. Dilution ratios, because $C_e < 1.0$, are lower than those predicted assuming ideal flow conditions through the annulus. Again, much of the deviation in the experimental data is attributed to the lack of accuracy possible in measuring the low flows used in many of the runs.

The direct measurement of p_i obviated the necessity for considering the head losses occurring in the nozzle. Pressure measurements along the upstream conduit, coupled with p_i determinations, gave results indicating the loss through the nozzle to be $0.14\ (V_i^2/2g)$. A larger and more carefully designed manifold would have smaller nozzle losses. At any rate, the nozzle losses must be considered in evaluating a prototype installation.

C. Mixing Studies

The simplified hydraulic analysis presented in Section A assumes complete mixing in the mixing chamber. Because the concept of using the suction manifold as a predilution device depends upon this premise, the actual efficiency of the material mixing process must be examined. Two questions of particular interest and concern from the standpoints of design and possible operation are: (1) what may be interpreted as the required or effective length of the mixing chamber; (2) what degree of uniformity of mixing actually is achieved at the downstream end of the mixing chamber? These questions become more important when appreciable density differences exist between the initial conduit flow and the ambient fluid. This section concerns the mixing process and experimental data obtained.

The process has two phases in the manifold. Initially, downstream from the nozzle the turbulence engendered by the shear flow between the two coaxial jets tends to mix the two streams and the denser fluid entering at the top of the mixing chamber tends to move downward into the lighter central core fluid to expedite mixing. Further downstream, however, the conduit flow

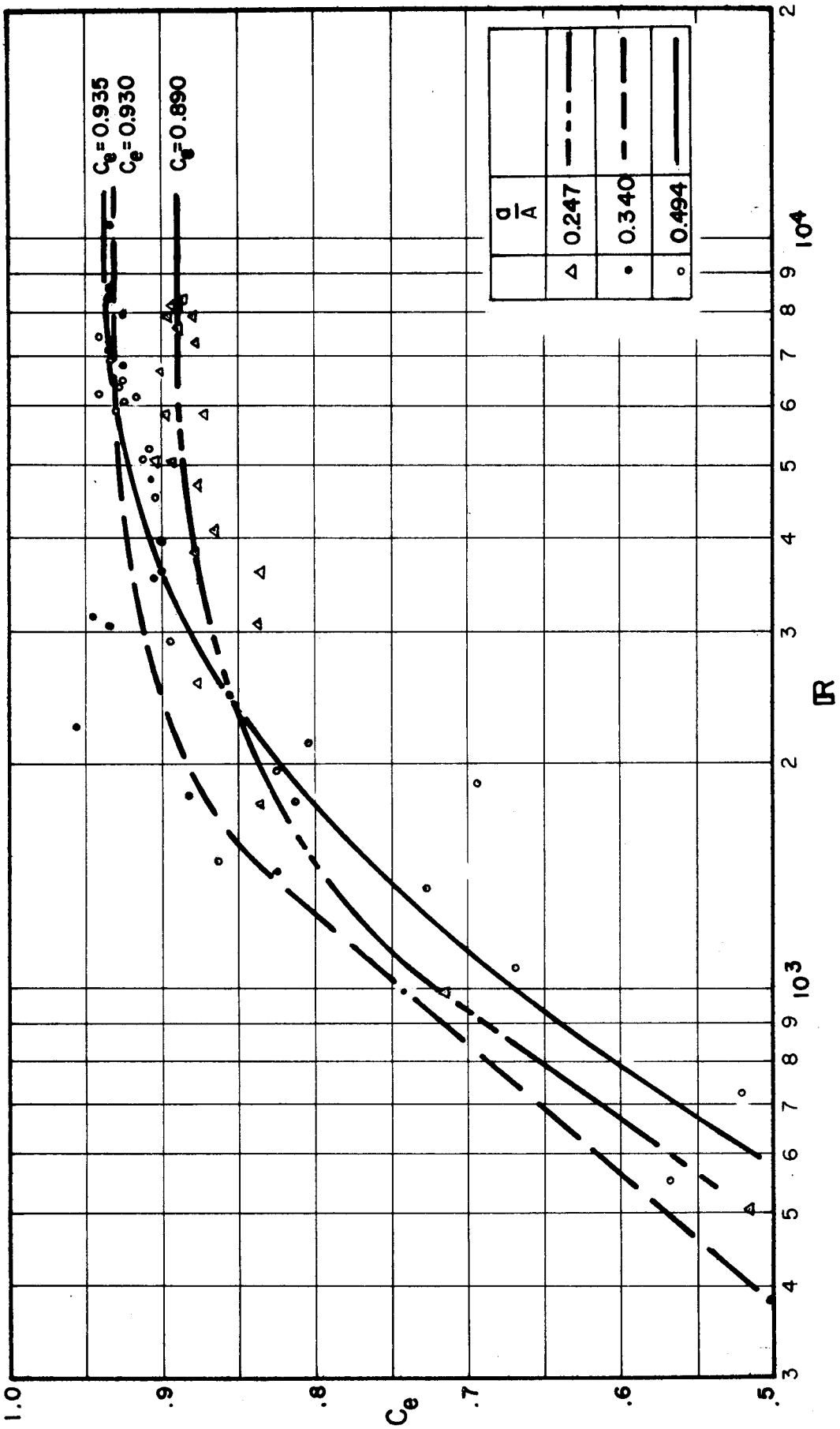

Figure 42. Entrainment Coefficient vs. Port Reynolds Number

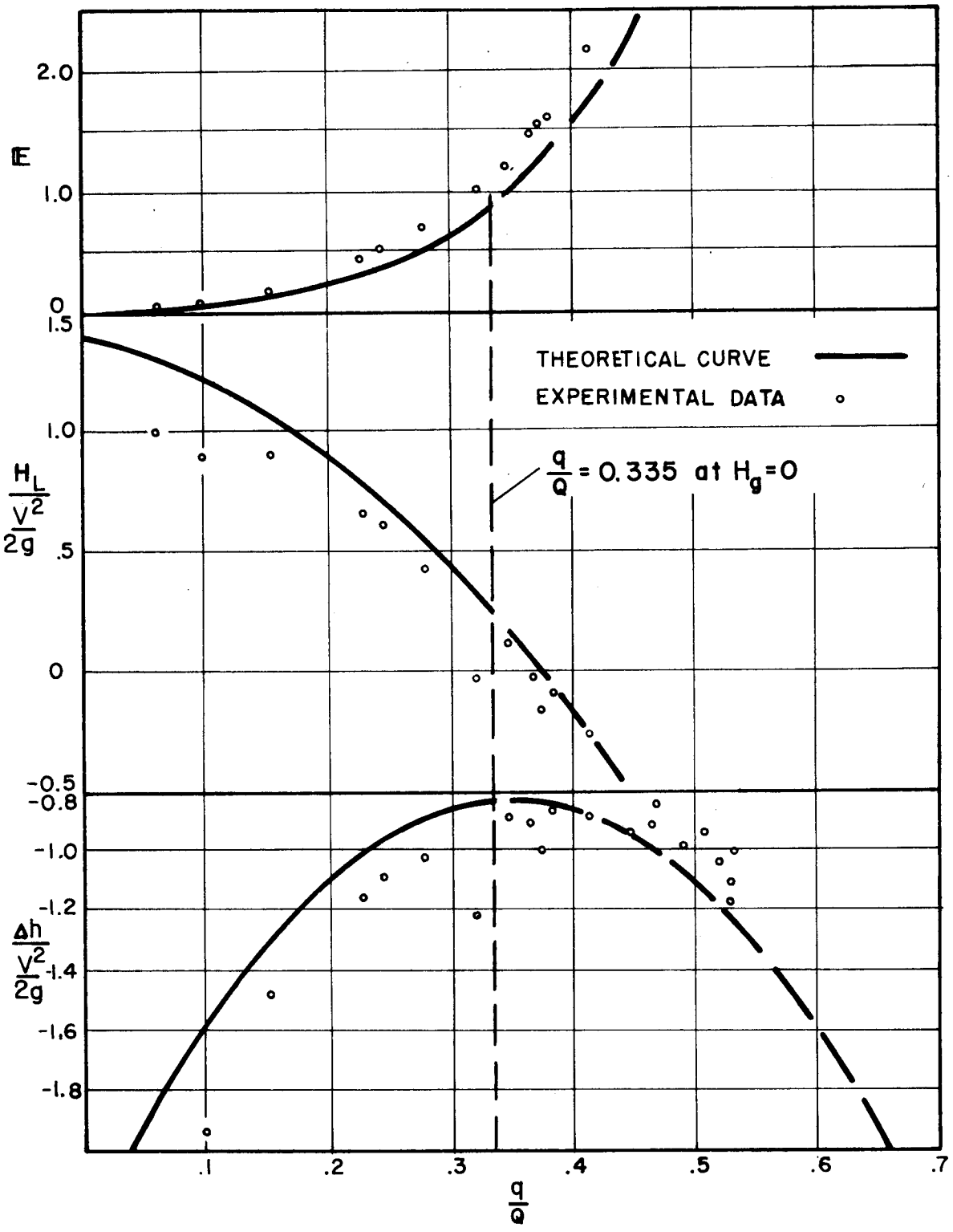

Figure 43. Experimental Results, a/A = 0.247, A_i/A = 0.460

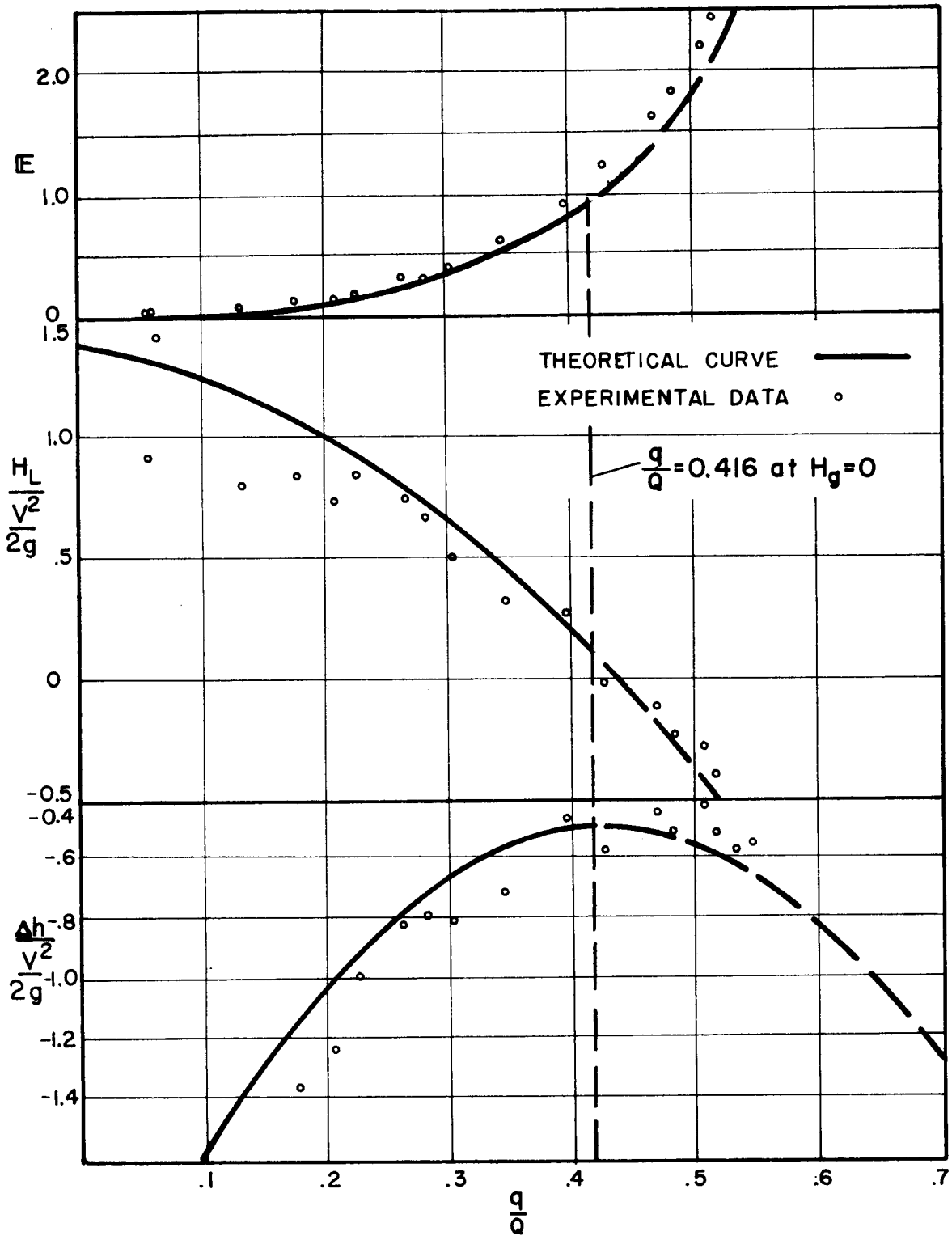

Figure 44. Experimental Results, a/A = 0.340, A_i/A = 0.460

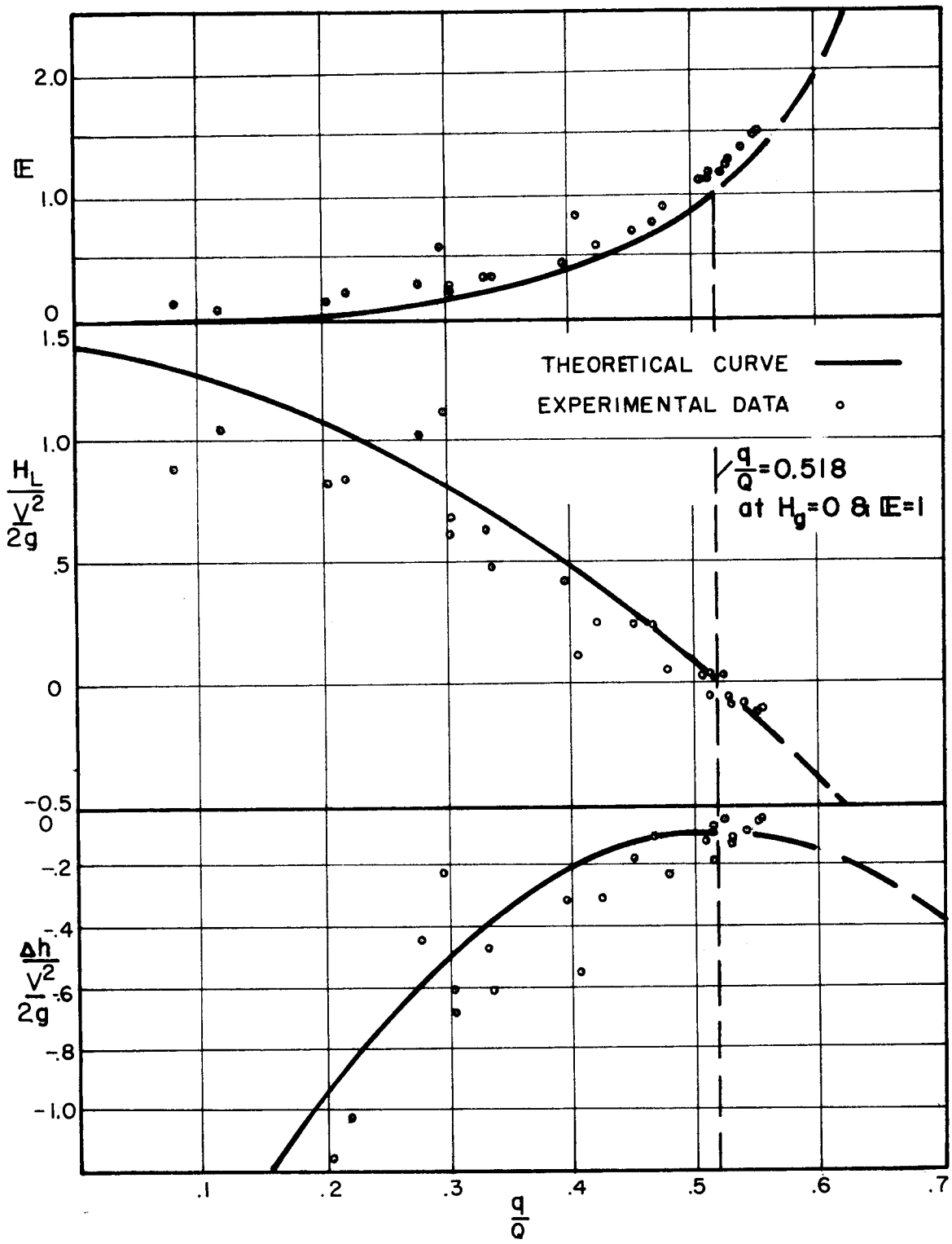

Figure 45. Experimental Results, a/A = 0.494, A_i/A = 0.460

tends to stratify. This latter situation must be investigated because if pronounced stratification exists downstream from the mixing chamber then the original objective of the manifold may be nullified.

The fluid mechanics problem associated with the upstream phase may be characterized as one of coaxial mixing of non-homogeneous, low speed jets within a confined space. A number of investigations have been made of comparable problems in recent years, with interest centered mainly in problems involved with gaseous propulsion of rockets, combustor design, and jet pumps. Most attention has been devoted to gas flows where velocities are high and density differentials, if present, relatively small; or, when density differentials are significant, inertial terms are far more significant than gravitational terms. The three main types of analytical approaches which have been applied to coaxial mixing problems are:

(1) point source of mass, momentum, or heat (most appropriate far downstream from where mixing begins)

(2) integral equations based on assumed velocity profiles

(3) boundary layer approximations of the equations of motion, incorporating appropriate formulations for transport properties (the only approach which yields a detailed picture of the flow field in the initial mixing region).

Fejer et al (1967) have summarized and extended these approaches recently. Whether free or unconfined coaxial jet mixing is considered, all of the approaches depend on axial symmetry in order to make a mathematical attack upon the problem feasible. In addition, axial pressure gradients usually are neglected in the initial mixing area; this assumption is not valid when the initial central jet has a diameter not much smaller than that of the mixing chamber. Examples of subsonic gas flow studies having relatively small central jets are those of Curtet and Ricou (1964) and of Alpinieri (1964). In the latter case density differentials as large as ρ_o/ρ_e = 1/20 were studied, but with equivalent $\mathbb{E}$ values of ≈ unity, for a jet: mixing chamber diameter ratio of 1:4; pressures were found to be essentially constant in the near-nozzle region, and the observed fact that no minimum mixing or tendency toward jet separation occurred when the jets were of different composition (density) but of comparable velocity was attributed

to the fact that the eddy viscosity was altered by the large density gradients. Axial symmetry with respect to density and velocity apparently was observed for values of x/D as large as 10. Hill (1965) considered axial pressure gradients in a confined duct, but again for a flow field in which the central jet was relatively small. Some published procedures for calculating velocity profiles in a zero density differential case were examined during the current study; typical was that of Abramovich (1963), which was found to be inadequate for the geometries being studied because, again, its approximations are more valid when the central jet is relatively small. Likewise, published analyses of buoyant jets in infinite receiving fluids were found to be inadequate and were not applied because of the over-riding effects of the confining walls. The actual flow patterns become very complex and very asymmetric; accordingly, the study being reported here was confined to an experimental approach.

Experimental mixing data were obtained by methods outlined in Chapter II. Parameters varied were flow ratios, density differences, and manifold configuration. The mixing data are again shown in terms of relative mixing expressed as $(c' - c_o)/(c_e - c_o)$. Further, because of the near equality of relative dye concentrations and specific gravities, the interpretation may be made that

$$\frac{c' - c_o}{c_e - c_o} = \frac{\rho' - \rho_o}{\rho_e - \rho_o} \tag{44}$$

Again, ρ' is the effective local time-average (over the withdrawal period) mass density.

A correlation parameter used in presenting the data is a densimetric Froude number defined as

$$\mathbb{F} = \frac{v^2}{\frac{\Delta\rho}{\rho_o} g r_i} \tag{45}$$

where $v = (q/a)$ and r_i is the nozzle radius. The Froude number is an index of the relative tendency of the denser liquid entering at the top of the

mixing chamber to move downward. If there were no mixing and hence no density changes, and if wall confinement were ignored, the coordinates of a jet trajectory could be expressed directly in terms of $\mathbb{F}$. A value of $\mathbb{F} = \infty$ corresponds to a zero density differential situation, in which case the mixing depends only on the relative velocities of the two initial streams and on the distance from the nozzle. For relatively high $\mathbb{F}$ values little asymmetry (for the fully open annulus) is expected near the nozzle, but gravitational effects become more significant as the distance from the nozzle increases. For relatively low $\mathbb{F}$ values, either the initial dilutant inflow velocity is low or initial density differences are high; in either case, it might be anticipated that gravitational forces may be most important and stratification could result. With partial closure of the annulus, the increased turbulence due to greater jet expansions could expedite the mixing process and perhaps override some of the effects of changes in $\mathbb{F}$.

Mixing data presented have been divided into four categories. Dye concentration samples were withdrawn at appropriate cross-section locations in the test section to examine:

I. Development of mixing for the fully open annulus.

II. Effect of port configuration on the mixing process; i.e., effect of asymmetric entrance conditions.

III. Effects of changes in flow ratio.

IV. Effects of variation in $\mathbb{F}$.

A representative development of mixing throughout the test section is shown in Fig. 46, where data are given for x/D values ranging from 5.7 to 50.0. The pertinent parameters of $\mathbb{F} = 26$, $\Delta\rho/\rho_o = 0.010$, $a/A = 0.494$, $q/A = 0.39$, and $v/V_i = 0.59$ for the case shown in Fig. 46 are considered representative in terms of extension to prototype performance. The data obtained over the test section of length = 50 D indicate the following:

1) For $x/D < 7.4$, little dilution occurs in the lower half of the conduit, but that the initial high value of dye concentration disappears quickly in the upper region. Evidently the initial velocity difference of the two streams

is dissipated quickly, and gravity effects are more significant than the effects of interfacial shear stress.

2) Most mixing occurs in the region $7.4 < (x/D) < 17.5$.

3) Additional mixing occurs over the range $17.5 < (x/D) < 50.0$, but this extra mixing is relatively minor compared to the mixing achieved already upstream. Lateral variations have nearly vanished at $x/D = 29.5$, and lateral mixing gains downstream from $x/D = 30$ are negligible. A certain final degree of vertical stratification is noted.

Based upon the results shown in Fig. 46, again considered to represent a typical symmetrical flow case, the decision was made to limit the sampling to the three stations having stations of $x/D = 5.7$, 10.0, and 29.5, considered as ones which would provide information typical of the various stages of the mixing process.

Effects of port configuration changes (asymmetry and changes in relative inflow areas) are shown in the data of Figs. 47-52. The value of a/A was varied while A_i/A, $\Delta\rho/\rho_o$ and $\mathbb{F}$ were held constant at 0.460, 0.035 and 26, respectively. In Figs. 47, 49, and 51, with v held constant and $v/V_i = 0.59$ in each case (q/Q variable) it is observed that:

1) Reasonably uniform mixing has resulted at $x/D = 29.5$ for all three cases.

2) For successively larger a/A ratios (smaller plugs) and greater initial interfacial areas of the two jets the uniformity of mixing decreases. The jet expansion process is more efficient in mixing than is initial interfacial shear.

On the other hand, in Figs. 48, 50, and 51 with q/Q held constant at 0.39 (v/V_i variable) it is seen that the effect of the small plug is negligible and produces essentially the same mixing at $x/D = 29.5$. Figure 48 with $v/V_i > 1.0$ is outside the range of outfall applicability but is useful when comparing mixing patterns of various a/A when the dilution ratio q/Q is constant. Further, best final mixing is achieved with the largest plug ($a/A = 0.247$) shown in Fig. 48, a result consistent with that shown in Fig. 47 vs. Figs. 49 and 51.

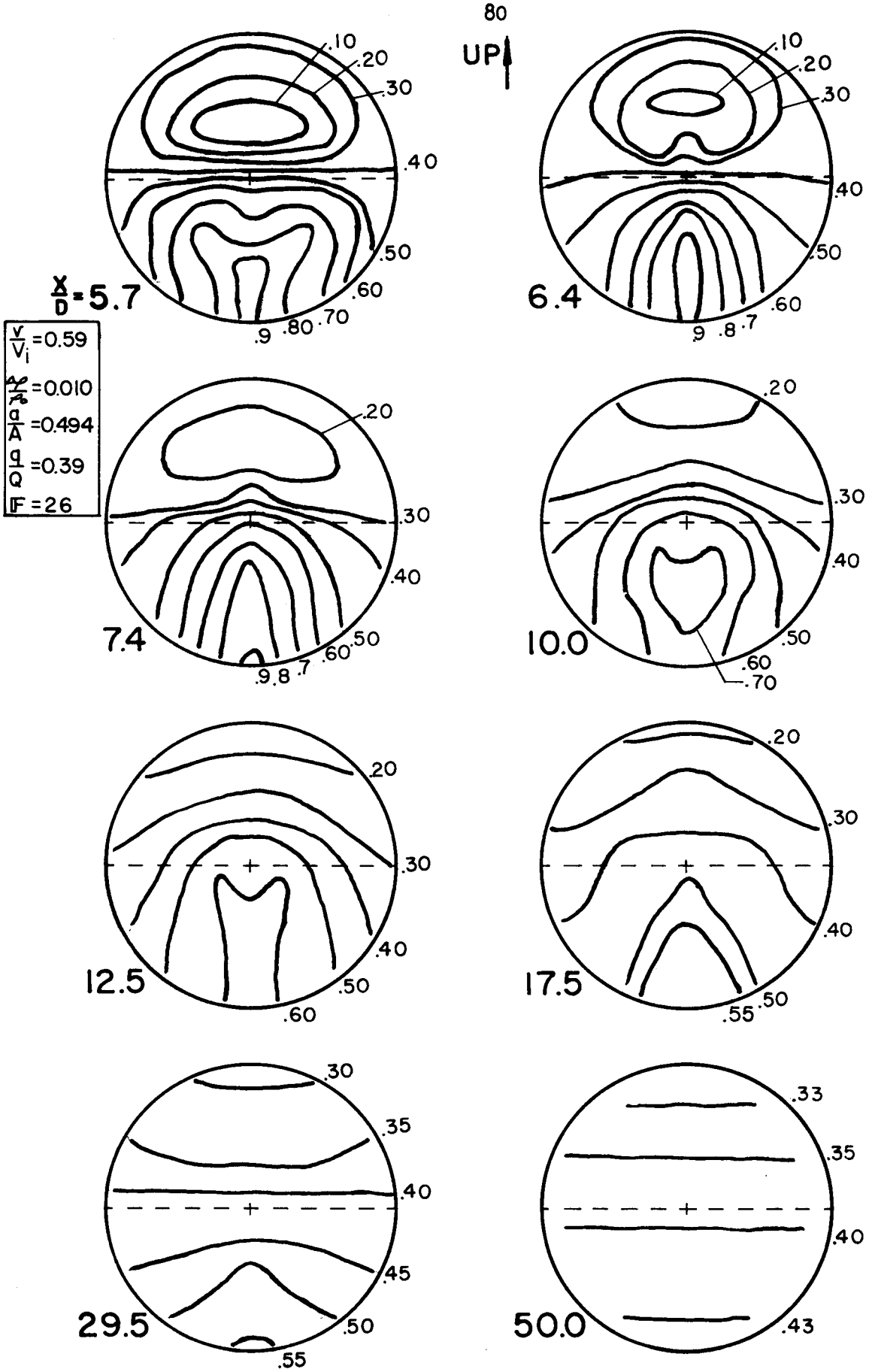

Figure 46. Dilution Mixing Contours, $(c'-c_o)/(c_e-c_o)$, Axi-Symmetrical Port

Effects of geometry changes are summarized on Fig. 52, on which are shown the vertical centerline profiles of the concentration patterns of Figs. 47-51. Figure 52(a) is for $v/V_i = 0.59$ and Fig. 52(b) is for $q/Q = 0.39$. While the vertical profiles are representative of the mixing over the entire cross-section only at stations well downstream from the nozzle, Fig. 52 shows that final downstream mixing (at $x/D = 29.5$) is slightly more dependent on the dilution ratio than on the area ratio. Figure 52 also shows that the final stratification is, in reality, slight; in Fig. 52(b) the uniform fully mixed concentration given by Eq. 21 is shown at all stations.

Effects of changes in flow ratio (Category III) are shown in Figs. 47-54, when port geometry, density differences and Froude numbers were held constant and q/Q was varied. Figures 47-54 all apply for $\mathbb{F} = 26$, $v = 1.30$ fps, and $\Delta\rho/\rho_o = 0.035$. Better mixing, as measured by uniformity over the entire cross-section as opposed to stratification, was achieved with higher velocity differentials or, because v was held constant, decreasing values of q/Q. Figure 53, showing results for three dilution ratios at the nominal $a/A = \frac{1}{2}$ ratio, shows this trend clearly. Because the head loss, H_L, decreases with increasing q/Q the improved uniformity is associated with relatively larger head losses for a particular configuration.

Figure 54 summarizes downstream ($x/D = 29.5$) centerline dilution profiles for the fully open annulus. Increased dilution was obtained by holding v constant and decreasing Q_o so that V_i was decreased. The results shown in Fig. 54 are taken from the right-hand column of Fig. 53, and illustrate more clearly the conclusion given above.

It is noted that the concentration profile on the vertical centerline tends to have an average value of the relative concentration which is approximately equal to the q/Q ratio for the run. Complete agreement cannot be expected for two reasons: the profile ignores the remainder of the cross-section, and no consideration of velocity profiles has been made that would account for the correct spatial distribution of dye transport rates. For example; the concentration profiles yield extreme values near the top and bottom of the conduit where the local velocities are lower than the average

over the section.

Effects on the mixing patterns due to changes in $\mathbb{F}$ (Category IV) are shown in Figs. 55-57. All four tests were at the same q/Q = 0.39 and for the same fully open annulus. In three runs the initial density difference was varied to obtain the different $\mathbb{F}$ values, and in the fourth test the dilutant flow rate was reduced. The significant parameters are listed in the following table.

Fig. 55	q (cfs)	$\Delta\rho/\rho_o$	$\mathbb{F}$	a/A	q/Q
a)	0.014	0	∞	0.494	0.390
b)	0.014	0.010	86	0.494	0.390
c)	0.014	0.035	26	0.494	0.390
d)	0.0047	0.035	2.9	0.494	0.390

The dilution contours in Fig. 55 apply at x/D = 5.7. For $\mathbb{F} = \infty$ ($\Delta\rho/\rho_o = 0$) the measured concentrations were axi-symmetric (within experimental error for the technique used) as expected. Changes in density but at a constant $\mathbb{F}$ produce little change in the mixing pattern. Further tests, not detailed here, confirmed this by establishing dilution contours nearly identical with those shown in Fig. 51 for $\mathbb{F} = 26$, a/A = 0.494, and $\Delta\rho/\rho_o = 0.010$ and 0.025. Even at x/D = 5.7 which is quite close to the nozzle, the flow tends toward stratification at the lower Froude number value $\mathbb{F} = 2.9$. The vertical centerline profiles from Fig. 55 are shown in Fig. 56, in which they are compared to initial conditions at the nozzle. Variations in $\mathbb{F}$ produce markedly different patterns early in the mixing chamber.

Figure 57 shows the progressive mixing over the range $0 < (x/D) < 29.5$ for the two lowest $\mathbb{F}$ values in the test series. The stratified flow which develops close to the nozzle for $\mathbb{F} = 2.9$ persists to the end of the mixing section. In contrast, a continuous increase in uniformity with increasing x/D occurs for the case of $\mathbb{F} = 26$. This latter was observed also in further tests at $\mathbb{F} = 86$ and $\mathbb{F} = \infty$ (not detailed here). The value of $(c' - c_o)/(c_e - c_o) = 0.39$ is shown to indicate the degree to which fully uniform mixing might be approached with increasing x/D.

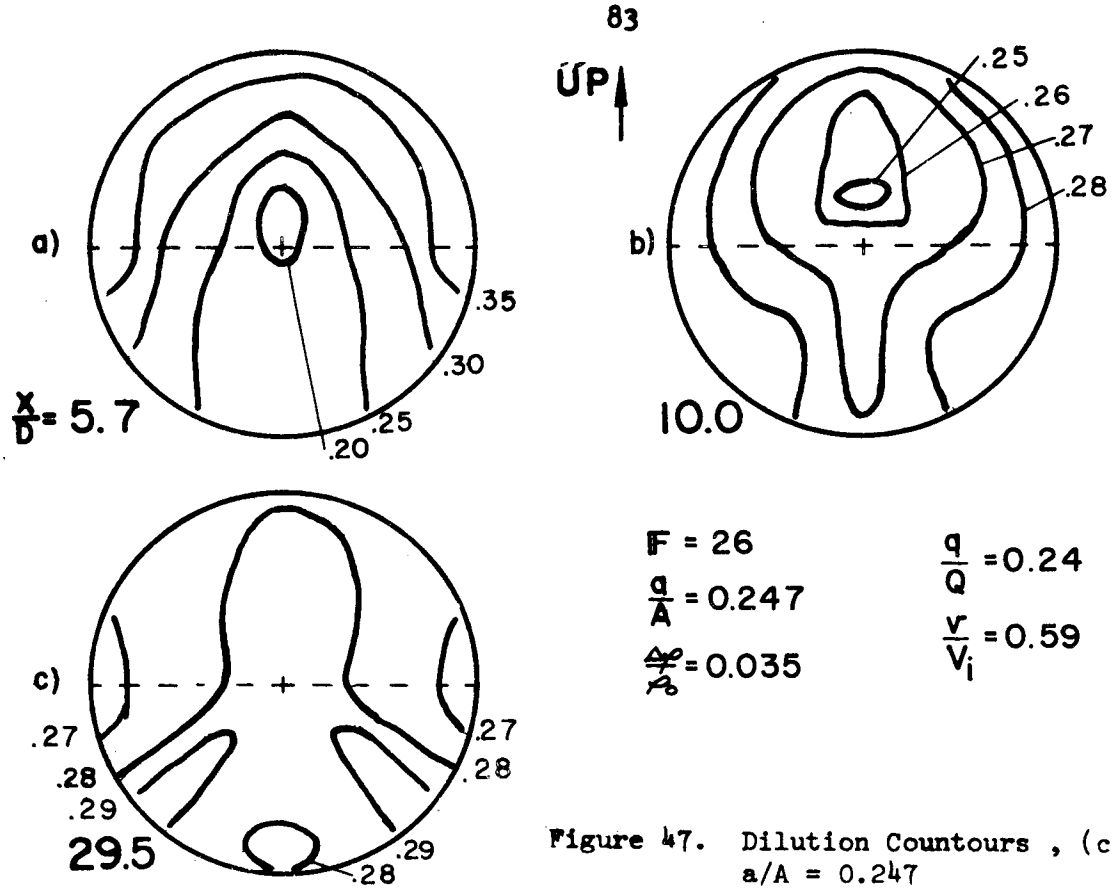

Figure 47. Dilution Countours , $(c'-c_o)/(c_e-c_o)$, a/A = 0.247

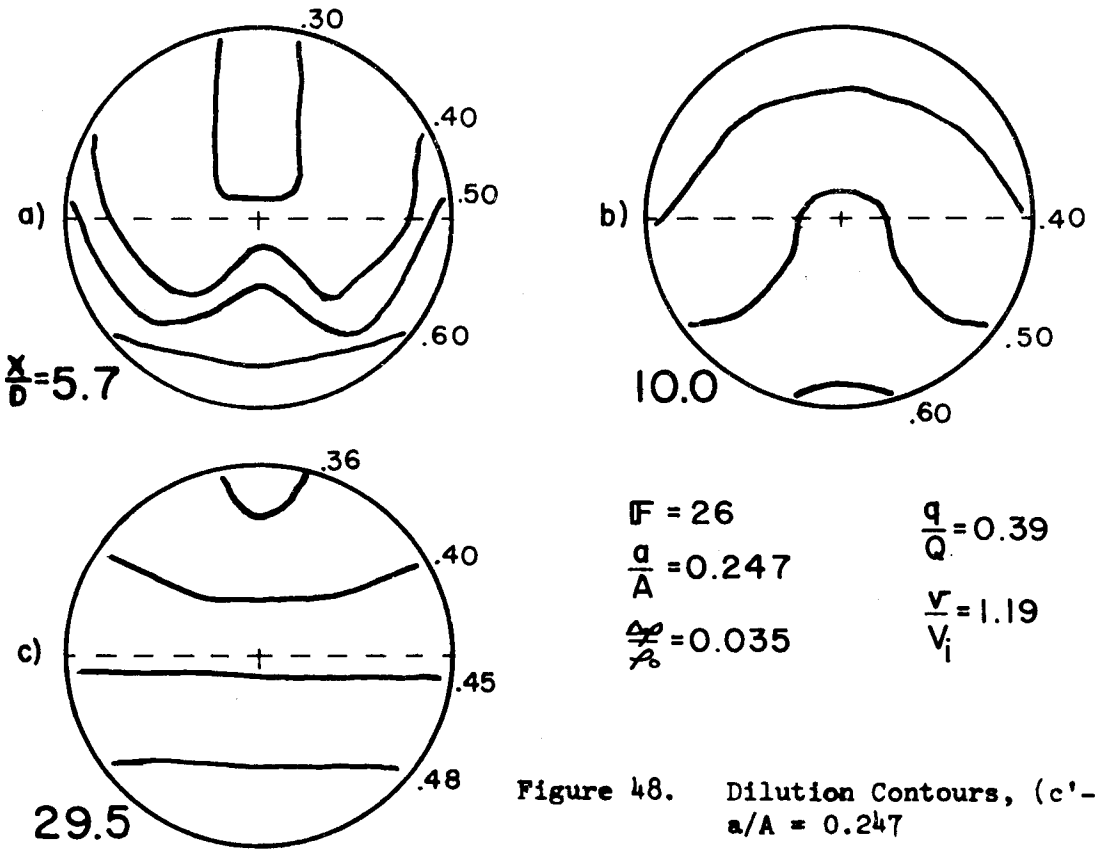

Figure 48. Dilution Contours, $(c'-c_o)/(c_e-c_o)$, a/A = 0.247

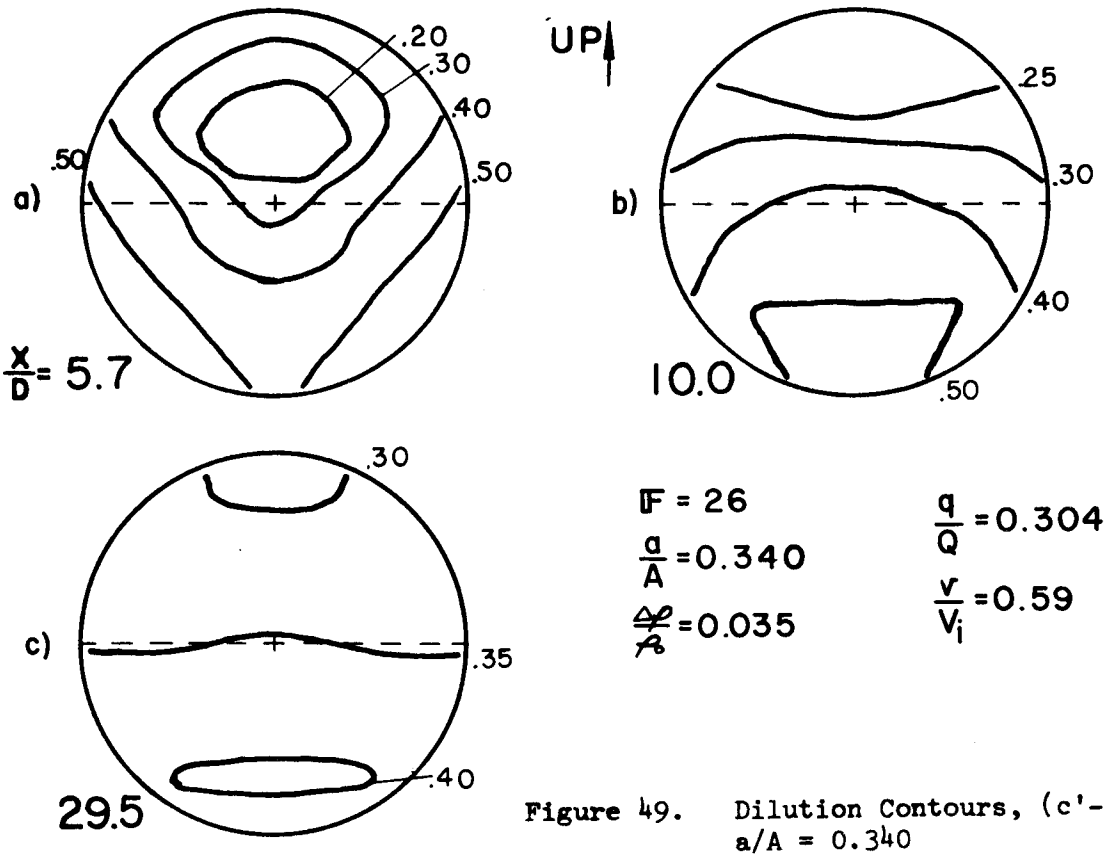

Figure 49. Dilution Contours, $(c'-c_o)/(c_e-c_o)$, a/A = 0.340

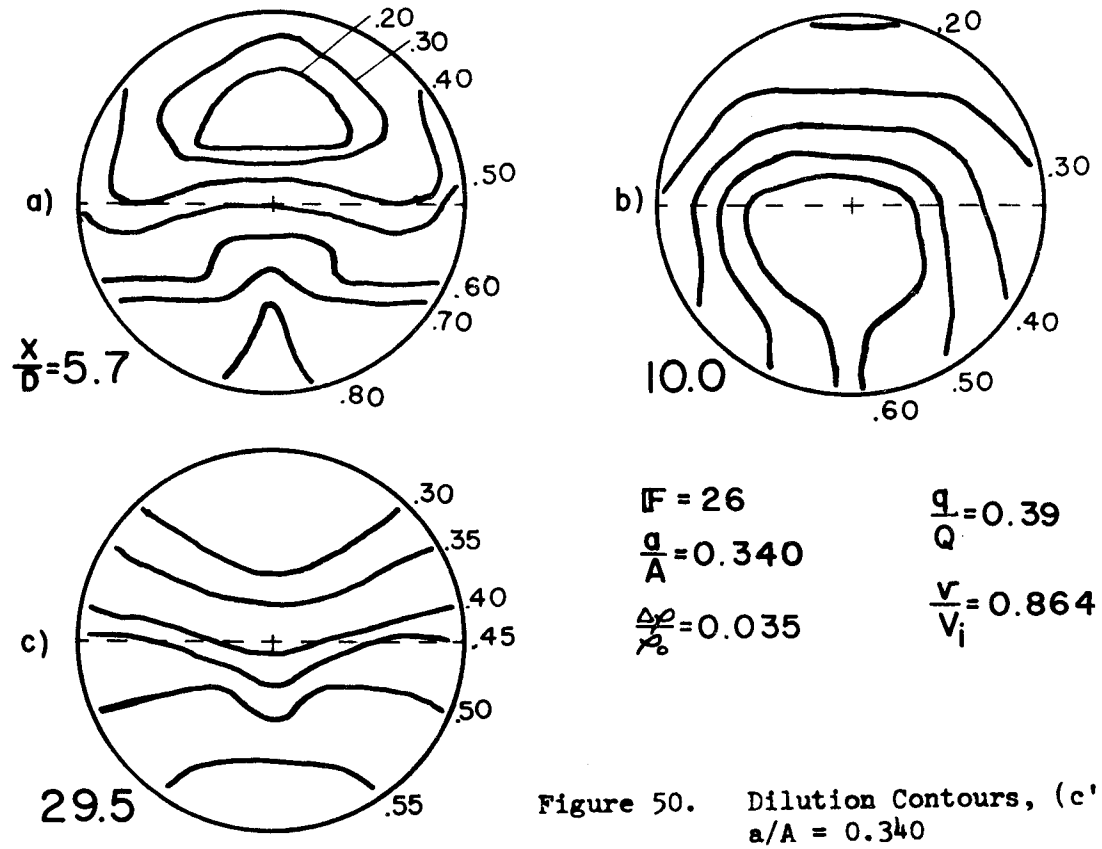

Figure 50. Dilution Contours, $(c'-c_o)/(c_e-c_o)$, a/A = 0.340

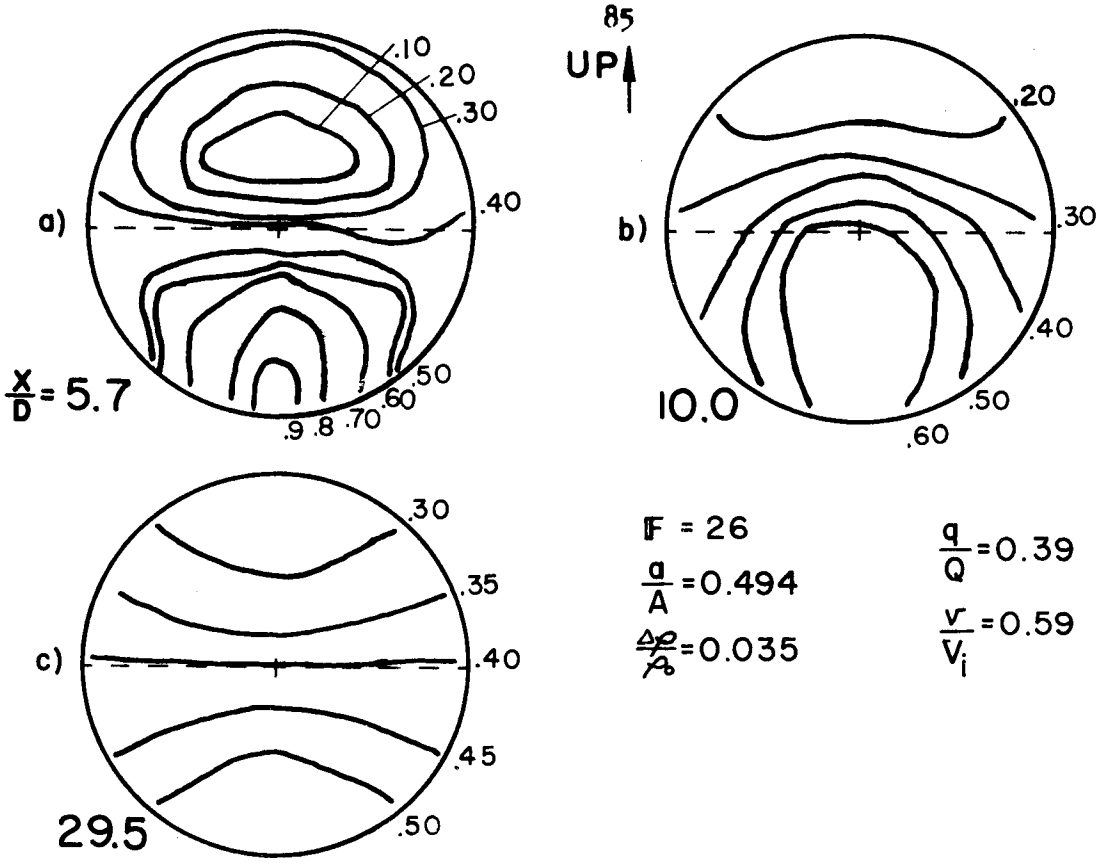

Figure 51. Dilution Contours, $(c'-c_o)/(c_e-c_o)$, a/A = 0.494

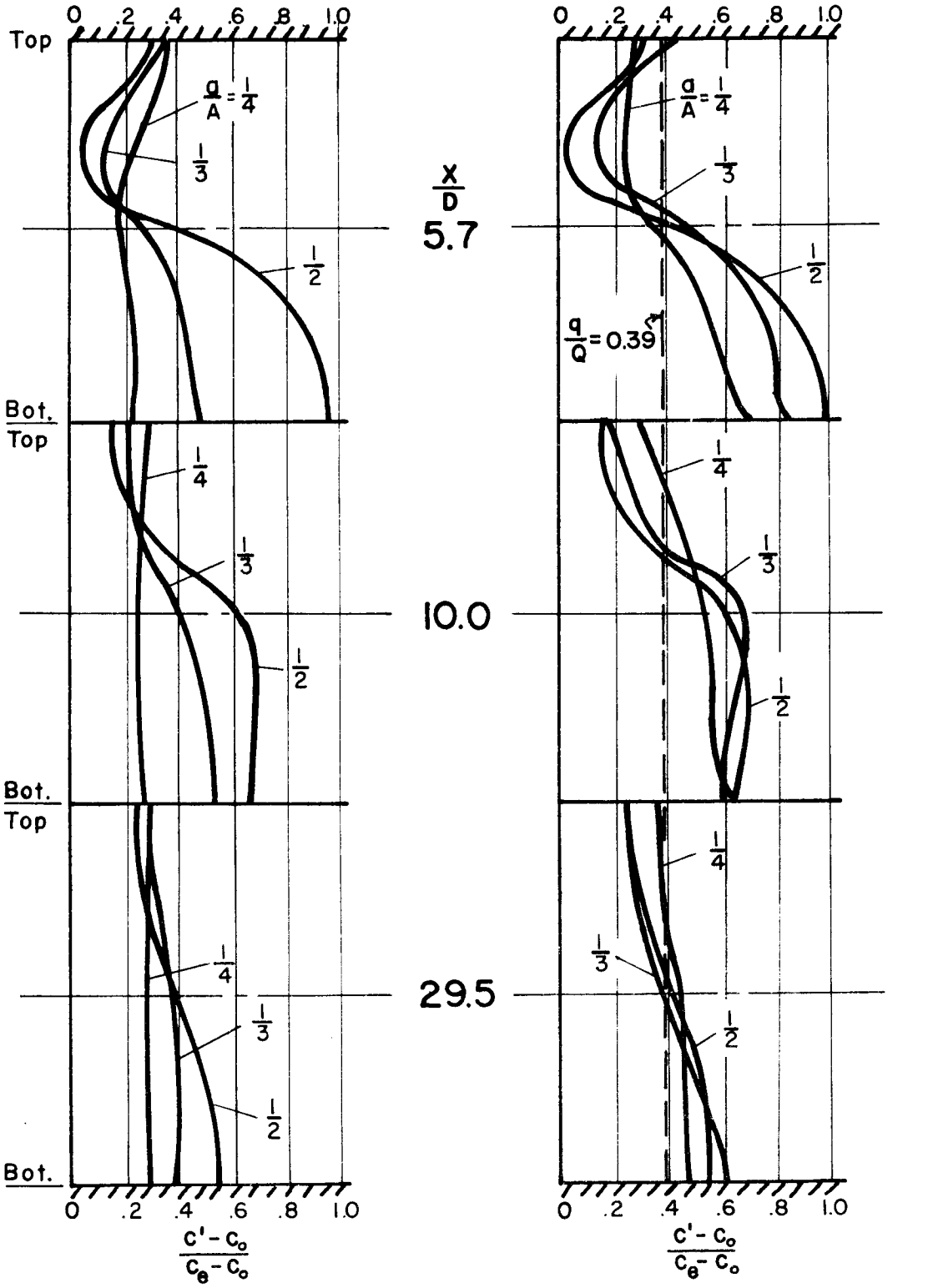

a) $\frac{V}{V_j}=0.59$, $F=26$, $\frac{\Delta\rho}{\rho_o}=0.035$

b) $\frac{q}{Q}=0.39$, $F=26\frac{\Delta\rho}{\rho_o}=0.035$

Figure 52. Dilution Profiles on Vertical Centerline

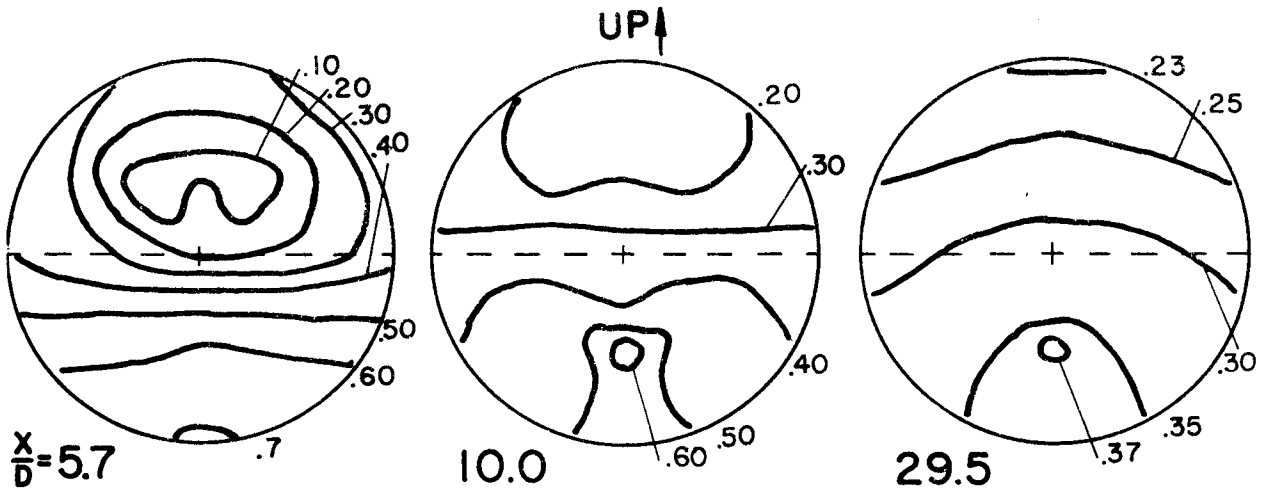

a) $\frac{q}{Q}=0.30, \frac{v}{V_i}=0.40$, IF=26, $\frac{\Delta\rho}{\rho_o}=0.035$, $\frac{a}{A}=0.494$

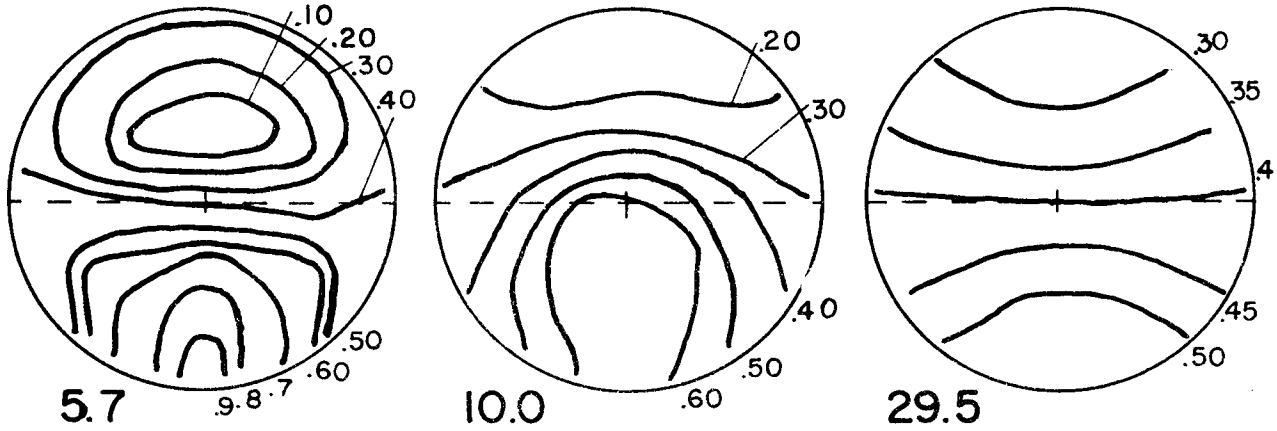

b) $\frac{q}{Q}=0.39$, $\frac{v}{V_i}=0.59$, IF=26, $\frac{\Delta\rho}{\rho_o}=0.035$, $\frac{a}{A}=0.494$

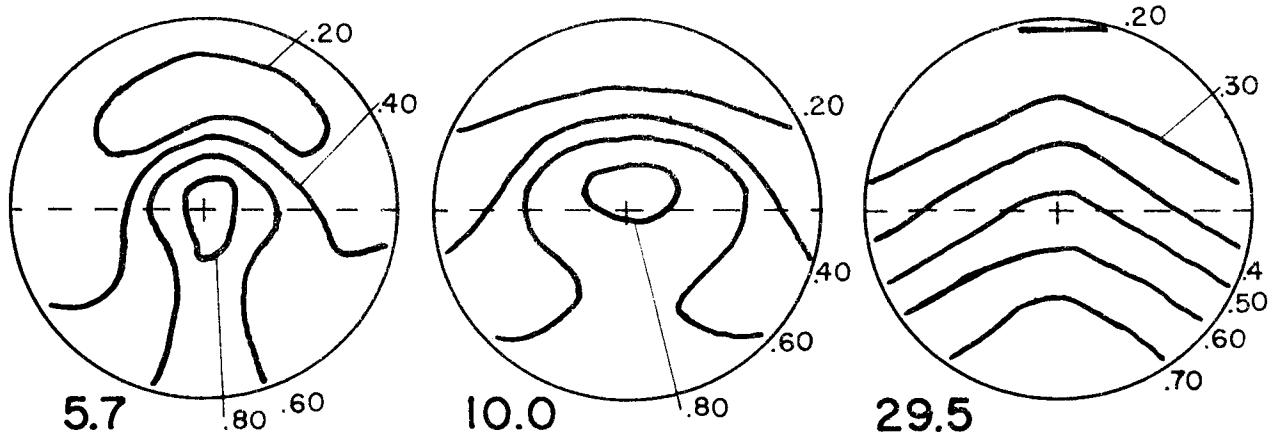

c) $\frac{q}{Q}=0.50$, $\frac{v}{V_i}=0.94$, IF=26, $\frac{\Delta\rho}{\rho_o}=0.035$, $\frac{a}{A}=0.494$

Figure 53. Dilution Contours, $(c'-c_o)/(c_e-c_o)$, for Various Dilution Ratios

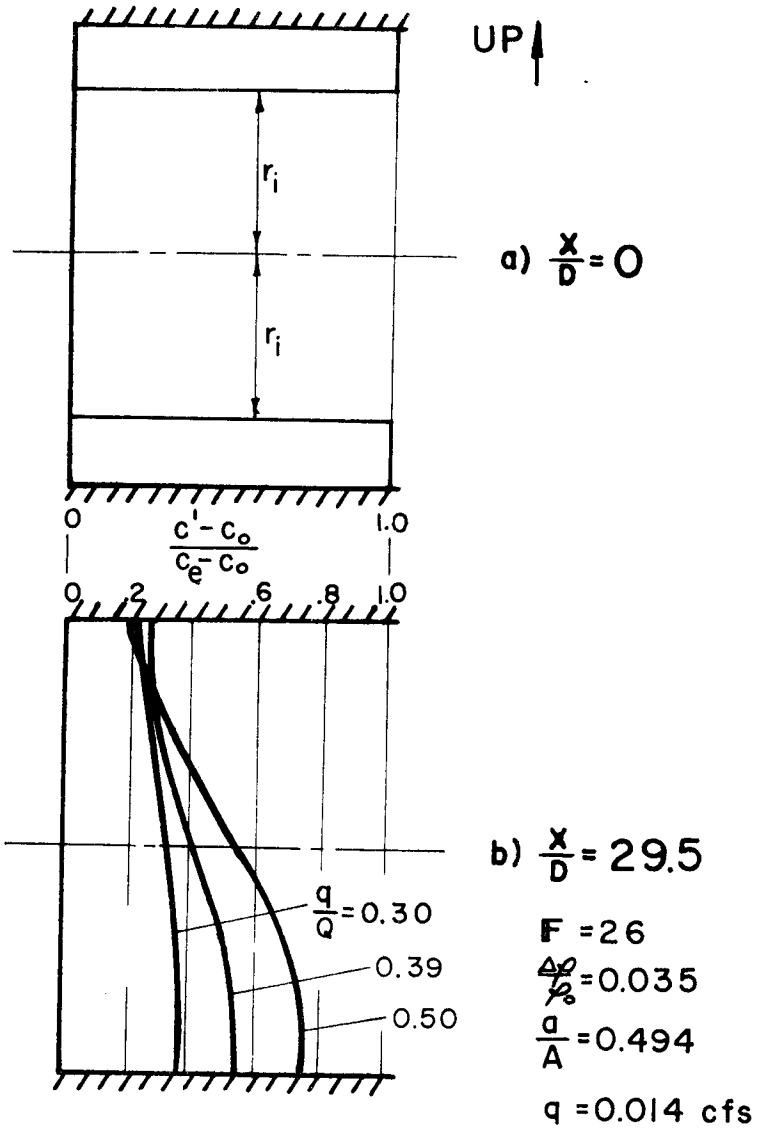

Figure 54. Dilution Profiles for Various Dilution Ratios

The mixing investigations may be summarized by listing some conclusions:

1) The required mixing chamber length for terminal mixing within the conduit is approximately 15-20 conduit diameters when density differentials appropriate to marine outfalls are involved. The terminal mixing may involve some stratification but will not vary appreciably with increased distance along the conduit. By contrast, the studies of Mueller (1964) and of Silvester and Mueller (1968), in which the annular port manifold was investigated as a water jet pump, suggested a required chamber length of about 7 conduit diameters to obtain the optimum pressure rise in excess of frictional losses in the mixing chamber for zero initial density difference.
2) Partial closure of the annulus (by plugging the lower half) produced a better uniformity of mixing within the conduit than obtained with the fully open annulus for the same q/Q, and with smaller a head loss H_L.
3) Uniformity of mixing increased with decreasing q/Q values. From the standpoint of outfall application, the larger dilution ratio q/Q is more significant.
4) Density changes of the dilutant fluid had relatively little effect on final mixing in the mixing chamber when $\mathbb{F}$ was held constant.
5) Higher $\mathbb{F}$ values lead to improved uniformity of mixing.
6) Downstream stratification tends to occur with low values of $\mathbb{F}$; consequently, low densimetric Froude numbers are undesirable for outfall use because the lighter (mostly initial effluent) fluid would end up at the top of the discharge jet.

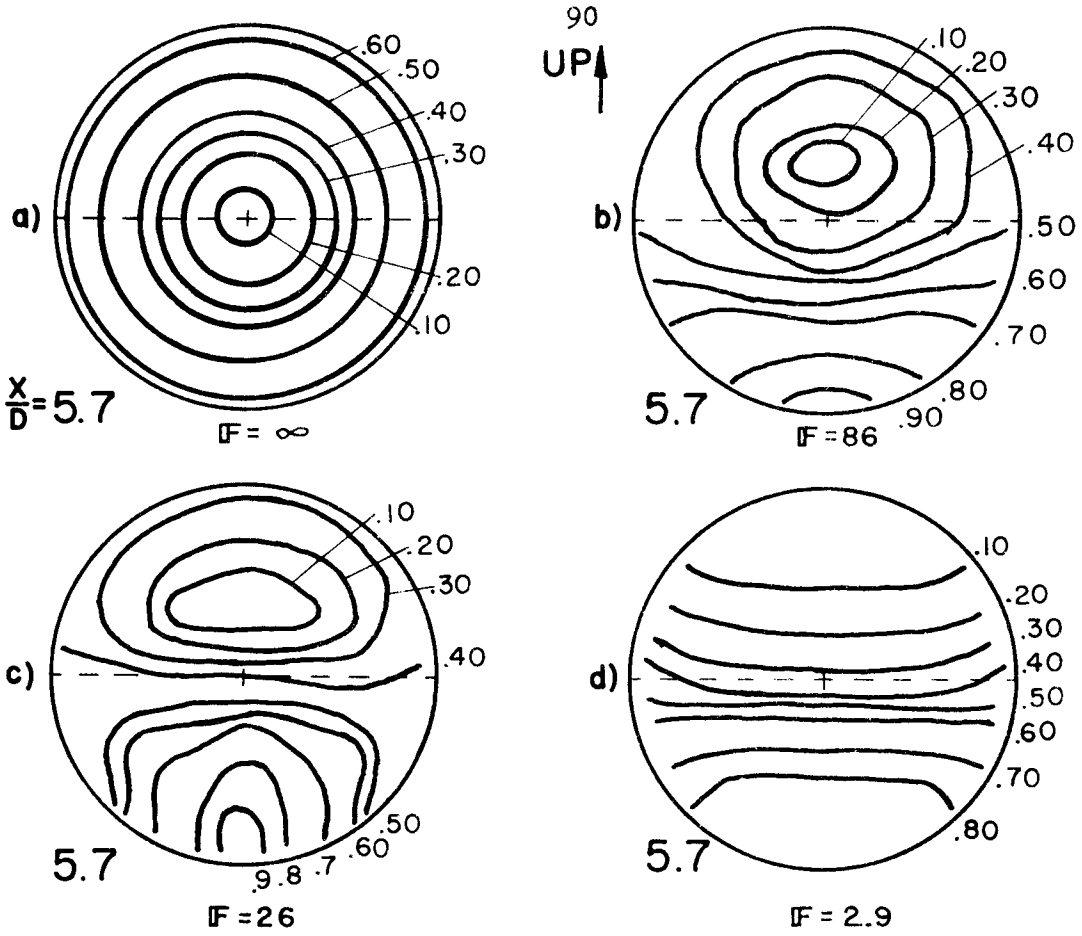

Figure 55. Dilution Contours, $(c'-c_o)/(c_e-c_o)$ for Various Froude Numbers

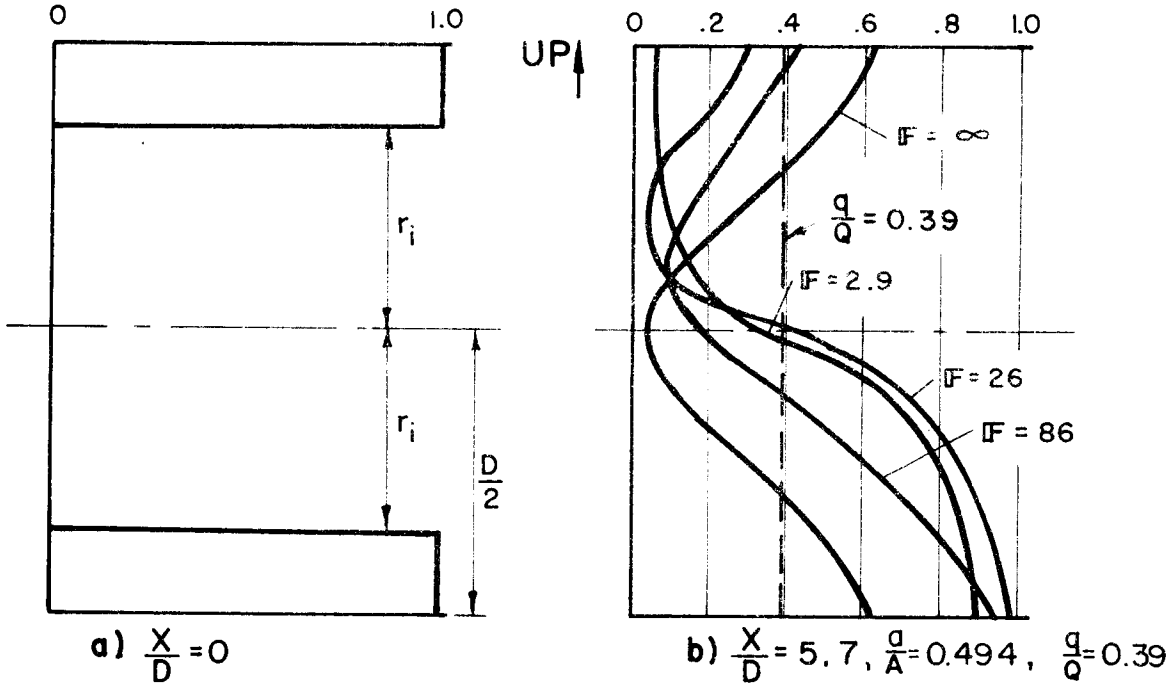

Figure 56. Dilution Profiles, $(c'-c_o)/(c_e-c_o)$ for Various Froude Numbers

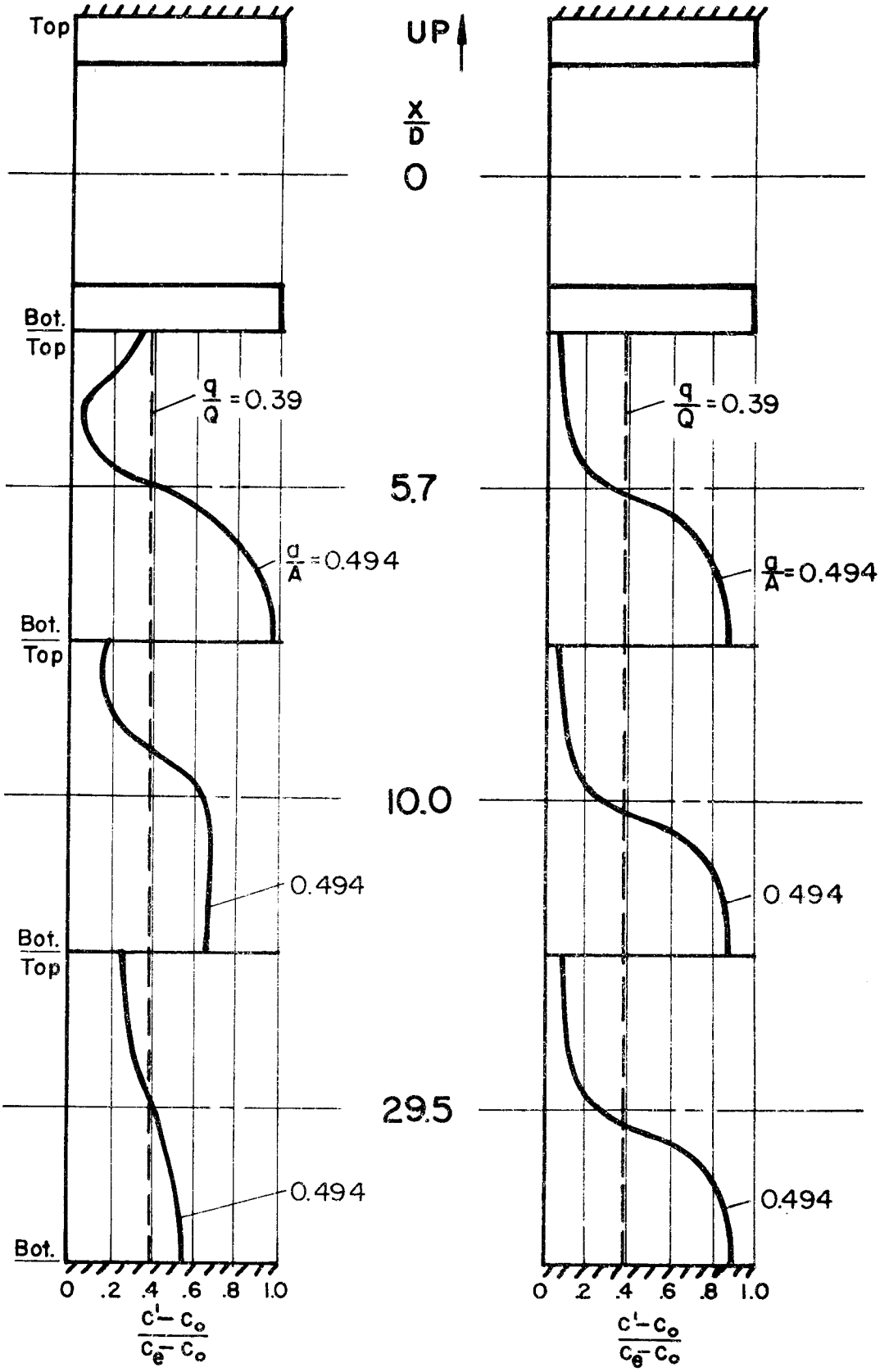

a) IF = 2.6, $\frac{q}{Q}$=0.39, $\frac{\Delta\rho}{\rho_o}$=0.035 b) IF = 2.9, $\frac{q}{Q}$=0.39, $\frac{\Delta\rho}{\rho_o}$=0.035

Figure 57. Dilution Profiles for Various Froude Numbers

V. CONCLUSIONS

The objective of the present study was to obtain data concerning the external hydraulic characteristics which would enable a designer to evaluate the possible use and efficacy of suction manifolds in predilution schemes in marine sewer outfalls. Test data were obtained for two types of manifolds, each of a relatively simple geometry, and representing between them elements of the basic geometries to be expected in most suction manifolds. Mixing characteristics were investigated for the annular-port manifold to determine if stratification occurs within the conduit downstream from the inlet port; such stratification would be detrimental to the manifold operation.

Relative hydraulic performances of the two classes of manifolds tested are shown on Fig. 58. All values shown are experimental data, and the actual configurations tested have been identified by their 'nominal-size' descriptions. The comparison made is on the basis of dilution ratio, a/Q, vs. dimensionless head loss charged to the manifold, $H_L/(V^2/2g)$. Data for the side-port manifolds indicate values at the limiting condition of $\mathbb{E} = 1$, and are taken from Figs. 20 and 21, so that the results are for single-port manifolds only. The annular-port results are also for the case of $\mathbb{E} = 1$, and are taken from Figs. 43-45. The comparison between the two geometrical forms is not completely valid because the annular-port manifolds should be examined at their limiting point of operation, namely, at $H_g = 0$. However, as indicated on Fig. 40, for the manifold of $A_i/A = \frac{1}{2}$ = constant and a/A variable, the values of $\mathbb{E}$ approach unity when $H_g = 0$ for the range of a/A covered by the laboratory tests.

Figure 58 does give a sufficiently qualitative comparison of the two configurations. As might be expected, the annular port is much more satisfactory on the basis of hydraulic characteristics, yielding larger dilution ratios for relatively smaller head losses over much of the range. The two examples having equal ratios of port area: conduit area are the annular port of $a/A = \frac{1}{4}$ and the side port of $d/D = \frac{1}{2}$; the annular port

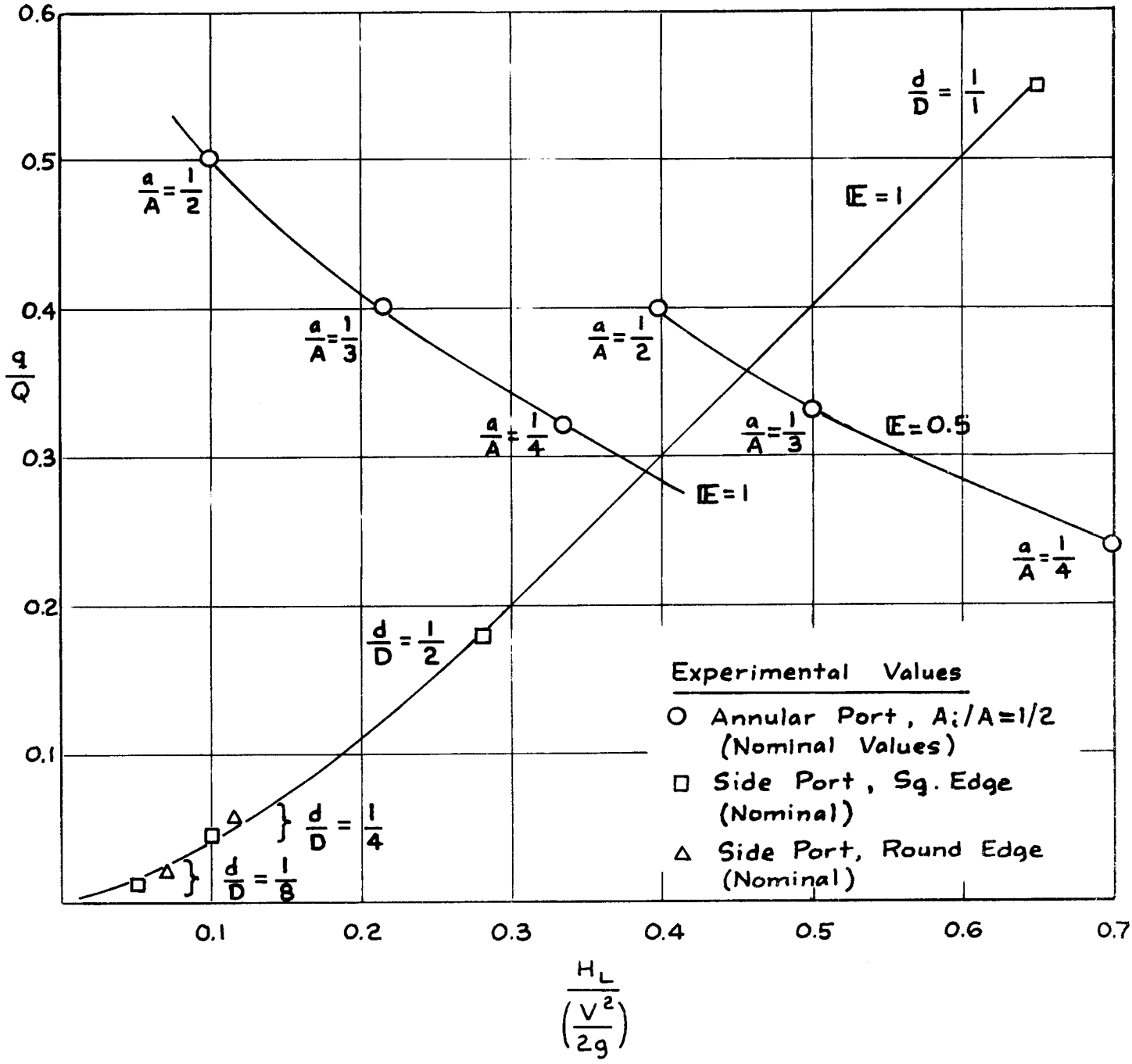

Figure 58. Relative Performance of Side-Port and Annular-Port Manifolds

provides an approximate 75 percent increase in dilution ratio for an approximate 20 percent increase in head loss based upon the velocity in the downstream conduit. Again, these figures are for the arbitrary case of $E = 1$, which would not be a condition of normal operation. A partial curve at a more realistic value of $E = 0.5$ is shown for the annular-port manifold and illustrates how performance falls off at more normal points of operation.

The evaluations made here are on the basis of relative external hydraulic characteristics only. Such items as determination of operating conditions under tidal variations of water surface elevation and of installation and operating costs have not been considered, although it may be pointed out that the installation of the annular-port manifold requires the careful alignment of the nozzle, the annulus, and the mixing chamber in order to achieve optimum performance and hence construction costs may be much higher than for the relatively simpler side-port manifolds. Vanes to minimize swirling motions at the port entrance also should be considered.

Although effects of scale and intensity of turbulence on the mixing process were not investigated and no attempts were made to estimate any turbulent diffusion coefficients, it is expected that the trends in mixing performance of prototype-sized devices should follow those trends observed in the laboratory tests. The densimetric Froude numbers used in the mixing tests with the annular-port manifolds are consistent with the range of outfall Froude numbers in typical marine installations such as listed by Pearson (1956) and by Frankel and Cumming (1965). For example, the following test parameters may be considered: $a/A = \frac{1}{2}$, $A_1/A = \frac{1}{2}$, $q/Q = 0.39$, $= 26$. This combination is one of those which was reported in Chapter IV. Using a typical marine installation value of $\Delta\rho/\rho_o = 0.025$ and assuming full mixing with no diffuser leads to a value of an equivalent discharge Froude number $V/\sqrt{(\Delta\rho/\rho)gD} \approx 6$, which is well within the ranges cited by the two above references. The laboratory mixing studies thus spanned the range of outfall operation.

Terminal mixing was found to be adequate in the annular-port manifolds

when F was sufficiently high. While no mixing studies were made with density differentials in tests on the side-port manifolds, the jet deflection observations and the zero density differential data would indicate that at the low E values associated with outfall operation the inflow would not penetrate immediately to the conduit invert and so mixing might be adequate to go along with the overall dilution. This is a point of study still to be undertaken.

The idea of using manifolds for predilution in sewer outfalls is not necessarily new or original. For example, a modified annular-port manifold proposed in 1966 for the discharge end of an effluent main discharging into a shallow river was discussed by Silvester (1967), during the time period of the present study. The device suggested was more along lines of a conventional jet pump configuration, and density differentials were not involved because of the fresh-water receiving fluid.

It is concluded that the suction manifold does have potential value for use in marine outfalls, particularly where advantage may be taken of local stratification so that the terminal discharge may not reach the water surface or where the outfall must be placed in shallow water so that an extension into deep water would be very costly.

VI. BIBLIOGRAPHY

Abraham, G. 1967. "Jets with Negative Buoyance in Homogeneous Fluid", Journal of Hydraulic Research, Vol. 5, No. 4, pp. 235-248.

Abramovich, G. N. 1963. "The Theory of Turbulent Jets", MIT Press Cambridge, Mass.

Alpinieri, L. J. 1964. "Turbulent Mixing of Coaxial Jets", AIAA Journal, Vol. 2, No. 9, pp. 1560-1567.

Blaisdell, F. W. and Manson, P.W. 1963. "Loss of Energy at Sharp-Edged Pipe Junctions", Technical Bulletin No. 1283, Agric. Research Service, U.S. Dept. of Agric., Washington, D.C.

Brooks, N. H. and Koh, R.C.Y., 1965. "Discharge of Sewage Effluent from a Line Source into a Stratified Ocean", Proc. Eleventh International Congress for Hydraulic Research, Leningrad, USSR.

Callaghan, E. E. and Ruggeri, R.S. 1948. "Investigation of the Penetration of an Air Jet Directed Perpendicularly to an Air Stream", Technical Note 1615, NACA (presently, NASA), Washington, D.C.

Curtet, R. and Ricou, F. P. 1964. "On the Tendency to Self-Preservation in Axisymmetric Ducted Jets", ASME Paper No. 64-FE-20.

Fejer, A. A., Torda, T. P. Boehman, L.I., Ghia, K.N. and Hermann, W.G. 1967. "Research on Mixing of Coaxial Streams", Aerospace Research Laboratories Report ARL 67-0058, Wright-Patterson Air Force Base, Ohio.

Frankel, R. J. and Cumming, J. D. 1965. "Turbulent Mixing Phenomena of Ocean Outfalls", Proc. ASCE, Journal of the Sanitary Engineering Division, Vol. 91, No. SA 2, pp. 33-59.

Goldstern, P. P. 1963. "The Entrainment of Flow through Ports in a Conduit Wall", M.S. Thesis, Univ. of Washington, Seattle, Wash. (unpublished).

Gordier, R. L. 1959. "Studies on Fluid Jets Discharging Normally into Moving Liquid", Technical Paper, No. 28, Series B, St. Anthony Falls Hydr. Lab., Minneapolis, Minn.

Hill, P. G., 1965. "Turbulent Jets in Ducted Streams", Journal of Fluid Mechanics, Vol. 22, 1, pp. 161-186.

McNown, J. S. 1954. "Mechanics of Manifold Flow", Transactions ASCE, Vol. 119, pp. 1103-1143.

Mueller, N. H. G. 1964. "Water Jet Pump", Proc. ASCE, Journal of the Hydraulics Division, Vol. 90, No. HY3, pp. 83-113.

Nece, R. E., Goldstern, P. P. and Black, J. L. 1966. "Single-Port Suction Manifolds", Proc. ASCE, Journal of the Hydraulics Division, Vol. 92, No. HY1, pp. 43-64.

Pearson, E. A. 1956. "An Investigation of the Efficacy of Submarine Disposal of Sewage and Sludge", Publication No. 14, State Water Pollution Control Board, Sacramento, Calif.

Rawn, A. M., Bowerman, F. R. and Brooks, N.H. 1961. "The Diffusion of Sewage in Sea Water", Trans. ASCE, Vol. 126, Part III, pp. 344-388.

Rouse, H. 1946. "Elementary Mechanics of Fluids", John Wiley and Sons, Inc., New York, N.Y.

Schraub, F. A., Kline, S. J., Henry, J., Runstatdler, P. W. and Littell, A. 1964. Report MD-10, Thermosciences Div., Dept. of Mechanical Engineering, Stanford Univ., Stanford, Calif.

Silvester, R. 1967. "Jet Mixers in Sewage Outfalls", Journal of the Institution of Engineers, Australia, Vol. 39, No. 3, pp. 33-37.

Silvester, R. and Mueller, N. H. G. 1968. "Design Data for the Liquid-Liquid Jet Pump", Journal of Hydraulic Research, Vol. 6, No. 2, pp. 129-162.